NANYANG TECHNOLOGICAL UNIVERSITY

INDUCED TRANSPARENCY IN RING RESONATOR DEVICES

YANBING ZHANG

School of Electrical & Electronic Engineering

2012

INDUCED TRANSPARENCY IN RING RESONATOR DEVICES

YANBING ZHANG

School of Electrical & Electronic Engineering

A thesis submitted to the Nanyang Technological University
in partial fulfillment of the requirement for the degree of
Master of Engineering

2012

ACKNOWLEDGEMENT

First I would like to express my sincere and utmost gratitude to my supervisor Prof. Mei Ting for his kind encouragement, support and advice through the past two years. My heartfelt appreciations go to my co-supervisor, Prof. Zhang Daohua, for his generous guidance, trust and support in Nanophotonics Lab during my research. My gratitude also extends to Nanyang Technological University that provided me the research scholarship for pursuing my Master of Engineering Degree in the University.

My appreciation goes to Dr. Stevanus Darmawan and Dr. Landobasa Yosef Mario for their guidance in the research. The collaboration and discussion with them benefits my growth in academic research. In addition, I am truly grateful for Dr. Tran Quynh for his help in FDTD programming and encouragement for my research. Our brief conversations relax the stress from study and life. I would also thanks to my senior graduates, Lee Shun Ying, Li Yicen, Zhao Qiuji, Feng Chengang, and Li Dongdong, among many others in Nanophotonics Lab.

Lastly but most important, my special appreciations and gratitude to my girlfriend Zou Qiong as well as my and her families, whose constant understanding and moral support are the greatest encouragement in our study and life.

TABLE OF CONTENTS

ABSTRACT

A microring resonator consists of a ring side-coupled to a bus waveguide, where the light exchange is achieved by means of evanescent coupling mechanism. It is a strong candidate for integrated optics due to its advantage of compact size, cascadable input/output ports, and the compatibility of CMOS fabrication. The microring resonator can be used to create many interesting phenomena that are difficult to obtain in other classical configurations.

This thesis focuses on the theoretical analysis and experimental realization of induced transparency in optical devices derived from ring resonators. In this thesis, I propose a ring-bus-ring Mach-Zehnder interferometer (RBRMZI) system based on a 3×3 coupler, and show that such a system can generate an electromagnetically induced transparency (EIT)-like spectrum via phase engineering facilitated by inter-pathways interference between RBR and MZI, instead of separate light interaction in two resonators alone. Both the transfer matrix formalism and the temporal coupled mode theory are investigated to model this induced transparency. The relationship between the two theories is obtained via the energy-conservation and *Q*-factors.

In addition, the EIT-like spectrum in the RBRMZI is experimentally realized using silicon-on-insulator technology. The best RBRMZI device has a transparency with a bandwidth of 0.25nm, a free spectral range of 12nm and a *Q*-factor of ~6300. With further measurements of the devices having strong ring-bus coupling, we obtain a *Q*~18000 when the circumference of one ring is 43.4μm and the circumference of the other ring is slightly detuned by ~0.035%. Moreover, we achieve a roundtrip loss as small as ~0.5% of the input energy. The measurement results agree well with theoretical prediction and 2D-FDTD numerical calculations.

LIST OF ABBREVIATIONS

IC – Integrated Circuit
CMOS – Complementary Metal Oxide Semiconductor
MOMS – Micro-Opto-Mechanical System
MZI – Mach-Zehnder Interferometer
SCISSOR – Side-Coupled Integrated Spaced Sequence of Resonators
CROW – Coupled Resonator Optical Waveguide
BDP – Bandwidth Delay Product
CIPS – Coupling-Induced Phase Shift
MRDC – Micro-Ring-assisted Directional Coupler
WDM – Wavelength-Division Multiplexing
REMZI/DRMZI– Ring-Enhanced/Dual-Resonator Mach-Zehnder Interferometer
EIT – Electromagnetically Induced Transparency
SOI – Silicon-On-Insulator
CRIT – Coupled Resonator Induced Transparency
PhC – Photonic Crystal
RBR – Ring-Bus-Ring
RBRMZI – Ring-Bus-Ring Mach-Zehnder Interferometer
TMF – Transfer Matrix Formalism
TCMT – Temporal Coupled Mode Theory
BPM – Beam Propagation Method
EIM – Effective Index Method
TE – Transverse Electric field
TM – Transverse Magnetic field
FDTD – Finite-Difference Time-Domain
FP – Fabry-Pérot
FSR – Free Spectral Range
FWHM – Full-Width at Half-Maximum
ER – Extinction Ratio
MMI – Multi-Mode Interferometer
DUT – Device Under Test

Chapter 1 Overview: Background, Objectives and Major Contributions

1.1 Motivation

The semiconductor industries have experienced tremendous technology development over the last half century. Until now, it is still possible to follow Moore's law as scaling down the device dimension based on existing planar platform of integrated circuits (IC). This is possible due to the technological advancement paved in lithography systems leading to nanometer-scale dimensions using complementary metal-oxide-semiconductor (CMOS) technology. Nevertheless, further miniaturization or downscaling becomes increasingly challenging due to several intrinsic technical and commercial difficulties. For instance, although the continuous dimensional scaling may improve the transistor performance in terms of the gate switching delay, the global interconnect resistance delay has become the major bottleneck which inhibits the main circuit performance. Moreover, as the area of a chip becomes larger for facilitating ever more complex functionality, which in turn leads to huge increase in the total interconnect length, the severe power dissipation problem will deteriorate the IC performance. In a nutshell, further functionality growth and speed demand within conventional planar ICs would not be possible without compromise on performance, process complexity and cost.

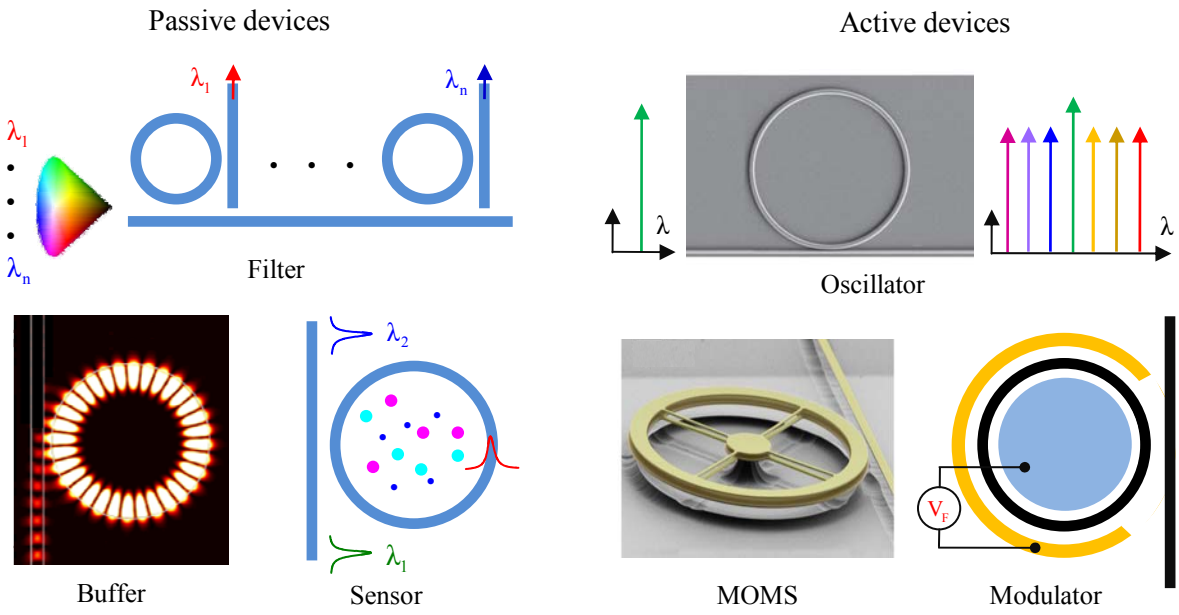

Fig. 1.1. Examples of optical devices based on microring resonators, including filters [1], buffers [2, 3], sensors [4], oscillators [5], micro-opto-mechanical systems (MOMS) [6] and modulators [7-8].

The optical complementary approach in information processing, especially in the aspect of intra-chip and inter-chip data communications, has been explored in recent years. Optical devices can be realized in a small building block with high integration density and high operation performance. Optics has presented advantages over electronics in communications, such as high speed and large capacity, as one

transmission line can carry many signal channels at different wavelengths without disturbing each other, and optical signal does not suffer from time delay due to electronic parasitic effects.

The realization of all-optical processing calls for both active and passive devices. Microring resonators are an essential optical device candidate for photonic integrated circuit that has been extensively exploited for a variety of devices [1-8], as shown in Fig. 1.1. The microring resonator is a form of Fabry-Pérot (FP) analog in optics where the resonant mode is excited by the evanescent coupling from the coupled waveguide [3]. However, compared to the normal FP etalon, the feedback mechanism of microring resonator is simply induced by a loop waveguide, without requiring of any Bragg grating, mirror or distributed feedback structures that are more difficult to fabricate. Thus, it has the advantage of being completely planar devices with input and output ports lying in the same plane and thus allowing easy cascading of many different devices on a wafer [2]. Besides the optical devices based on standalone microring resonators, many modified structures have been investigated using coupled resonators [9-17]. In particular, the synergistic integration of ring resonators with the Mach-Zehnder interferometer (MZI) has yielded interesting applications [18-26]. This highlights the flexibility and the versatility of microring resonator-based MZI devices in realizing various optical functionalities.

1.2 Literature review

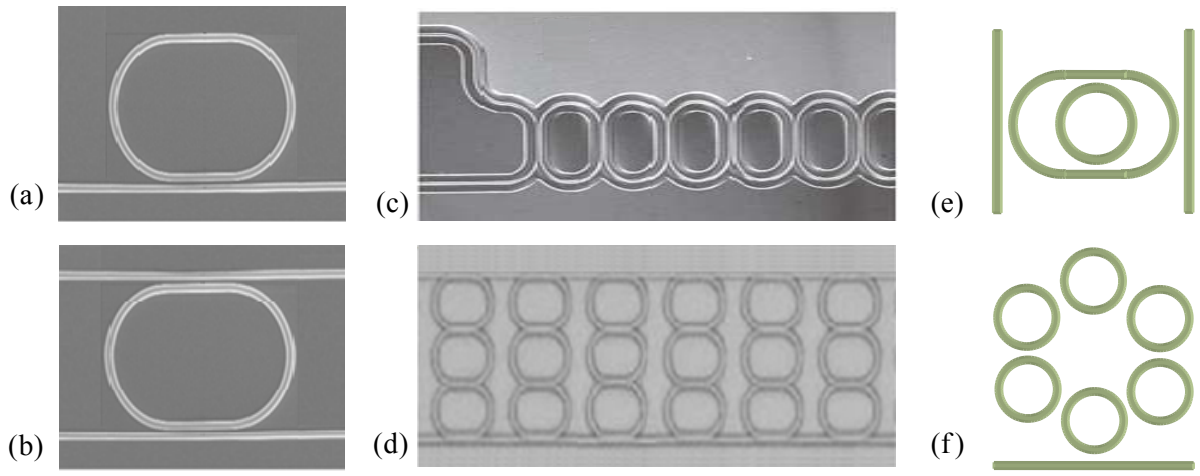

Fig. 1.2. Examples of various microring resonator configurations. SEM images of (a) a 1R1B, (b) a 1R2B, (c) a CROW [14], and (d) 2D array coupled ring resonators [15]. (e) Proposed embedded ring resonators [16], and (f) circular array of serially coupled resonators [17].

The simplest ring resonator is a bus waveguide shaped into one ring structure (1R1B) [see Fig. 1.2(a)]. When the round-trip optical path length in the ring is equal to an integral multiple of input wavelength, light couples into the ring and builds up inside, which is named on-resonance. The 1R1B becomes an add-drop resonator (1R2B) if a second waveguide is situated in close proximity to the ring structure [see Fig. 1.2(b)]. Besides the basic single-ring configurations, many progresses have been made in designing and fabricating more sophisticated devices through employing double/multiple rings, like the two-ring-two-bus (2R2B) [9], the two-ring-one-bus (2R1B) [10], and the side-coupled double-ring resonator [11].

Furthermore, various kinds of ring resonators cascaded in parallel or serial have been investigated, e.g., zigzag resonator chains [12], side-coupled integrated spaced sequence of resonators (SCISSOR) [13], coupled resonator optical waveguides (CROW) [see Fig. 1.2(c)] [14], as well as two-dimensional coupled ring resonator arrays [see Fig. 1.2(d)] [15]. It is worth noting that the cascaded ring resonator presents the box-like transmission, which is a promising candidate for digital signal processing due to its flat-top transmission response. This structure resembles a hybrid combination of distributed Bragg reflectors and ring resonators, with each ring serving as a frequency-dependent reflector [15]. In addition, certain novel configurations have been proposed recently, such as embedded ring resonators [16] and circular array of serially coupled resonators [17], as depicted in Fig. 1.2(e) and Fig. 1.2(f), respectively.

One of the attractive topics on ring resonators is the optical buffer for storing/slowing light. It has been theoretically and experimentally reported that either the single resonator or the periodic coupled resonator arrays can reduce the group velocity of light [14, 17, 28-31]. The polymer CROW with 12 resonators was experimentally demonstrated to have a flat delay of ~140ps over a 17GHz bandwidth [28]. Similarly, by applying 100 cascaded rings in the CROW structure, the on-chip group delay exceeding 500 ps was obtained within a footprint below 0.09 mm^2 [14]. Much improvement has been done in the circular array of ring resonators [17], where a large flat delay enhancement can be dynamically obtained by simply varying the loop coupling strengths. This structure creates a bandwidth delay product (BDP) of $2N\pi$ due to the enhanced finesse in the circular loop, which is twice of that in the CROW and the SCISSOR with the number of N identical rings. However, even though the delay can be extendable with large number of resonators, the intrinsic limits BDP caused by the higher-order dispersion and rippling transmission spectrum in multiple rings inhibits the ring resonator as an optical buffer, e.g. the experiment result shows the CROW with 100 rings is only able to buffer one-bit data without distortion [14].

The microring resonator devices have been fabricated on many material platforms, such as silicon-on-insulator (SOI) [1, 4, 32, 33], polymer [24, 28] and III-V alloys (InP [2, 22] and GaAs/AlGaAs [3, 34]). Even though the structures have been theoretically predicted to exhibit the desired characteristics, the small size and stringent requirements for ring resonators impose severe challenges in practical fabrications. For example, in the cascaded ring resonators, any mismatch in the coupling region of ring-to-ring or ring-to-waveguide bus will degrade the filter characteristics [15]. The losses in ring resonator is another problem that needs to be considered. The sidewall scattering loss caused in etching process is the dominant source of loss in SOI high-index waveguides. This problem could be solved by a novel etchless process without exposing the silicon surface to any plasma etching throughout the fabrication process [33]. The interest of this etchless process is to obtain the configuration of the microring resonator and the upper grown oxide cladding using selective thermal oxidation of silicon core [see Fig. 1.3(a)]. However, since the mode confinement is rather weak in the lateral edges, the fabricated ring has a relatively large radius of 50μm and a high propagation loss of 0.8dB/cm. Furthermore, the coupling-induced phase shift (CIPS) is an important fundamental source of resonance frequency mismatch in mutually coupled resonators [35]. Hence, the spectral response degradation in ring resonators caused by CIPS must be compensated in

designing and fabrication. Several approaches have been developed to offset the CIPS effect [35-37]. For instance, reference [37] provides a simple method to quantitatively analyze the CIPS for 2×2 directional couplers by incorporation of the second-order coupling effect in coupled-mode theory. It has also been experimentally demonstrated on SOI technology that the shifting phase in the high-order filters can be cancelled-out by using different gaps at the mutual coupling regions [37] [see Fig. 1.3(b)].

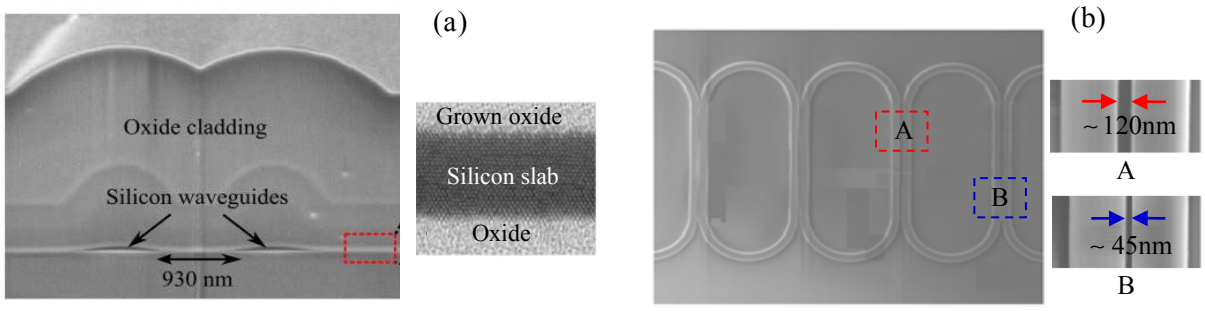

Fig. 1.3. (a) Cross-sectional image of the coupling region in the etchless SOI ring resonator [33]. (b) A 3rd-order filter made of three racetrack coupling resonators [37].

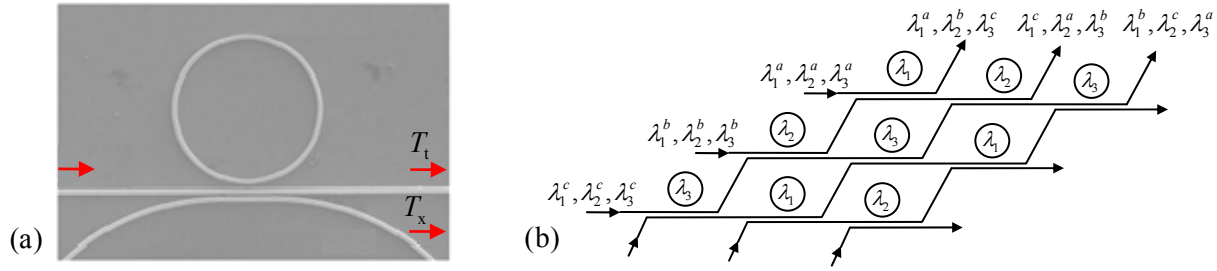

Fig. 1.4. (a) A MRDC device on SOI material [38]. (b) Schematic of a 3×3 WDM cross-connect grid using MRDC structures. The resonant wavelengths are indicated inside each ring.

So far, all the microring resonator configurations discussed above are based on 2×2 couplers. In 2009, A. M. Prabhu firstly demonstrated a new resonator system using a 3×3 coupler for signal processing, which is named as a microring-assisted directional coupler (MRDC) [38], as shown in Fig. 1.4(a). The interesting feature of this system lies in the fact that the power coupling between the two side-coupled waveguides can be mediated by the ring resonance [39], giving different transmission responses at the two output ports. The resonant light couples into the through port (T_t) and induces associated dips in the cross-port spectrum (T_x). This feature suggests that this device allows novel cascaded microring architecture to be constructed for wavelength-division multiplexing (WDM), as shown in Fig. 1.4(b). Unlike the cross-connect grids using conventional single add-drop rings, the MRDC does not require direct waveguide crossings and thus avoids the problem of cross talks due to waveguide junction scattering.

Next, we are going to review the microring resonator-based MZI devices. The MZI is a common element in integrated optical systems that has been extensively applied as sensors, switches and modulators. The root of the extreme applications of MZI devices owing to its two complementary outputs

and thus it is flexible to introduce different transmissions through changing the phase difference between two MZI arms. In order to enhance the phase difference and realize novel applications, one promising approach is to combine the ring resonator and the MZI together named as ring-enhanced MZI (REMZI), as depicted in Fig. 1.5(a) for the simplest schematic [18]. The phase response of the ring resonator can be detuned flexibly and it effectively enhances the interference between the upper arm and the lower arm in the MZI. The REMZI has exhibited many interesting properties, e.g., the sharp asymmetric Fano resonance profile [19]. The steep slope of the Fano resonance can be introduced to improve the performance of devices, like reducing the threshold power of a modulator/switch and increasing sensitivity of a sensor. It has been theoretically reported that the maximum sensitivity of an optimized REMZI sensor is increased by 30% while the operating power is reduced by 25% compared to that of a standalone 1R1B resonator sensor with an identical ring perimeter and loss [20]. Meanwhile, such a low operating power is very useful for the suppression of undesirable nonlinear effects. Much more research is dedicated to apply the nonlinear ring resonator to boost the accumulated nonlinear phase shift. It has been reported that the switching threshold can be reduced by four or more orders of magnitude to the level of milliwatts [21]. Some modified conventional REMZI with a feedback path between one MZI output and the input has been demonstrated as a thermo-optical tunable switching in InGaAsP-InP material [22] [see Fig 1.5(b)]. Because the feedback mechanism possesses a large transmission change with a small phase imbalance between two MZI arms, this unique design enables a substantial reduction of the switching power. The reduced power for complete switching is 26mW in comparison with 40mW of a conventional MZI switch. Similarly, using the feedback mechanism, the nest ring MZI (NRMZI) is proposed through connecting two ends of 1R2B device with a feedback loop in one MZI arm. The NRMZI is able to exhibit the box-like transmission spectrum with sharp transition edges, which is highly desirable for the digital switching and filtering [23].

Many configurations with multiple rings as the variations of basic one-ring MZI are also investigated, including integrated MZI based on two-ring resonators [9, 10], SCISSORs [24], as well as CROWs and two-dimensional resonators [25]. The amplitude and phase characteristics of various ring array configurations and how they can be used to physically engineer the MZI transmission behavior have been systematically studied in reference [25]. It is interesting to find that the two-ring MZI shown in Fig. 1.5(c) can effectively enhance the finesse and thus introduce a very sharp resonance, when the resonant light is strongly localized in the larger ring while the smaller ring is anti-resonant [10]. Through slightly detuning the two rings, the MZI can produce a very sharp narrow Fano resonance, which realizes the switching of high extinction ratio (>10dB) and large modulation depth (~1) with low switching power ($n_2 I_{IN} \sim 10^{-5}$) at the point of the small ring is off resonant [9]. Besides the MZI configurations modified by cavity in one arm, reference [26] proposes a new dual-ring MZI with both arms integrated with resonators [see Fig. 1.5(d)]. In this structure, one resonator is side coupled to one arm and the other ring is inserted into the second arm similar to a 1R2B. This device can create a narrow transparent peak between two resonant frequencies in the transmission spectrum (this induced transparency will be discussed in next paragraph).

Moreover, some new structures resembling to conventional MZI have been analyzed for switching, where a 100% switching can be produced with a small index perturbation of ~2×10^{-3} [27].

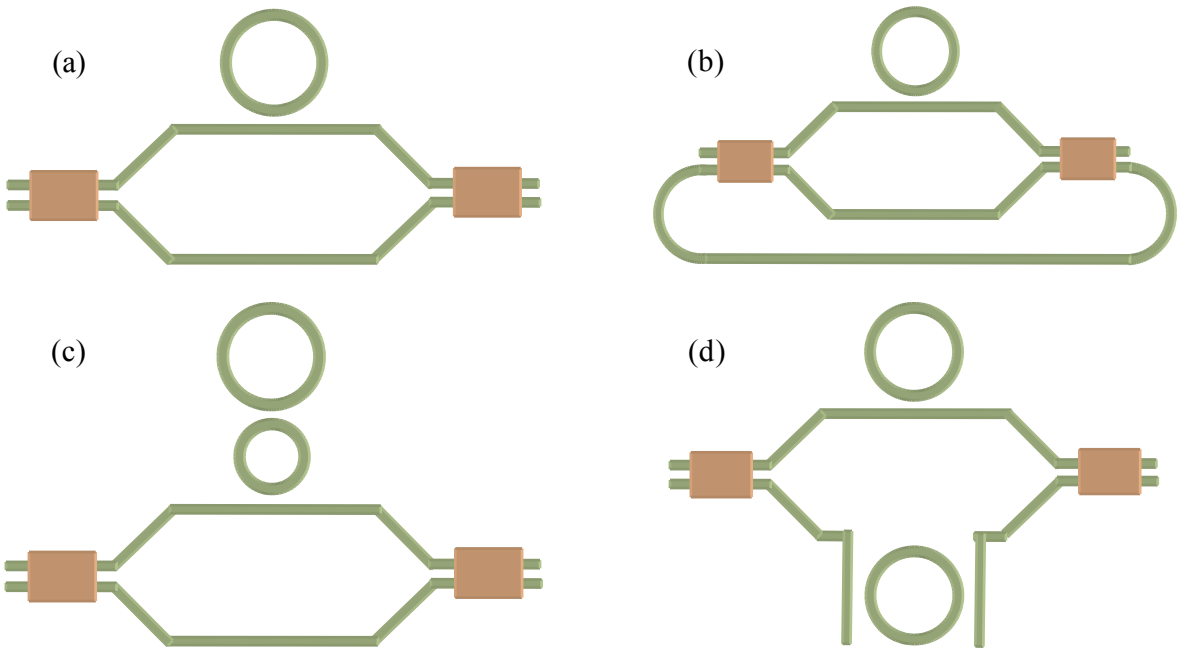

Fig. 1.5. Schematics of various REMZI configurations. (a) One ring coupled REMZI [17]. (b) Feedback REMZI [22]. (c) Two-ring finesse enhanced REMZI [10]. (d) Dual-ring coupled MZI with each ring shaped into one arm [26].

In addition, microring resonators can generate many unusual effects that are difficult to achieve in conventional systems. For example, recent theoretical analyses have revealed that the phenomenon analogous to electromagnetically induced transparency (EIT) in atomic systems can also be remarkably observed in optical resonant cavities, which is well-known as coupled resonator-induced transparency (CRIT) [40-42, 43-46]. In order to elucidate the analogy between atomic EIT and photonic CRIT, let us first review EIT in an atomic three-level scheme as illustrated in Fig. 1.6(a). The quantum EIT involves the destructive interference between two excitation pathways, including $|1\rangle-|3\rangle$ and $|2\rangle-|3\rangle$, to a common upper level $|3\rangle$ [43]. The atomic transition of $|1\rangle-|3\rangle$ and $|2\rangle-|3\rangle$ define the absorption of the probe laser field with frequency ω_p and the control (pump) laser field with frequency ω_c, respectively [46]. When a strong control field is resonantly applied to $|2\rangle-|3\rangle$ transition, the excited state $|3\rangle$ splits into two dressed states as $|\pm\rangle=\left(|3\rangle\pm|2\rangle\right)/\sqrt{2}$, separated by the Rabi frequency of the control field ω_c. The absorption of a weak probe beam, resonant with the $|1\rangle-|3\rangle$ transition, vanishes due to the fact that a Fano-type interference occurs between the two indistinguishable quantum mechanical paths [40]. This interference is destructive owing to a π phase difference between the two contributions to the atomic response at the probe frequency. Therefore, the destructive interference between the two absorption amplitudes, containing excitation pathways from $|1\rangle-|3\rangle-|2\rangle-|3\rangle$ indirectly and from $|1\rangle-|3\rangle$ directly, leads to no

absorption of the applied fields between two separated dressed states, which is represented by an extreme narrow transparent window in the center of a broad transmission dip, as shown in Fig. 1.6(b).

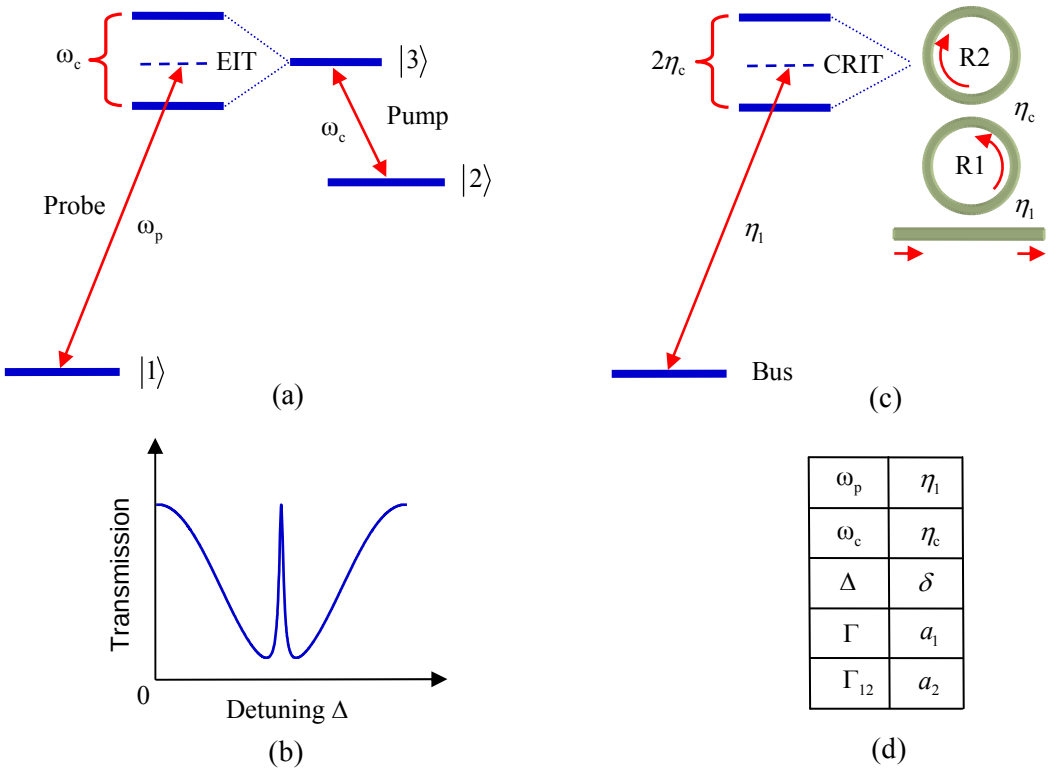

Fig. 1.6. (a) Three-level energy atomic system of EIT. (b) Signature of EIT, where Δ is the angular frequency detuning of the probe field. (c) CRIT occurs in two mutually coupled rings. (d) Analogies of parameters between EIT and CRIT. η_1 and η_c is the cross-coupling coefficient between R1 and bus, as well as R1 and R2, respectively. δ is the detuning and $a_{1,2}$ are the intrinsic losses of R1,2 [40].

In the atomic systems, the EIT occurs due to quantum destructive interference between two atomic transitions to a common energy level induced by coherently deriving the atom with an external laser, leading to a sharp reduction of absorption and resulting in a transparent window between two dressed states [43]. In a similar fashion, the CRIT occurs by virtue of the coherent interference between two resonant optical pathways instead enforced by the geometry of a system, which introduces a transparent region between the two resonance wavelengths. There are several approaches for combining EIT and ring resonators to obtain transparent spectrum in photonic systems [44-46]. Fig. 1.6(c) shows the optical CRIT analog to EIT in a mutually coupled two-ring system. Here, the mutual coupling of the two rings (η_c) works as the control laser field and the ring-bus coupling (η_1) works as the probe field in the atomic system. When the circumferences of the two rings are identical, the resonance frequency (ω_0) of a standalone ring splits to two separate resonances $\omega_0 \pm \eta_c$ due to a destructive interference between the two resonant fields from two rings, resembling the two dressed states caused by two atomic transitions. This inherent destructive interference is attributed to the fact that the resonant light must traverse a coupler twice, acquiring a net π phase shift before interfering with light in the initial ring. Fig. 1.6(d) shows the analogies of parameters between EIT in atomic systems and CRIT in ring resonators. The intrinsic losses

and coupling strengths in the two-ring resonator are analogous to the two different decay rates (Γ and Γ_{12}) and transitions (ω_p and ω_c) in an atomic system, respectively, where $\Gamma=\Gamma_{31}+\Gamma_{32}$ is the decay rate from level $|3\rangle$ to levels $|1\rangle$ and $|2\rangle$, as well as Γ_{12} is the decay rate from level $|1\rangle$ to level $|2\rangle$. Thus, this analogy tells us that the CRIT only happens when the two resonators have different intrinsic losses and coupling strengths. In other words, the induced transparency requires that R1 is quite lossy, R2 is nearly lossless ($a_2>a_1$, $a_2\sim1$), and the cross-coupling coefficient between R2 and the bus waveguide is much larger than that of the rather weak mutual coupling between R1 and R2 ($\eta_1>\eta_c$, $\eta_c\sim0$).

The first experimental realization of EIT-like spectrum in optical resonators is achieved using a pair of SOI microrings coupled to double waveguides structure, as shown in Fig. 1.7(a) [45]. Cascading the two rings together allows a resonance to form via multiple, constructively interfering "reflections" ($T_{reflected}$) between the two rings, which will introduce EIT-like transparent region in-between two resonance frequencies in the through transmission (T_{out}) spectrum. Here, the two resonances with frequencies of ω_1 and ω_2 are analogue to the two separated dressed states in the atomic EIT system. Unlike the two-ring resonator in Fig. 1.6(c), since the field interaction between the two individual rings is facilitated by a double parallel waveguides, there is no direct mutual coupling between the two rings and thus no intrinsic resonance splitting. Here, the control field is determined by the frequency difference ($|\omega_2-\omega_1|$) and the probe field is determined by the two coupled bus waveguides. Therefore, the bandwidth and the amplitude of such a transparency can be detuned by adjusting the ring-to-ring distance between the two resonators [45]. However, in practice, a slight derivation of the ring-to-ring separation can seriously degrade the expected transparent peak due to the Vernier effect of the two ring resonances. Similarly applying the Vernier effect from cascaded cavities, the EIT-like profile has also been observed in the multiple photonic crystal (PhC) cavities system shown in Fig. 1.7(b) [46]. In comparison to the structure in Fig. 1.7(a), for the PhC resonator, only one bus waveguide is enough to assist the field interaction between the two cavities due to the bi-directional standing modes in PhC cavities.

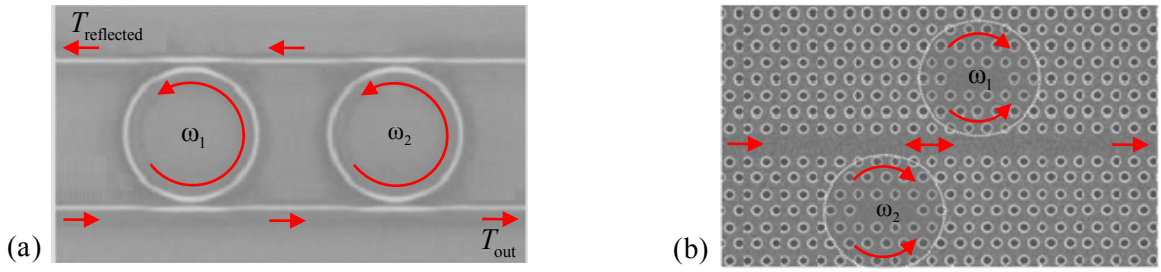

Fig. 1.7. The EIT-like spectrum realized by (a) the cascaded two 1R2B resonators configuration [45] and (b) multiple cavities in PhC structure [46]. The arrows indicate the light propagation direction.

The characteristics of EIT-like (or CRIT) normally consist of a linear phase response followed by a narrow transparency in the transmission, which means that a large sensitivity (or responsivity) can be realized without dispersion. These characteristics conform to the requirement of optical filters, delay lines (or optical buffers), optical switching and bio-chemical sensing, where the extinction ratio and phase

linearity are certainly desired. Moreover, since the CRIT resonance is a result of an internal coupling between individual oscillators without requirements of extra pump laser and low temperature, CRIT is more flexible than EIT in optical applications. For example, the steep linear dispersion characteristic of the narrow transparent resonance can be used to reduce the velocity of light [47-51]. It has been experimentally reported that the light can be stored on-chip using the structure in Fig. 1.7(a), with longer times than the bandwidth-determined photon lifetime of the static device using ultrafast tuning of ring resonators [49]. Further advances also demonstrate that the transparency can reduce the propagating pulse with a positive delay of 8.5ns with low pulse deformation [50], and 25ps delay using thermo-optic detuning [51]. In addition, since the CRIT resonance is much narrower compared to that of individual resonator, the capability for controlling the linewidth of such resonance is important for low-power switching and tunable bandwidth filter. Through tuning the rings, it would enable applications for all-optical interconnects and signal processing, where nonlinear component can be achieved using micron-sized integrated silicon devices [45].

1.3 Objectives

Based on the backgrounds introduced above, the thesis will focus on the theoretical investigation and experimental realization of the CRIT in ring resonator integrated MZI devices. The objectives of this thesis are summarized as follows:

(1) To develop the transfer matrix formalism (TMF) and temporal coupled-mode theory (TCMT) for 3×3 coupler (tri-coupler)-based devices.

(2) To theoretically investigate the physics of ring-bus-ring (RBR) and ring-bus-ring Mach-Zehnder interferometer (RBRMZI) systems, as well as their potential applications.

(3) To experimentally demonstrate and characterize the RBR and the CRIT in RBRMZI.

1.4 Major contributions

The major contributions are the theoretical analysis of RBR and RBRMZI using TMF and TCMT, as well as the experimental demonstration of the RBR and CRIT in RBRMZI. The original contributions are summarized as follows:

(1) A new type of device - the RBR configuration was proposed and a general 3×3 coupling matrix for modeling the symmetric/asymmetric RBR configurations was developed. The RBR behaves like 1R1B with two identical rings but has two separated resonances with two size-detuned rings. This uniqueness implies the RBR is applicable for channel-drop filter and 1×3 power splitter, which takes only half footprint of conventional devices.

(2) A RBRMZI system capable of generating CRIT resonance was proposed and analyzed. Theoretical analysis using TMF and TCMT was performed, showing a good agreement with 2D-FDTD simulation results. Different from other existing EIT-like schemes where the high resonators' finesses are required, the proposed CRIT spectrum in RBRMZI system is generated out of low-finesse resonators. The

transparency becomes sharper as the coupling strength between two resonators is increased, with the background spectrum significantly reduced as a result of additional phase shift from indirect coupling. For completeness, the RBRMZI with 3×3 multimode interferometer (MMI) coupler with high fabrication tolerance is also presented.

(3) The CRIT in RBRMZI was experimentally demonstrated using SOI technology. A fair agreement was obtained between the theoretical prediction and measurement results. The basic characteristics of the transparent resonance were extracted, showing the transparency can be created without the requirement of different losses in the two rings and a very small difference of ring circumferences. The best transparency has a bandwidth of 0.25nm, a free spectral rage of 12nm and a quality factor around 6300.

1.5 Thesis organization

This thesis is organized into six chapters. Chapter 1 is the thesis overview, containing the motivation for the thesis, the literature review that provides the current research in the field of induced transparency using ring resonators, the objective, the major contributions and organization of the thesis. Chapter 2 describes the optical mode theory of coupled waveguides and the basic theory of two simplest one-ring configurations (1R1B and 1R2B). Chapter 3 presents the detailed theoretical model of the RBR and the CRIT generated in RBRMZI using the TMF. Chapter 4 applies the mode analysis using TCMT to illustrate physics of a tri-coupler in RBR and the occurrence of CRIT in RBRMZI. Chapter 5 covers the experimental verification of the sharp transparent resonance in RBRMZI on SOI technique. Consequently, the thesis demonstrates the induced transparency in optical devices based on ring resonators. Chapter 6 concludes the thesis and gives the directions for future work. Finally, the author's publications, appendices and references are listed.

Chapter 2 Basic Theory

2.1 Introduction

The optical waveguide and directional coupler are the two basic components to form a ring resonator. Dielectric waveguides are an optical structure that guides light by confining it in a rectangular or square core of higher index surrounded by a cladding of lower index due to total internal reflection. A rigorous physical description for light propagation begins with Maxwell's equations in the core and the cladding, and reduces them to a single wave equation. However, there is no analytical solution for rectangular dielectric waveguides since the electromagnetic fields extend beyond the core into a region where the geometry cannot be defined independently along orthogonal directions [3]. Although there are several analytical approximations of varying degrees of accuracy, notably Marcatili's method, effective index method (EIM) and beam propagation method (BPM), the problem of rectangular waveguides is best addressed with numerical methods. In this chapter, we first briefly recall the mode theory in slab optical waveguides, and then introduce the EIM to analyze the propagation of light in three-dimensional (3D) waveguides, in order to save the calculation time. After that, the 2×2 coupling matrix which is adopted to analyze the power exchange in directional couplers is discussed. Based on the obtained matrix, we extend the analysis to two fundamental one-ring resonators and deduce the important figures of merit relevant to the two configurations. The theories in this chapter chiefly originate from several references [2, 3, 52].

2.2 Optical dielectric waveguides

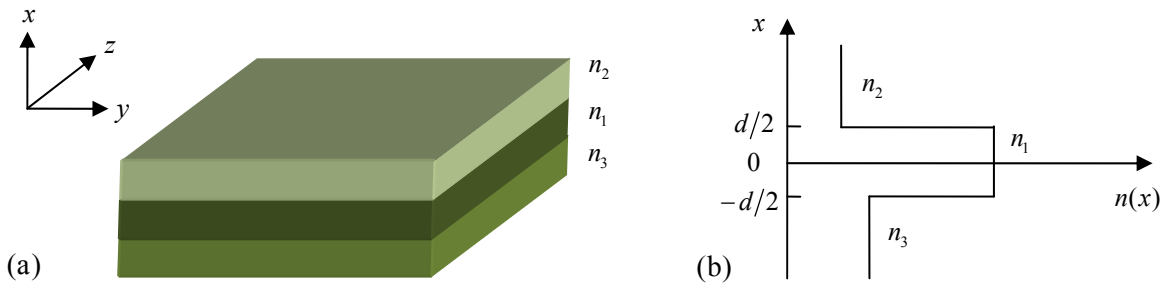

Fig. 2.1. (a) General schematic of a slab waveguide with asymmetric claddings. (b) Refractive-index profile of the slab waveguide in (a).

Fig. 2.1(a) presents a slab waveguide with asymmetric claddings, where the light propagates along the z-axis and confined only along the x-axis. Since the light is only invariant in the y-axis, the localized solutions require that the field decays to zero at $x\rightarrow\pm\infty$ [3]. We assume the guided wave has a time-dependency of $\exp[i(\omega t-\beta z)]$, where β is the propagation constant and ω is the angular frequency. The permittivity (ε) and permeability (μ) are set as $\varepsilon=\varepsilon_0 n_1^2$ and $\mu=\mu_1$ for the core layer in Maxwell's equations,

$$\begin{aligned}\nabla\times\mathbf{E}&=-i\omega\mu_1\mathbf{H}(x,y)\\ \nabla\times\mathbf{H}&=i\omega\varepsilon_0 n_1^2\mathbf{E}(x,y)\end{aligned} \tag{2.1}$$

where n_1 is the refractive index of the core area. We can reduce the Maxwell's vector curl equations from six to three equations involving E_y, H_x and H_z (H_y, E_x and E_z) for TE (TM) polarized modes, and combine them into a second-order wave equation for the transverse electric (magnetic) field components. Then, by taking into account the boundary conditions at the core-cladding interfaces $x=\pm d/2$ for the perpendicular and tangential electric and magnetic fields, we can solve the guidance condition for TE modes [52],

$$k_{1x}d = \tan^{-1}\left(\frac{\mu_1\alpha_2}{\mu_2 k_{1x}}\right) + \tan^{-1}\left(\frac{\mu_1\alpha_3}{\mu_3 k_{1x}}\right) + m\pi \qquad (m = 0,1,2,...) \tag{2.2}$$

and for TM modes,

$$k_{1x}d = \tan^{-1}\left(\frac{\varepsilon_1\alpha_2}{\varepsilon_2 k_{1x}}\right) + \tan^{-1}\left(\frac{\varepsilon_1\alpha_3}{\varepsilon_3 k_{1x}}\right) + m\pi \qquad (m = 0,1,2,...) \tag{2.3}$$

where k_{1x} are the wavenumbers in the core layer along the x-axis. α_2 and α_3 are the decay constants for the top and bottom cladding area, respectively.

Now, we are going to consider the rectangular waveguide with a width of w and a thickness of d, as shown in Fig. 2.2(a). The EIM mentioned earlier due to its simplicity is used to analyze the propagating light. The EIM starts by solving the center slab waveguide with refractive index inside the core and the cladding layers for each segmented slab waveguide. Here, we take the center segment with n_1, n_2 and n_3 for example. In Fig. 2.2(b), since E_y is parallel to the boundaries, the eigenequation for the E_y component should be that of TE modes of a slab waveguide. From the solution of the slab waveguide discussed in Eq. (2.2), we get the propagation constant and thus the effective index distribution $n_{\text{eff},1}$. Similar equations hold for the other two slab sections of $y<0$ and $y>w$, when $n_7>n_8$, n_9, and $n_4>n_5$, n_6 [52].

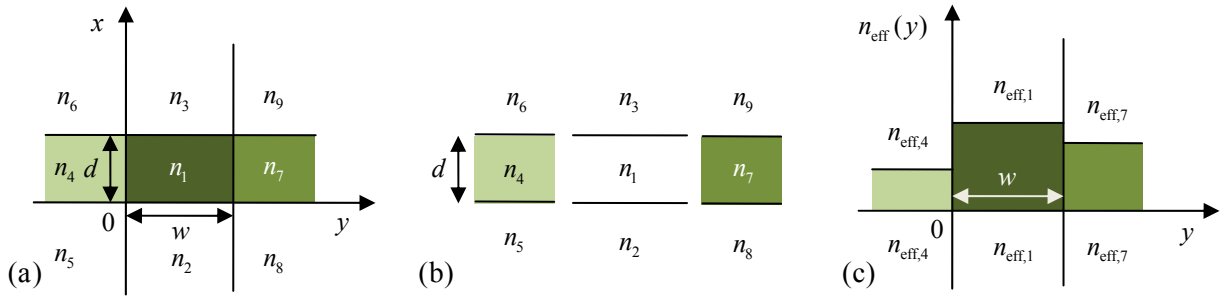

Fig. 2.2. Effective index approximation for a rectangular waveguide. (a) A rectangle waveguide to be investigated using EIM. (b) Obtain the effective index profile $n_{\text{eff}}(y)$ at three different dielectric regions. (c) Solve the slab waveguide problem with the obtained $n_{\text{eff}}(y)$.

Next, we solve the slab waveguide problem using the effective indices $n_{\text{eff}}(y)$ in each slab segment, as presented in Fig. 2.2(c). At this moment, since the component E_y becomes to be perpendicular to the slab boundaries, the guidance condition for TM modes in Eq. (2.3) is applied to solve the problem,

$$k_{1y}w = \tan^{-1}\left(\frac{n_{\text{eff},1}^2\alpha_2}{n_{\text{eff},7}^2 k_{1y}}\right) + \tan^{-1}\left(\frac{n_{\text{eff},1}^2\alpha_4}{n_{\text{eff},7}^2 k_{1y}}\right) + m\pi \qquad (m = 0,1,2,...) \tag{2.4}$$

Recall Eq. (2.2), we can see that a modal distribution is found as a function of x for each y position. This field distribution is called $F(x, y)$ since it also changes with the variation of y. While the solution for the modal distribution in Eq. (2.4) is a function of only y, which is called $G(y)$. Therefore, the total electric field E_y can be expressed with the separation of variables, which is the basic idea of the EIM,

$$E_y(x,y) \simeq F(x,y)G(y) \tag{2.5}$$

However, in practice, the best way to solve the problem of modal distribution is numerical calculation for the waveguide with rectangular cross-section. Numerous commercial software packages are available for obtaining the mode profile and the effective index concurrently. The software considered for waveguide designs in this thesis is Opti-FDTD. The numerical calculation is based on the popular finite-difference time-domain (FDTD) algorithm with a second-order numerical accuracy and an advanced boundary condition, i.e., uniaxial perfectly matched layer [53]. The waveguide material used in this thesis is silicon-on-insulator (SOI). As presented in Fig. 2.3(a), the SOI has a buffer oxide of thickness of 2μm, where the silicon core is sandwiched between two SiO_2 layers. The rectangular waveguide with a width of w=450nm and a thickness of d=220nm supports only the fundamental TE-like polarization (electric field predominantly in the plane of the structure). Fig. 2.3(b) presents the contour plot of fundamental mode in the cross-section. The 3D-FDTD simulation result shows this waveguide has n_{eff}~2.35 at the wavelength of 1550nm, which is pretty consistent with that obtained from EIM, where n_{eff}~2.38.

Fig. 2.3. (a) Sketch of the SOI rectangular waveguide. (b) Contour plot of the fundamental TE-polarized mode in the cross-section with n_{eff}~2.35 obtained from 3D-FDTD modeling.

2.3 Coupled waveguides

The light interaction in the ring resonator happens at the directional coupler region, which is based on parallel-coupled optical waveguides. As shown in Fig. 2.4, when two waveguides (WG p and WG q) are placed very close to each other, the optical power can be exchanged between their supporting modes via the evanescent wave. If the light is initially launched in one waveguide, it is eventually transferred to the other waveguide over some distance (the "beat length" L_π labeled in Fig. 2.4), which couples it back into the first waveguide, and so forth. Usually, the beat length is dependent on the separation gap and the propagation constant of the two waveguides.

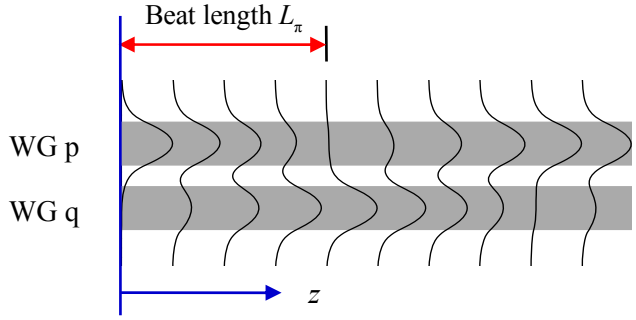

Fig. 2.4. Coupling of two parallel slab waveguides.

The coupling strength between the coupled waveguides is calculated by using the modes of individual waveguides and applying a perturbation-based approach from coupled-mode theory (CMT) [3]. Here, we follow closely the procedure in reference [52] to obtain the coupling matrix for two arbitrarily coupled waveguides. The coupled-mode equations in the vector form is given by $\partial s/\partial z = iMs$, where s is the eigenstate solution of coupled waveguides and M is a matrix consisting of propagation constant, coupling coefficient and overlap integrals. We consider the light propagating along the z-axis as depicted in Fig. 2.4. Applying the Maxwell's equations, the total field solutions can be written as linear combinations of individual waveguide modes,

$$\begin{aligned}\mathbf{E}(x,y,z) &= a_{\mathrm{p}}(z)\mathbf{E}_{\mathrm{p}}(x,y) + a_{\mathrm{q}}(z)\mathbf{E}_{\mathrm{q}}(x,y)\\ \mathbf{H}(x,y,z) &= a_{\mathrm{p}}(z)\mathbf{H}_{\mathrm{p}}(x,y) + a_{\mathrm{q}}(z)\mathbf{H}_{\mathrm{q}}(x,y)\end{aligned} \tag{2.6}$$

Note the time dependency $\exp[j(\omega t-\beta z)]$ in both electric and magnetic fields, then the field amplitudes a_{p} and a_{q} satisfy the following matrix,

$$\frac{d}{dz}\begin{bmatrix} a_{\mathrm{p}} \\ a_{\mathrm{q}} \end{bmatrix} = iM\begin{bmatrix} a_{\mathrm{p}} \\ a_{\mathrm{q}} \end{bmatrix} = i\left[\begin{bmatrix} \beta_{\mathrm{p}} & 0 \\ 0 & \beta_{\mathrm{q}} \end{bmatrix} + \begin{bmatrix} 1 & \hat{C} \\ \hat{C} & 1 \end{bmatrix}^{-1}\begin{bmatrix} \kappa_{\mathrm{pp}} & \kappa_{\mathrm{pq}} \\ \kappa_{\mathrm{qp}} & \kappa_{\mathrm{qq}} \end{bmatrix}\right]\begin{bmatrix} a_{\mathrm{p}} \\ a_{\mathrm{q}} \end{bmatrix} \tag{2.7}$$

where $\beta_{\mathrm{q,p}}$ is the propagation constant of a single waveguide without the presence of the other waveguide. $\hat{C}$ is the mean arithmetical value of two overlaps $\hat{C}=(C_{\mathrm{pq}}+C_{\mathrm{qp}})/2$, where $C_{\mathrm{pq,qp}}$ is the overlap integral between the two waveguides. $\kappa_{\mathrm{pq,qp}}$ and $\kappa_{\mathrm{pp,qq}}$ are the cross-coupling ($q\neq p$) and self-coupling ($q=p$) coefficients. The overlap integral, cross-coupling and self-coupling coefficients can be numerically calculated from the integral of the electromagnetic field between the two waveguides [52],

$$\begin{aligned} C_{\mathrm{pq}} &= \frac{1}{2}\int_{-\infty}^{\infty}\int_{-\infty}^{\infty}\mathbf{E}_{\mathrm{q}}(x,y)\times\mathbf{H}_{\mathrm{p}}^{*}(x,y)\bullet\hat{z}\,dxdy\\ \kappa_{\mathrm{pq}} &= \frac{\omega}{4}\int_{-\infty}^{\infty}\int_{-\infty}^{\infty}\left[\varepsilon(x,y)-\varepsilon_{\mathrm{q}}(x,y)\right]\left[E_{\mathrm{p}}^{*}(x,y)\bullet E_{\mathrm{q}}(x,y)-E_{\mathrm{p}}^{*}(z)\bullet E_{\mathrm{q}}(z)\right]dxdy\end{aligned} \tag{2.8}$$

where $\varepsilon(x,y)$ is the permittivity distribution for the two waveguides. $\varepsilon_{\mathrm{q}}(x,y)$ is the permittivity distribution when only the waveguide q exists. $E_{\mathrm{q,p}}(z)$ is the purely imaginary part of electric fields. We can see from the above equations that, compared to the self-coupling coefficient, the overlap integral is much smaller

that it can be neglected ($\hat{C}_{pq}$=0) due to the several order difference between the amplitudes of electric field and magnetic field. On the other hand, the total guided power in the two waveguides can be calculated by using the power conservation P=Re(**E**×**H***)/2=$|a_p|^2$+$|a_q|^2$+Re[$a_p a_q{}^* C_{pq}$+$a_q a_p{}^* C_{qp}$]. As all the transverse field components are real for a lossless system, we consider $\partial P/\partial z$=0 for arbitrarily amplitudes of $a_{p,q}$, and obtain κ_{pq}-κ_{pq}=(γ_p-γ_q)(C_{pq}+C_{qp})/2, where $\gamma_{p,q}$ is a complex propagation constant modified by the overlap intergals and self-coupling coefficients in Eq. (2.7). Applying $C_{pq,pq}$~0, we arrive at κ_{pq}=κ_{qp} for the set of co-directional coupled waveguides, and get a simplified *M* matrix as,

$$\frac{d}{dz}\begin{bmatrix} a_p \\ a_q \end{bmatrix} = i\begin{bmatrix} \beta_p + \kappa_{pp} & \kappa_{pq} \\ \kappa_{qp} & \beta_q + \kappa_{qq} \end{bmatrix}\begin{bmatrix} a_p \\ a_q \end{bmatrix} = iM\begin{bmatrix} a_p \\ a_q \end{bmatrix} \tag{2.9}$$

where β_m+κ_{mm} (m=p,q) is the normalized propagation constant of each waveguide due to the existence of self-coupling coefficient κ_{mm}. Through solving the eigenstate problem of matrix |M-$I\sigma$|=0, i.e., the two eigensolutions (σ_m) and associated eigenvalues (υ_m), we can express the output power with a matrix of s=Σ$c_m v_m$exp($i\sigma_m z$), where c_m is solved from the initial values of $a_{p,q}$ at z=0 ($a_{p0,q0}$). Finally, the coupling matrix to connect the input and output amplitudes is obtained by eliminating c_m in s,

$$\begin{bmatrix} s_p \\ s_q \end{bmatrix} = \exp(i\bar{\beta}z)\begin{bmatrix} \cos(\psi z) + i\frac{\Delta\beta}{\psi}\sin(\psi z) & i\frac{\kappa_{qp}}{\psi}\sin(\psi z) \\ i\frac{\kappa_{qp}}{\psi}\sin(\psi z) & \cos(\psi z) - i\frac{\Delta\beta}{\psi}\sin(\psi z) \end{bmatrix}\begin{bmatrix} a_{p0} \\ a_{q0} \end{bmatrix} \tag{2.10}$$

where $\bar{\beta}$ =(β_q+β_p+κ_{qq}+κ_{pp})/2, $\Delta\beta$=(β_q-β_p+κ_{qq}-κ_{pp})/2 and ψ=($\Delta\beta^2$+$\kappa_{pq}{}^2$)$^{1/2}$. In the ideal case, the self-coupling coefficients are negligible $\kappa_{pp,qq}$~0 and two waveguides have the same propagation constant β, i.e., $\bar{\beta} = \beta$, $\Delta\beta$=0 and ψ=κ_{qp}=κ, then Eq. (2.10) is simplified to a unitary matrix,

$$\begin{bmatrix} s_p \\ s_q \end{bmatrix} = \exp(i\beta z)\begin{bmatrix} \cos(\kappa z) & i\sin(\kappa z) \\ i\sin(\kappa z) & \cos(\kappa z) \end{bmatrix}\begin{bmatrix} a_{p0} \\ a_{q0} \end{bmatrix} \tag{2.11}$$

where the imaginary part i in the matrix suggests each cross-coupling will introduce a π/2 phase shift. Note that since the common phase term exp($i\beta$z) only shifts the entire resonance spectrum, it will be removed in the following analyses throughout this thesis.

However, in the more realistic situations, as shown in Fig. 2.5, either the racetrack coupling or the point coupling, there inevitably exist some non-idealities originated from three main sources. (1) We ignore the offset of the overlap integrals and the self-coupling coefficients in Eq. (2.11) by assuming an ideal case, i.e., a very weak coupling [e.g. cos(κz)>0.99]. When a strong coupling occurs, the overlap integrals and the self-coupling coefficients will introduce additional transmitted phase and result in coupling-induced phase shift (CIPS) [35]. (2) Due to the effects of the self-coupling coefficients and the overlaps, the propagation constants of the resonant mode and the guided mode are inherently phase-mismatched, which causes an asynchronous coupling and coupling loss at the directional couplers region.

(3) The coupling region is extended from the straight section to the curved section of the racetrack geometry. This extended coupling greatly increases the coupling strength, at a modest introduction of the junction loss and a reduction of the free spectral range, especially for a resonator with smaller ring radius. Extensive treatments of the optimized coupling of ring and waveguide can be found in reference [3].

Fig. 2.5. Ring resonators in racetrack coupling and point coupling conditions.

2.4 One-ring-one-bus

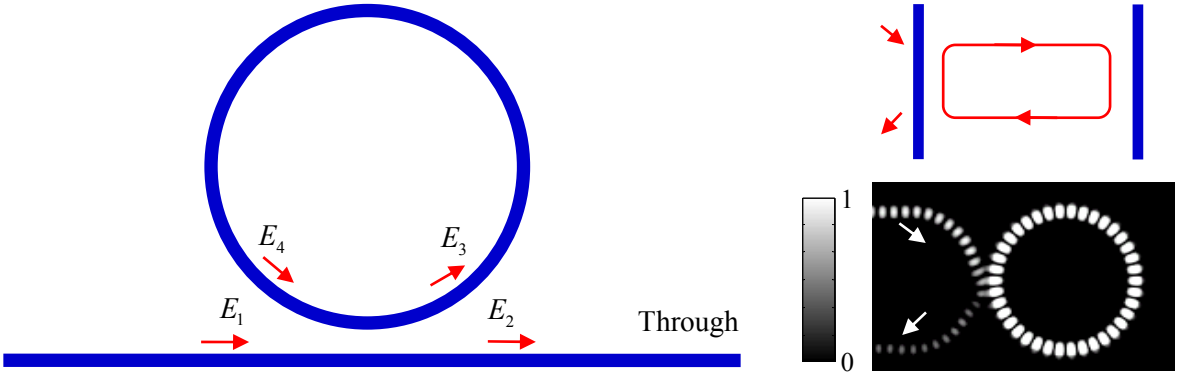

Fig. 2.6. Left: Schematic of the 1R1B configuration. Right: (upper) 1R1B is equivalent with FP etalon; (lower) Energy distribution of 1R1B device at resonance.

The configuration of one waveguide shaped into a ring (1R1B) is shown in the left of Fig. 2.6. The 1R1B structure is simply created by feeding one output of a directional coupler back into one input port. The functionality of such a device is analogous to a Fabry-Pérot (FP) etalon with a partial reflective and a full reflective mirror, and thus it exhibits a periodic cavity resonance when the round-trip phase is equal to an integral multiple of 2π radians. Here, instead of using an infinite sum derivations in FP etalon, the basic spectral properties are deduced by assuming the matching fields and steady-state operation [3].

It shows in Fig. 2.6 that the 1R1B resonator is mathematically formulated from two components: a coupling strength and a feedback path. The coupling strength involving the incident field E_1, transmitted field E_2 and circulating fields E_3 and E_4 are related via the matrix in Eq. (2.11),

$$\begin{bmatrix} E_2 \\ E_3 \end{bmatrix} = \begin{bmatrix} r & it \\ it & r \end{bmatrix} \begin{bmatrix} E_1 \\ E_4 \end{bmatrix} \tag{2.12}$$

where $r=\cos(\kappa z)$ and $t=\sin(\kappa z)$ are the reflection and cross-coupling coefficients that are analogous to the reflectivity r and transmittance t of partial reflective mirror in FP etalon, respectively. r and t satisfy the

relation of $r^2+t^2=1$ and are assumed to be independent of frequency. The feedback path connects the output from E_3 back into the input E_4 with $E_4=a\exp(i\delta)E_3$, where $a=\exp(-\alpha_{ring}L/2)$ is the round-trip amplitude transmission factor (or loss factor) and $a=1$ in a lossless case. L is the ring circumference and α_{ring} is the power loss in the ring per unit length. $\delta=k_0 n_{eff}L=t_R\omega$ is the round-trip phase response (or normalized detuning). t_R is the round-trip time and ω is the angular frequency. The ring is on resonance when δ is an even multiple of π, and it is on anti-resonance when δ is an odd multiple of π. Solving Eq. (2.12) with the feedback fields, the normalized transmission is obtained as,

$$T=\left|\frac{E_2}{E_1}\right|^2=\left|\frac{r-a\exp(i\delta)}{1-ar\exp(i\delta)}\right|^2=\frac{r^2+a^2-2ra\cos\delta}{1+r^2a^2-2ra\cos\delta} \tag{2.13}$$

Fig. 2.7 shows the general transmission calculated from Eq. (2.13) for 1R1B structure. When the incident light is on resonance in a lossless structure, i.e. $a=1$, the 1R1B predicts a unity intensity transmission for all values of normalized detuning δ and is termed an all-pass filter [3]. However, in practice, a strong confined light inside the ring can strengthen the effect of losses, such as the coupling loss and the scattering loss, which in turn induces periodical dips in the transmission spectrum. The 2π periodicity of resonant peaks is named as free spectral range (FSR).

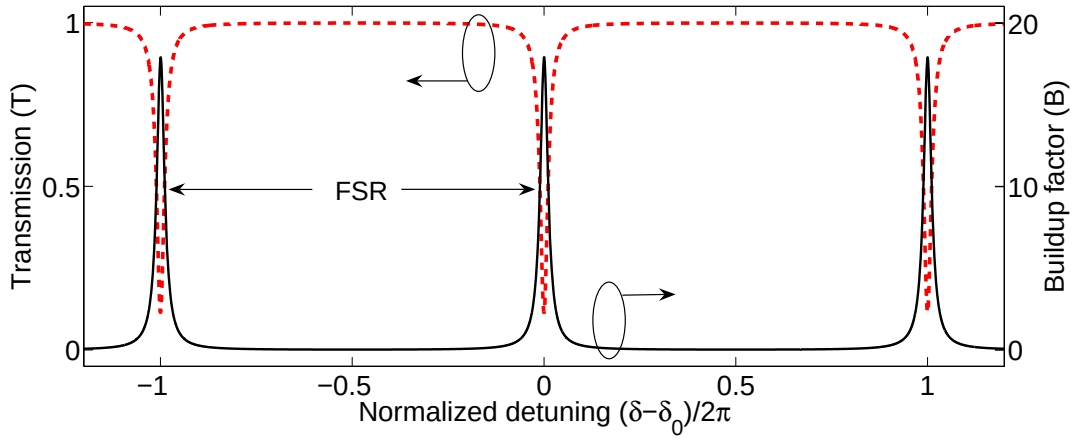

Fig. 2.7. Transmission (T) and buildup factor (B) as a function of δ in 1R1B device.

2.4.1 Buildup factor, Finesse and Quality factor

As discussed earlier, the resonant light can couple into the ring and acquire an effective $2m\pi$ phase response for each round trip, thus the constructive interference at the coupler port entering the ring ensures that the circulating optical intensity is coherently built up to a higher value than that of initially injected [3]. This accumulated intensity is described by the buildup factor (B), that is a square modulus of the circulating intensity divided by the incident intensity,

$$B=\left|\frac{E_3}{E_1}\right|^2=\left|\frac{it}{1-ar\exp(i\delta)}\right|^2=\frac{1-r^2}{1-2ar\cos\delta+a^2r^2}\xrightarrow{\delta=2m\pi,\,a\sim 1}=\frac{1+r}{1-r} \tag{2.14}$$

where the final result refers to the situation that the incident light is resonant in a lossless system. The 1R1B in these situations can obtain the maximum buildup factor that can be achieved. As one example illustrated in Fig. (2.7), the intensity inside the ring is ~19 times higher than the input light. This enhanced light can lead to a dramatically amplified nonlinear response [21] and multi-stability [9].

The sharply peak resonance in the buildup factor is characterized by a finesse parameter, which is defined as the ratio of FSR ($\delta_{FSR}=\delta_2-\delta_1=2\pi$) to the full-width at half-maximum (FWHM) of a resonance ($\Delta\delta_{FWHM}$). By expressing $\Delta\delta_{FWHM}$ in Taylor formula for resonance phase with $\cos\delta=1-\delta^2/2$ at Eq. (2.14), we have $\Delta\delta_{FWHM}=2(1-ar)/(ar)^{1/2}$. Then the finesse ($F$) is given by,

$$F \equiv \frac{2\pi}{\Delta\delta_{\mathrm{FWHM}}} = \frac{\pi\sqrt{ar}}{1-ar} \xrightarrow{a\sim 1} = \frac{\pi\sqrt{r}B}{1+r} \xrightarrow{r\sim 1} = \frac{\pi B}{2} \tag{2.15}$$

Similar to the finesse as a figure of merit related to resonance sharpness, the quality factor (Q) of a resonator is a measure of the resonance sharpness relative to its central resonance frequency (ω). The Q-factor is formally defined as the ratio between the stored energy circulating inside the resonator and the energy dissipated in one optical cycle [3],

$$Q \equiv \frac{\omega \times \text{Stored energy}}{\text{Power loss}} \tag{2.16}$$

Here, the dissipation of energy includes all the losses inside the ring and power coupled out into the bus waveguide. However, since the dissipation is a temporal phenomenon, we consider the analysis in reference [3] using the transient response to derive the general expression of Q-factor and explore more relations. On one hand, we assume the ring resonator has been charged to an intensity of $|E_0|^2$ before the input is switched off. Then the intensity stored in the ring after it travels the n^{th} round-trip is given by $|E_n|^2=\exp(-\alpha_{dis}L)|E_{n-1}|^2=\exp(-n\alpha_{dis}L)|E_0|^2$. Here we define the total loss coefficient $\alpha_{dis}=\alpha_{ring}+\alpha_e$, where α_e is the loss of energy responsible for the ring-bus coupling and it has the relation with r as $r=\exp(-\alpha_e L/2)$. If n is large enough, the variation of $|E_n|$ can be treated as a continuous variable $d|E_n|^2/dn=-\alpha_{dis}L|E_n|^2$. On the other hand, since the amount of power lost in one roundtrip is equivalent to the rate of energy variation during per roundtrip time (t_R), we can obtain $d|E_n|^2/dn=-t_R d|E_n|^2/dt$ by connecting the energy loss to power loss. Therefore, Q can be rewritten as,

$$Q = \frac{\omega|E_n|^2}{d|E_n|^2/dt} = \frac{\omega t_R|E_n|^2}{d|E_n|^2/dn} = \frac{\omega t_R}{\alpha_{dis}L} \tag{2.17}$$

Next, we recall the relation between the FWHM in round-trip phase response and angular frequency ($\delta=t_R\omega$), and apply relations of $r=\exp(-\alpha_e L/2)$ and $a=\exp(-\alpha_{ring}L/2)$ in the case of $\alpha_{dis}L \ll 1$, then arrive at the relationship between linewith and total loss coefficient,

$$\Delta\omega_{\mathrm{FWHM}} = \frac{\Delta\delta_{\mathrm{FWHM}}}{t_R} = \frac{2(1-ar)}{t_R\sqrt{ar}} = \frac{2\left[1-\exp(-\alpha_{dis}L/2)\right]}{t_R\exp(-\alpha_{dis}L/4)} = \frac{\alpha_{dis}L}{t_R} \tag{2.18}$$

Combining Eq. (2.17) and Eq. (2.18), as well as translating the frequency into wavelength using the relation $d\lambda=\lambda^2 d\omega/(2\pi c)$, where c is the speed of light in vacuum, we get the general expression of Q-factor defined in Eq. (2.16) as,

$$Q \equiv \frac{\delta}{\Delta\delta_{\mathrm{FWHM}}} = \frac{\omega}{\Delta\omega_{\mathrm{FWHM}}} = \frac{\lambda}{\Delta\lambda_{\mathrm{FWHM}}} \tag{2.19}$$

The relationship between the Q and F can be obtained as $Q=n_{\mathrm{eff}}L/\lambda F=mF$ by implementing Eq. (2.17) into Eq. (2.18) with $\delta=k_0 n_{\mathrm{eff}}L=t_R\omega$, where $m=n_{\mathrm{eff}}L/\lambda$ is the resonance order that directly relates the quality factor to the finesse. Also, the order is a measure of the number of wavelengths within the circumference and is indicative of the m^{th} peak in the transmission spectrum. The physical meaning of the Q and F can be explained in this way. If we define N as the effective number of round-trips required to reduce the energy to 1/e of its initial value, i.e., $\exp(-N\alpha_{\mathrm{dis}}L)=1/e$, we can solve N and express F in the terms of the loss coefficient α_{dis}. Then we have,

$$F = \frac{2\pi}{\alpha_{\mathrm{dis}}L} \Rightarrow F = 2\pi N \tag{2.20}$$

Eq. (2.20) tells us that the finesse represents the effective number of round-trips made by the resonant light in the ring multiplied by a factor of 2π. Similarly, the quality factor $Q=\omega t_R N$ represents the number of oscillations of the circulating field before being depleted to 1/e of the initial value. In other words, the F and Q respectively represent metrics for the intensity buildup and effective interaction time in a cavity resonator. The light interacts with the coupling interface for a finesse number of times while interacts with the ring interior for a quality number of cycles. This insight is very important for designing optical applications relying on the change of parameters of ring resonators [3, 6-8].

2.4.2 Effective phase response

The effective phase response is defined as the phase argument of the field transmission. If we rewrite Eq. (2.13) in a form of $E_2/E_1=e^{i(\pi+\delta)}(a-re^{-i\delta})/(1-are^{i\delta})$, the phase response ($\phi$) is deduced as,

$$\phi = \pi + \delta + \tan^{-1}\left(\frac{r\sin\delta}{a - r\cos\delta}\right) + \tan^{-1}\left(\frac{ar\sin\delta}{1 - ar\cos\delta}\right) \tag{2.21}$$

Eq. (2.21) is the phase shift acquired by light in passing through the 1R1B structure from the input port to the output port. It is a combination of three parts that can be understood in this way: the π is attributed to the twice cross-couplings of light before exiting the resonator, each of which imposes π/2 phase shift; the round-trip phase response δ is responsible for the light having to travel the ring one round before knowing whether it is on resonance; the last two $\tan^{-1}()$ terms are primarily dependent on the value of δ, which determines the resonant light and further determines the total phase response.

Fig. 2.8 presents the phase response of a 1R1B device for critical-coupled ($r=a$), under-coupled ($r>a$) and over-coupled ($r<a$) regimes. The critical-coupling implies the roundtrip absorption inside the cavity is

exactly equal to the amount of coupled energy. In this case, all the resonant light vanishes in the ring area and the transmission is zero. This is represented by the loss of phase information with a π discontinuity and the infinite phase sensitivity without bound. This critical-coupling is desirable for a filtering based on resonators to achieve 100% transfer of light. The under-coupling means the roundtrip absorption exceeds the coupled energy. Thus, there is almost no phase buildup and some counter-intuitive effects happen in this case, e.g., the phase response of the resonant light is unperturbed and the phase sensitivity has been inversed. The over-coupling means the roundtrip absorption is less than the coupled energy. There is a net optical field accumulation for the resonant light, which is reflected by a swing of 2π across the resonance in the phase spectrum. As shown in Fig. 2.8, under this over-coupled condition, the phase is significantly perturbed and the slope is sensitively dependent on the coupling strength. Such a phase sensitivity can be obtained by the normalized detuning derivative of the phase response,

$$\begin{aligned}\phi' \equiv \frac{d\phi}{d\delta} &= 1+\frac{ar\cos\delta - r^2}{a^2 - 2ar\cos\delta + r^2} + \frac{ar\cos\delta - a^2r^2}{1-2ar\cos\delta + a^2r^2} \\ &\xrightarrow{a\sim 1} = \frac{1-r^2}{1-2r\cos\delta + r^2} = B\end{aligned} \tag{2.22}$$

It is interesting to point out that, in the very low loss case (a~1), the phase sensitivity is identical with the buildup factor across the entire spectrum.

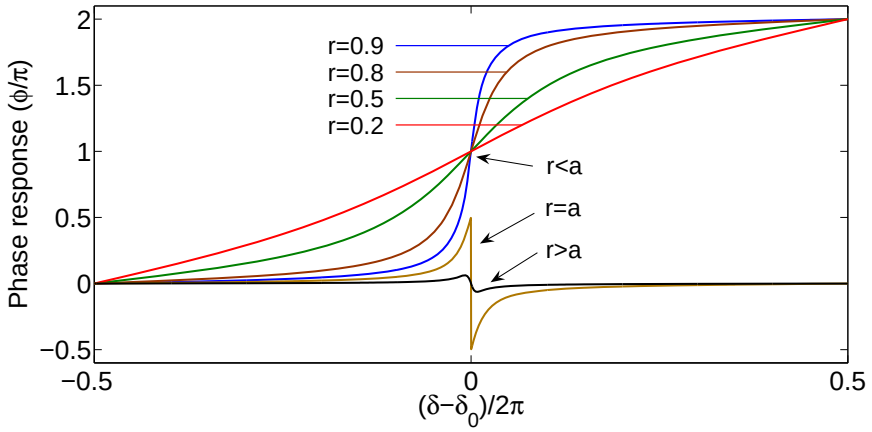

Fig. 2.8. Phase responses of 1R1B device at different coupling conditions (a=0.95).

2.4.3 Group delay

The phase sensitivity is directly related to the group delay of a resonant pulse that imposed by a ring. Such a group delay is given by differentiating the effective phase response to the angular frequency [3],

$$T_g \equiv \frac{d\phi}{d\omega} = \frac{d\phi}{d\delta}\frac{d\delta}{d\omega} = \phi' t_R \xrightarrow{a\sim 1} = Bt_R \tag{2.23}$$

We can see the group delay is interpreted as round-trip time enhanced by the phase sensitivity. The relation between delay and effective number of round-trips N can be obtained by applying the conversion between F and B from Eq. (2.17) and Eq. (2.18),

$$T_g \approx Bt_R = \frac{F(1-r^2)t_R}{\pi\sqrt{ar}(1-ar)} = \frac{2N(1-r^2)t_R}{\sqrt{ar}(1-ar)} \xrightarrow{a,r\sim 1} = 2Nt_R \tag{2.24}$$

Eq. (2.24) shows that the group delay approximately equals $2Nt_R$ in the lossless resonator when the coupling is very weak. Since an input pulse is being delayed in a resonator, i.e., its energy is stored and released by the ring, the group delay should be equal to twice of the cavity lifetime (t_{cav}) as $T_g=2t_{cav}=2Nt_R$, as verified by the last result in Eq. (2.24). Therefore, conversely, the phase sensitivity is expressed as the effective number of roundtrips that light travels inside the ring enhanced with a factor of two.

Furthermore, Eq. (2.24) tells us that the transmission of 1R1B is a sum of the delayed pulse inside the ring resonator, thus it is worth investigating the temporal output. To do this, we convert the normalized time domain ($t_n=t/t_R$) to normalized frequency domain (δ) using Fourier Transform,

$$F(\delta) = \sum_{-\infty}^{\infty} f(t_n)\exp(-i\delta t_n) \qquad T(t_n) = \frac{1}{2\pi}\sum_{-\infty}^{\infty} F(\delta) * T(\delta)\exp(it_n\delta) \tag{3.25}$$

where $T(\delta)$ is transmission in Eq. (2.13), $f(t_n)$ is the input Gaussian pulse and $T(t_n)$ is the temporal output.

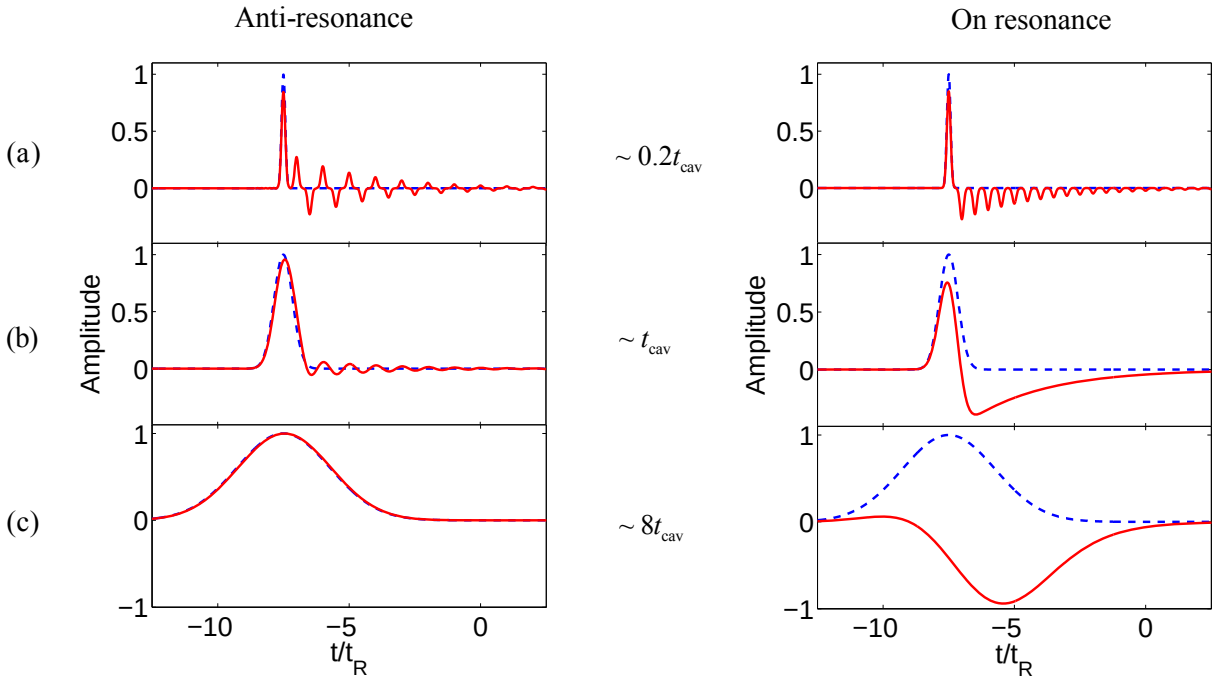

Fig. 2.9. Calculations of interfering output field amplitudes for anti-resonant and resonant light with three different injected pulse widths. The dashed lines are the incident pulse.

Fig. 2.9 presents the transmitted field amplitudes for three different pulse widths under anti-resonant and resonant conditions. In the anti-resonant case, as shown in Fig. 2.9(a), when the pulse width is less than the cavity lifetime, e.g., ~$0.2t_{cav}$, the amplitudes of subsequent impulses come out with alternating signs. The amplitude sign of first pulse is positive and that of the second one is negative, and so forth. This is due to the fact that the anti-resonant light obtains π [or $(2m+1)\pi$] phase shift for one round trip inside the ring and gets another π phase response originated from the twice cross-couplings at the

coupling interface. However, the situation is quite different for the resonant case. When the input signal is on resonance, all the amplitudes of the output pulse are negative, owing to each roundtrip involving twice cross-couplings and the $2m\pi$ effective phase shift (or zero phase shift) inside the ring. Fig. 2.9(b) and (c) show the outputs when the input pulse widths are ~t_{cav} and ~$8t_{cav}$, respectively. It is worth noting that, with the increase of the pulse width to a value larger than the cavity lifetime, the subsequent impulses destructively interfere at the output port to form an undisturbed pulse in the anti-resonant case, while constructively interfere to form a delayed (and inverted) pulse in the resonant case [3]. The delay of the pulse is applicable for all-optical buffering in integration of optical devices [28-31].

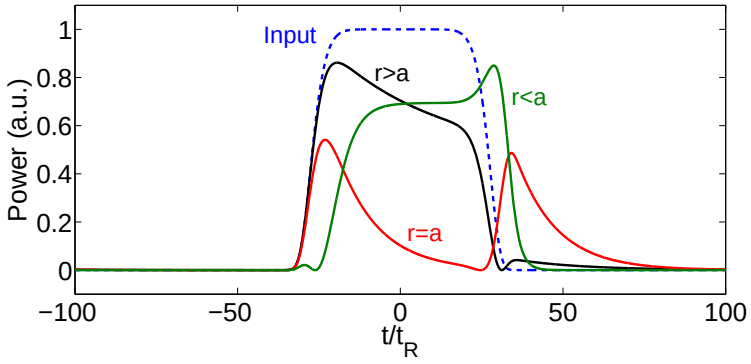

Fig. 2.10. Linear time responses of 1R1B device in three different coupling situations.

Fig. 2.10 shows the temporal response of a super-Gaussian pulse $\{f(t_n)=T_0\exp[(t_n-t_0)/\sigma]^n$, n>2$\}$ after passing through 1R1B under different coupling conditions. When a critical-coupling ($r=a$) happens, the complete resonant absorption inside the resonator renders no output in the center of the pulse and a rapid decay in the pulse amplitude. However, in under-coupled ($r>a$) and over-coupled ($r<a$) cases, the shape of output pulse remains similar to the input pulse except some slight sidelobes and distortion caused by high-order dispersion. The main difference between the two cases lies in the opposite sidelobes and group delay. The difference in sidelobes is on account of different coupling strengths r. The larger r implies less light couples into the ring and more light in the transmitted output. The negative delay in the under-coupled case is named as fast light and the positive delay in the over-coupled case is named as slow light. This theoretical prediction is consistent with the experimental observation in ring resonators [50].

2.5 One-ring-two-bus

The one ring side-coupled to two waveguides (1R2B) structure is shown in Fig. 2.11. The 1R2B is analogue to the FP etalon with two couplers behaving as the two partial reflective mirrors. The difference is the through (drop) transmission in 1R2B refers to the reflection (through) in FP etalon. The 1R2B is also named as add-drop resonator since the resonant light can be transferred from the input port to the drop port through the ring, as highlighted in the panel of Fig. 2.11. For simplicity, the two bus-ring couplers are assumed identical. With the feedback field related by the coupling matrices $E_6=E_3a^{1/2}\exp(i\delta/2)$ and $E_4=E_5a^{1/2}\exp(i\delta/2)$, the normalized through (T) and drop (D) transmission are deduced as,

$$T=\left|\frac{E_2}{E_1}\right|^2=\left|\frac{r-ra\exp(i\delta)}{1-r^2a\exp(i\delta)}\right|^2=\frac{r^2-2ar\cos\delta+a^2r^2}{1-2ar^2\cos\delta+a^2r^4}$$
$$D=\left|\frac{E_8}{E_1}\right|^2=\left|\frac{-t^2a^{1/2}\exp(i\delta/2)}{1-r^2a\exp(i\delta)}\right|^2=\frac{(1-r^2)^2a}{1-2ar^2\cos\delta+a^2r^4} \quad (2.26)$$

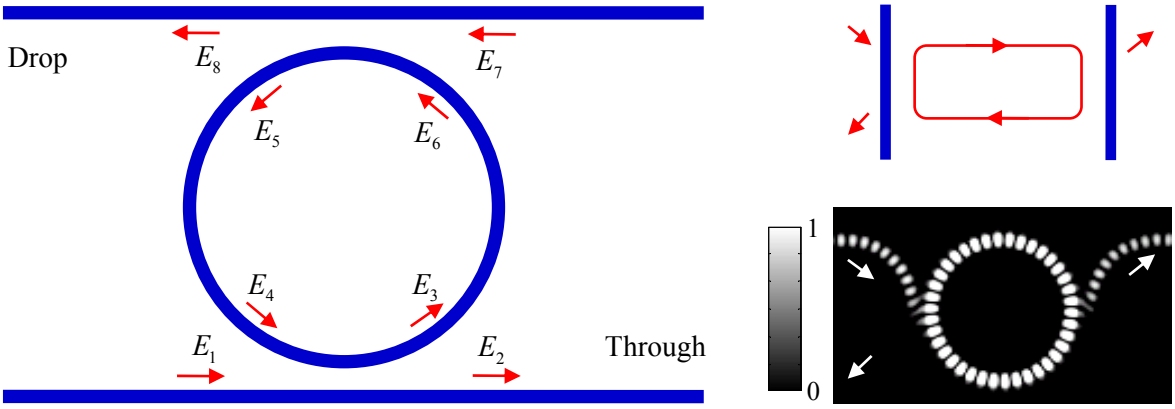

Fig. 2.11. Left: Schematic of 1R2B configuration. Right: (upper) 1R2B is equivalent with FP etalon; (lower) Power distribution of 1R2B device at resonance.

2.5.1 Effective phase response

If we express the transmissions in Eq. (2.26) in the alternative forms of $E_2/E_1=re^{i(\pi+\delta)}(a-e^{-i\delta})/(1-r^2ae^{i\delta})$ and $E_8/E_1=e^{i(\pi+\delta/2)}/(1-r^2ae^{i\delta})$, the corresponding effective phase response in the through transmission (ϕ_T) and drop output (ϕ_D) are given by,

$$\phi_T=\pi+\delta+\tan^{-1}\left(\frac{\sin\delta}{a-\cos\delta}\right)+\tan^{-1}\left(\frac{r^2a\sin\delta}{1-r^2a\cos\delta}\right)$$
$$\phi_D=\pi+\delta/2+\tan^{-1}\left(\frac{r^2a\sin\delta}{1-r^2a\cos\delta}\right) \quad (2.27)$$

In Eq. (2.27), ϕ_T has a similar formula with the phase response of 1R1B, and the δ/2 in ϕ_D is attributed to the fact that the resonant light travels half ring before entering the drop port. Fig. 2.12 shows the transmissions and associated phase shifts of 1R2B device. When the launched light is off resonant, it seems the light passes along the input bus directly to the through port, thus there is no phase accumulation for both the through and drop transmissions ($\phi_{T,D}$~0). In the case of on resonance, the resonant light interferences destructively with previous delayed pulse at the through port, inducing dips in the through spectrum, and interferences constructively in the drop port, forming corresponding peaks in the drop spectrum. If there is no coupling loss and no absorption in the cavity, the total power in through and drop ports is equal to unity $D+T=1$. However, due to the presence of losses, the resonant light cannot be completely guided to the drop channel and the total power is no longer equal to one. That is why the spectra in Fig. (2.12) show the resonant peaks less than one while the resonant dips close to zero. In the phase response, the resonant peaks give a ~π phase swing in the drop output and the resonant dips give a

~π phase jump in the through transmission. The π amount of the phase shift comes from the two cross-couplings of the resonant light before exiting the 1R2B configuration.

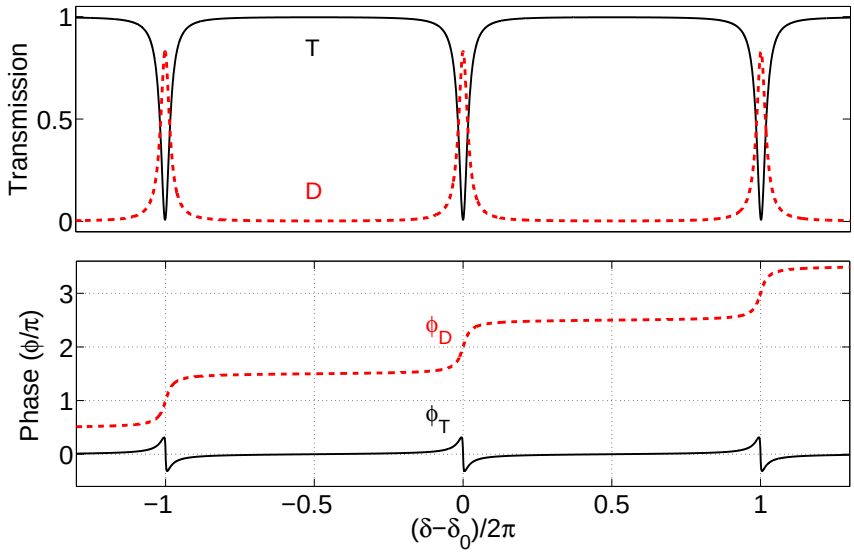

Fig. 2.12. (a) Through (*T*) and drop (*D*) transmissions of 1R2B configuration, and (b) phase responses,

2.5.2 Buildup factor, Finesse and Quality factor

Similar to the 1R1B case, the buildup factor (*B*), the finesse (*F*) and quality factor (*Q*) of 1R2B device can be deduced respectively as,

$$B=\left|\frac{E_3}{E_1}\right|^2=\left|\frac{it}{1-ar^2\exp(i\delta)}\right|=\frac{1-r^2}{1-2ar^2\cos\delta+a^2r^4}$$
$$F=\frac{2\pi}{\Delta\delta_{\mathrm{FWHM}}}=\frac{\pi r\sqrt{a}}{1-ar^2}=\pi B \qquad (2.28)$$
$$Q=\frac{\delta}{\Delta\delta_{\mathrm{FWHM}}}=\frac{2\pi nL/\lambda}{2(1-ar^2)/r\sqrt{a}}=mF$$

where $\Delta\delta_{\mathrm{FWHM}}=2(1-ar^2)/(ra^{1/2})$ is the FWHM of *B*. Eq. (2.28) tells us that the relations between the finesse buildup factor and quality factor of a 1R2B are analogous with those of a 1R1B structure. The comparison of the specifications in above equations and those of 1R1B reveals that the only difference between them is the coupling strength r^2, which is caused by twice ring-bus couplings in 1R2B device.

2.6 Summary

In this chapter, we have introduced the waveguide mode theory and EIM for single optical waveguides, and coupled-mode theory for parallel-coupled waveguides. The fundamental specifications associated with two basic single-cavity structures, 1R1B and 1R2B, like the transmission, effective phase response, buildup factor, finesse, quality factor and group delay, are investigated.

Chapter 3 Coupled Resonator Induced Transparency in Ring-Bus-Ring Mach-Zehnder Interferometer

3.1 Introduction

In this chapter, we propose a ring-bus-ring (RBR) configuration [see Fig. 3.1(a)], which consists of two resonators indirectly coupled by a tri-coupler formed between two resonators and one bus waveguide between them, and show that such a structure is capable of generating CRIT resonance when it is coupled to a Mach-Zehnder interferometer (RBRMZI), as schematically drawn in Fig. 3.1(b). Similar to many two-cavity systems in the references [9, 10], the RBR geometry also provides two resonant optical pathways P1 and P2 corresponding to dominant light localization in Ring 1 (R1) and Ring 2 (R2), respectively [see Fig. 3.1(c)]. Unlike in mutually coupled resonators where the field acquires π/2 phase shift as it cross-couples from one resonator to another, the double coupling in the tri-coupler imparts π phase shift to the coupling fields. As will be shown later, this π phase shift is responsible for generating narrow and almost loss independent transmission spectrum in RBRMZI. First, we present the theoretical model of the RBR device based on transfer matrix formalism (TMF). Then, we integrate the RBR with MZI and present its various transmission characteristics. Finally, the good agreements between the TMF theoretical prediction and 2D-FDTD simulation results for RBR and RBRMZI systems are given.

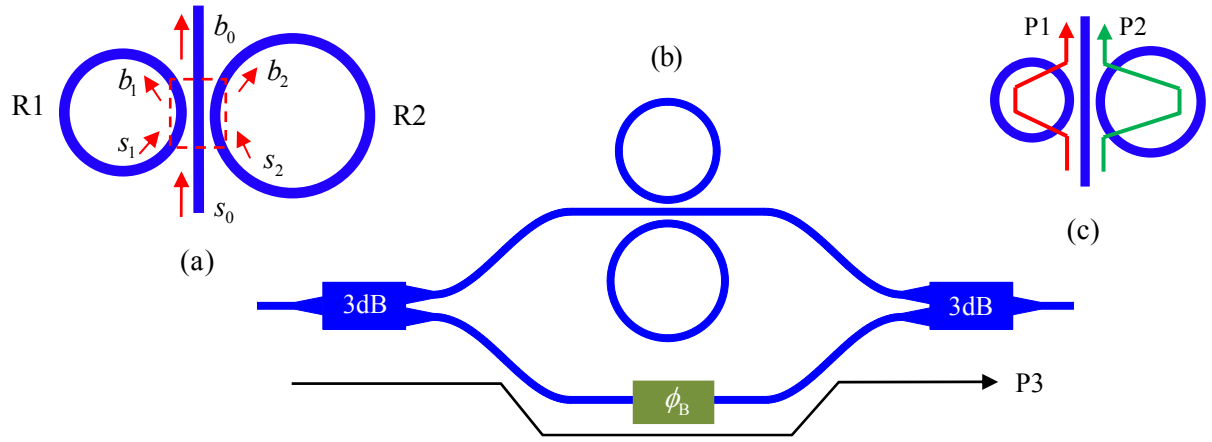

Fig. 3.1. (a) Geometrical scheme of the RBR configuration and six fields inside it, where the dashed box indicates the tri-coupler. (b) Proposed RBRMZI structure with the third optical pathway (P3) in the MZI. (c) Two possible optical pathways (P1 and P2) excited in the RBR structure.

3.2 Ring-bus-ring

The spectrum of the RBR structure can be easily obtained by transfer matrix analysis. The tri-coupler is schematically indicated in Fig. 3.1(a), showing there are six fields involved in the coupling process. The general derivation of field coupling of three parallel waveguides has been well studied in coupled-mode theory formalism [54], giving results in coupling matrix. In theory, the coupling of fields may occur for any combination of two out of three fields. However, in realistic case, the coupling is only noticeable

for two adjacent fields, and the coupling between R1 and R2 is very weak. This property is exploited to simplify our calculation, so that the coupling matrix for the tri-coupler can be expressed as,

$$\begin{bmatrix} b_1 \\ b_0 \\ b_2 \end{bmatrix} = \begin{bmatrix} r_1 & it_1 & t_{12} \\ it_1 & r_0 & it_2 \\ t_{12} & it_2 & r_2 \end{bmatrix} \begin{bmatrix} s_1 \\ s_0 \\ s_2 \end{bmatrix} \tag{3.1}$$

where r denotes the reflection-coupling elements of the center waveguide (r_0), R1 (r_1), and R2 (r_2), while the t denotes the cross-coupling elements between R1 (R2) and the center waveguide t_1 (t_2), and between the R1 and R2 (t_{12}) [refer to Appendix A for detailed derivation]. The input and output amplitudes are the denoted $s_{1,2,3}$ and $b_{1,2,3}$, respectively. Referring to Fig. 3.1(a), the output fields ($b_{1,2}$) and the input fields ($s_{1,2}$) are related via feedback relationships, i.e., $s_{1,2}=b_{1,2}A_{1,2}=b_{1,2}a_{1,2}\exp(-i\delta_{1,2})$. $a_{1,2}=\exp(-\alpha_{ring}L_{1,2}/2)$ are the round-trip amplitude transmission factors (a=1 in lossless situations), α_{ring} is the power loss coefficient and $L_{1,2}$ are the ring circumferences. $\delta_{1,2}=\kappa_0 n_{eff}L_{1,2}$ are the round-trip phase responses, where κ_0 is the propagation vector in free space and n_{eff} is the effective index. Thus, by solving Eq. (3.1), one may obtain the following set of equations,

$$\begin{aligned} &s_1 = \frac{(it_1 s_0 + t_{12} s_2)A_1}{1 - r_1 A_1}, \; s_2 = \frac{(it_0 s_0 + t_{21} s_1)A_2}{1 - r_0 A_2}, \\ &b_0 = r_0 s_0 + it_1 s_1 + it_2 s_2. \end{aligned} \tag{3.2}$$

from which the through transmittance of the RBR (T_{RBR}) based on tri-coupler is deduced by applying the relationships in Eq. (A11) as,

$$T_{RBR} \equiv \left|t_{RBR}\right|^2 = \left|\frac{b_0}{s_0}\right|^2 = \left|\frac{r_0 - r_2 A_1 - r_1 A_2 + A_1 A_2}{1 - r_1 A_1 - r_2 A_2 + r_0 A_1 A_2}\right|^2 \tag{3.3}$$

with corresponding phase response of,

$$\begin{aligned} \phi_{RBR} = &-\tan^{-1}\left[\frac{a_1 r_2 \sin\delta_1 + a_2 r_1 \sin\delta_2 - a_1 a_2 \sin(\delta_1 + \delta_2)}{r_0 - \left(a_1 r_2 \cos\delta_1 + a_2 r_1 \cos\delta_2 - a_1 a_2 \cos(\delta_1 + \delta_2)\right)}\right] \\ &+ \tan^{-1}\left[\frac{a_1 r_1 \sin\delta_1 + a_2 r_2 \sin\delta_2 - r_0 a_1 a_2 \sin(\delta_1 + \delta_2)}{1 - \left(a_1 r_1 \cos\delta_1 + a_2 r_2 \cos\delta_2 - r_0 a_1 a_2 \cos(\delta_1 + \delta_2)\right)}\right] \end{aligned} \tag{3.4}$$

It should be noted that Eq. (3.3) and Eq. (3.4) look similar to the transmittance and the phase response of one-ring coupled to one bus waveguide (1R1B), but slightly modified due to the contribution of the resonant process of R1 (r_1A_1), R2 (r_2A_2) and the mixture of the two ($r_0A_1A_2$). This can also be referred from the phase response where $\theta=\delta_1+\delta_2$. Correspondingly, the buildup factor for each ring ($B_{1,2}$) is also affected by the presence of the other ring, as shown in the following formula,

$$B_1 = \left|\frac{b_1}{s_0}\right|^2 = \left|\frac{it_1(1 - A_2)}{1 - r_1 A_1 - r_2 A_2 + r_0 A_1 A_2}\right|^2, \; B_2 = \left|\frac{b_2}{s_0}\right|^2 = \left|\frac{it_2(1 - A_1)}{1 - r_1 A_1 - r_2 A_2 + r_0 A_1 A_2}\right|^2. \tag{3.5}$$

And the light intensity distribution in the RBR can be estimated by using the relative intensity buildup B_{21}, defined as the ratio of the light intensity accumulated in R2 relative to that in R1 in a lossless case,

$$B_{21} = \frac{B_2}{B_1} = \left|\frac{it_2(1-A_1)}{it_1(1-A_2)}\right|^2 \xrightarrow{a_{1,2}\sim 1} = \left(\frac{t_2}{t_1}\right)^2 \left[\frac{\sin(\delta_1/2)}{\sin(\delta_2/2)}\right]^2 \tag{3.6}$$

In the case of identical rings (for the same coupling, t_1=t_2), it is expected that the light is equally distributed within RBR because of symmetry reason. This is different in the non-identical case ($\delta_1 \neq \delta_2$), which gives asymmetric intensity distribution. Near R1 resonance [$\sin(\delta_1/2)\sim 0$)], the dominant light distribution is expected to be in Ring 1, whereas near R2 resonance [$\sin(\delta_2/2)\sim 0$], it is the opposite. Thus, the light intensity distribution within RBR is crucially dependent on the detuning of the resonance frequencies of the two rings, which in this thesis is denoted by γ, defined as the ratio of the roundtrip phase (or ring circumference) of the two rings,

$$\gamma \equiv \delta_2 / \delta_1 = L_2 / L_1 \tag{3.7}$$

The general spectral characteristics of RBR are shown in Fig. 3.2(a). The resonance order is chosen to be about 120 to reflect the typical dimensions of fabricated ring resonators (e.g., 5μm radius). When the two rings are identical (γ=1), expression of the through transmission, intensity buildup factor and relative buildup factor can be simplified as,

$$T = \left|\frac{r_0 - A_1}{1 - r_0 A_1}\right|^2,\ B_{1,2} = \left|\frac{t_{1,2} A_1}{1 - r_0 A_1}\right|^2,\ B_{21} = \left(\frac{t_2}{t_1}\right)^2. \tag{3.8}$$

Here, the coupling coefficient $r_{1,2}$ are simplified by the relation r_1+r_2=r_0+1 in Eq. (A10). Because there is no distinction between the two rings in γ=1, the cavity system can be treated as if the system only consists of one cavity with the effective coupling coefficient r_0, hence imitating the behavior of 1R1B system. This is shown in Eq. (3.8), where the expression for the through transmission is identical to that in 1R1B. In the RBR device, generally, the located light intensity in each ring for γ=1 is dependent on the coupling constant of each ring $t_{1,2}$, as illustrated by the relative buildup factor in Eq. (3.8). This is in consistency with the assumption that the inter-resonator coupling con only be facilitated by virtue of coupling to the intermediate center waveguide. In the special case where the tri-coupler is symmetric (t_1=t_2), B_{21} is unity and we have t_1^2=t_2^2=r_0^2/2, which implies that the value of the buildup factor in each ring is only half of that in 1R1B device [refer to Eq. (2.14)]. Therefore, at γ=1, the light equally splits to two rings and uniformly distributes in them, as shown in panel (1) of Fig. 3.2(c) where the fields calculated by 2D-FDTD simulation are equally confined in both rings.

Unlike in other two-cavity systems [9, 40, 44], there is no resonance splitting resulting from mutual coupling of identical rings (γ=1). However, we can have very similar patterns for slightly non-identical rings, although it is not caused by mutual resonance splitting, but rather by isolated resonances of the rings, which are situated at δ_1=$m2\pi$ (for R1) and δ_1=[round(γm)/γ]2π (for R2). Here the round() is the

function that rounds a number to its nearest integer, and m is an integer. This is shown in Fig. 3.2(a), where γ=1.05 and γ=1.1 are chosen as illustrations. When the resonances coincide, there is only resonant dip as in the γ=1 case. When the two resonances do not coincide, the spectra have two distinct resonances. The two individual resonances become more widely separated in the increasing resonance order (e.g., $\delta_1/2\pi$>120), which is attributable to the Vernier effect of the two resonators. The field distributions corresponding to such resonances of γ=1.05 are shown in the panels (2)-(4) of Fig. 3.2(c). The resonances near the isolated resonance frequency of R1 (δ_1/π=even) correspond to the dominant light localization in R1 [panel (2)], whereas the farther one corresponds to dominant light localization in R2 [panel (3)].

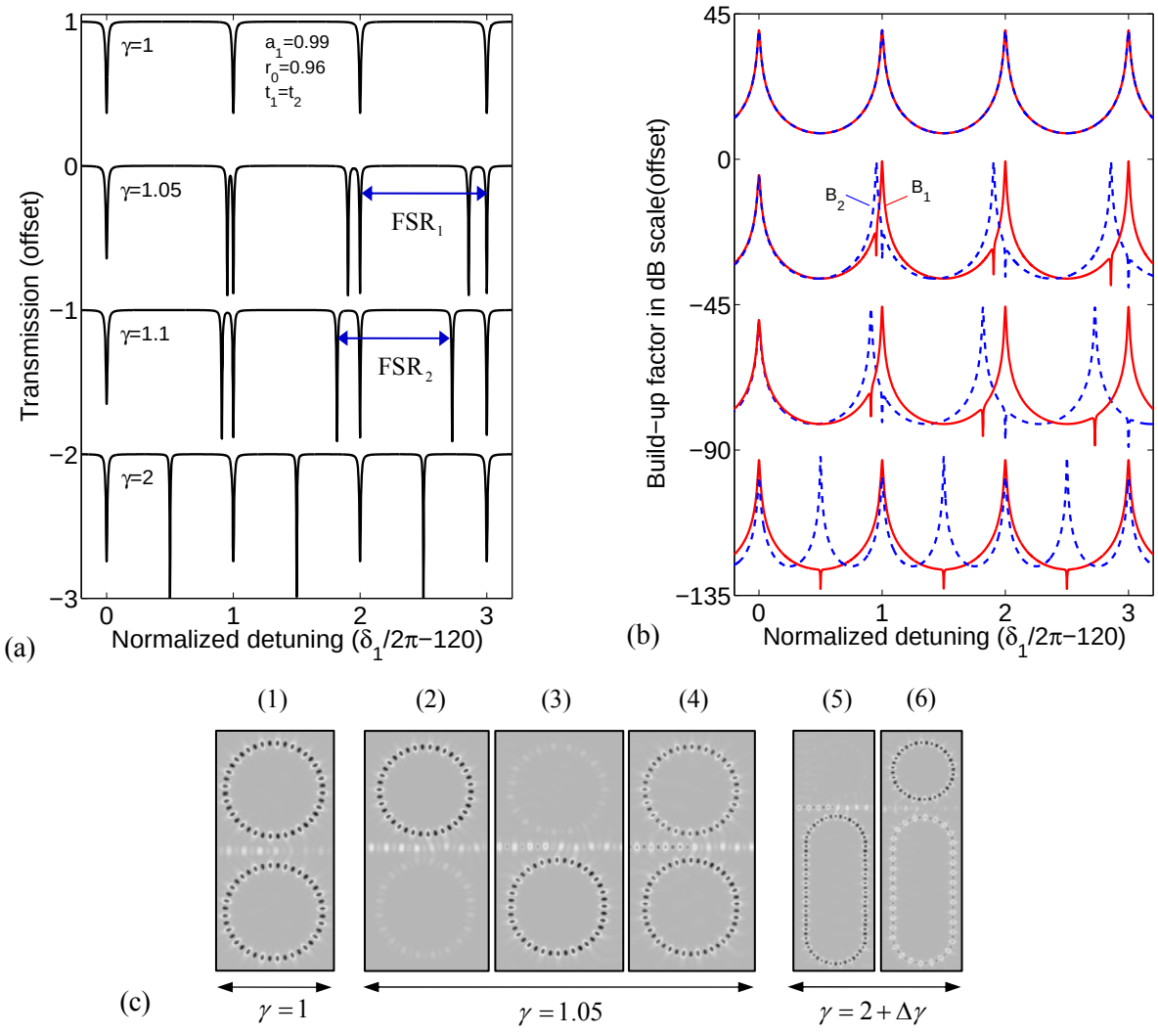

Fig. 3.2. (a) Transmission spectrum and (b) buildup factors for different values of γ. (c) Fields distribution for γ=1, γ=1.05 and γ=2+$\Delta\gamma$ as calculated using 2D-FDTD, where $\Delta\gamma$=0.006 is used to compensate the effect of coupling-induced phase shift [35].

For better illustration, the $B_{1,2}$ of the RBR device for the corresponding γ are shown in Fig. 3.2(b). It can be seen that the presence of resonant peaks in one ring corresponds to the presence of resonant dips in the intensity buildup of the other ring. This is attributable to the fact that the light acquires a π phase shift as it cross-couples two times from one ring to the other (each cross-coupling acquires $\pi/2$ phase shift),

which causes the two resonances to be in destructive interference. One special interest is that when the light is equally distributed within the RBR, as shown in panel (4) in Fig. 3.2(c). In this situation, the resonant light gains 2π phase jump as it has to cross-couple four times to go through both R1 and R2 for only once before exiting the structure. This is particular to the generation of EIT-like transmission in low-finesse ring resonators, as will be explained in the next section.

In the case of γ=2, there are two resonances in one free spectral range (FSR). One occurs at δ_1/π is odd, and the other one occurs at δ_1/π is even. At the location of δ_1/π is odd, the two resonators are completely isolated from each other since R2 is on resonance while R1 is on anti-resonance. This condition renders the light distribution is trapped more strongly in R2 [see panel (5) in Fig. 3.2(c)], giving the transmission spectrum similar to that of 1R1B with higher amplitude contrast and narrower linewidth. On the other hand, at the locations of δ_1/π is even, the resonant dips of both rings are overlapped with relatively different light intensities storing in each ring. At this case, if the two rings are equally placed with the center bus (r_1=r_2), then $B_{21}=a_1^2/(1+a_1)^2$ suggests that the light intensity circulated in R1 is approximately four times as that in R2 at low loss conditions, which can be verified by the simulated field distributions in panel (6) of Fig. 3.2(c).

From Fig. 3.2(a), we can observe that the resonance locations of R1 are fixed while the resonances spectrum of R2 move as γ is being varied. This is due to the fact that there exist two possible pathways in the RBR structure, as introduced earlier. This two-pathway property suggests the RBR structure is applicable for sensor application [55]. For instance, R1 is used as the reference ring and R2 is the sensing ring. The shift of coincident resonance is the detecting value, when γ changes during sensing. However, in comparison to the dual-ring coupled MZI in reference [55], the proposed RBR is more compact and favorable for device miniaturization. For better illustration the two pathways, we present a comparison between the transmissions of two standalone 1R1B devices with that of RBR structure, as shown in Fig. 3.3(a). Here, T1 and T2 denote the transmissions of two 1R1B devices involving R1 and R2, respectively. Also, the constructive interference between the two pathways P1 and P2 at the output end is attributed to the four times cross-couplings, which totally gives a 2π phase shift. Note that the slight shift between the RBR resonances and the standalone P1 (R1) and P2 (R2) resonances result from the modification of the 8-like round-trip path from the two rings [10]. Therefore, there is no phase difference for the resonant light passes through both rings in RBR or one ring in 1R1B configuration if the coupling-induced phase shift (CIPS) assumed to be absent. This explanation is verified by the FDTD calculation result shown in panel (4) at Fig. 3.2(c), where the field distributions is generally symmetrically located at the tri-coupler region with respect to the center waveguide. The explanation can also be supported by the coupling element (t_{12} and t_{21}) in Eq. (A8), which describes the coupling between R1 and R2 without additional transmission phase or imaginary part.

Fig. 3.3 (b) and (c) show the relative buildup B_{21} and the phase response of RBR compared to two individual 1R1B devices, respectively. The resonance spikes in the B_{21} spectrum imply that there are competing resonances between R1 and R2, since the light can only resonate in either one of the rings for

different operating frequency. For the phase responses, when the two resonances overlap (merging conditions), there is only 2π phase shift at the resonant order of 120, which accompanied with a 1R1B device under over-coupled conditions. This is clearly resembles the case ordinary 1R1B, as previously shown in Eq. (3.8). However, the phase response becomes qualitatively different when the two resonances are detuned from each other, producing a continuous or a step-like 4π phase shift where the $(2\pi+2\pi)$ come from the (P1+P2). As long as the resonance detuning is smaller than the resonance linewidth, the phase swing is characteristically linear with the slope inversely dependent on the resonance detuning of the two rings, which are indicated by the peaks and dips in relative intensify buildup. As the resonance detuning increases with increasing resonance order, we can expect the phase to become increasingly undulated, resembling more into isolated 1R1B structures. Later we will show that this 4π linear phase is particularly important in the phase engineering of the CRIT spectrum when the RBR is coupled to MZI.

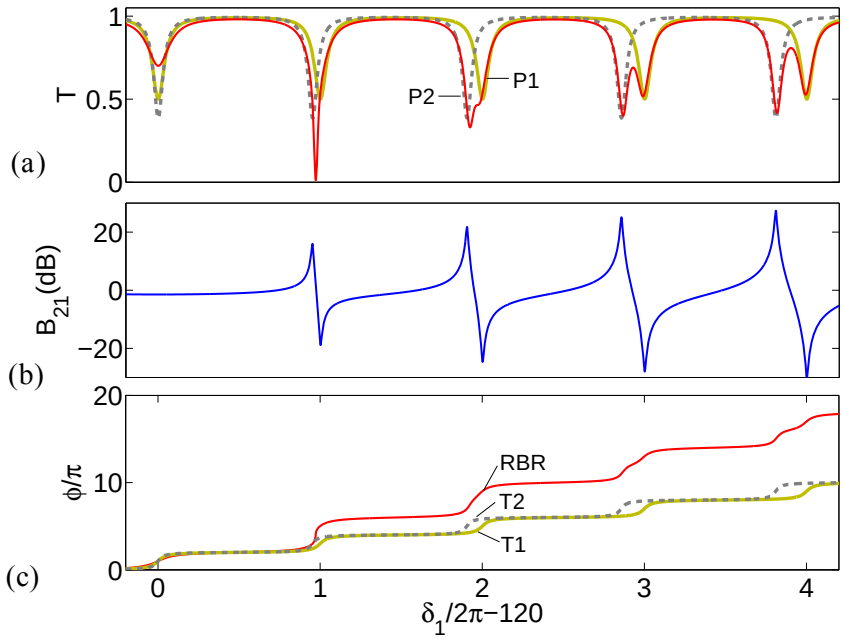

Fig. 3.3. (a) Comparison of transmissions between RBR and two standalone 1R1B structures. (b) B_{21} of RBR for detuned cavity resonance. (c) Phase response of RBR can be decomposed of the sum of phases came from R1 and R2. The γ=1.05, a_1=0.96, r_1=0.59 and r_2=0.52 are used.

3.4 Ring-bus-ring Mach-Zehnder interferometer

The EIT-like (or CRIT) spectrum characteristically consists of a linear phase in between two discontinuities, which translates into a transparent peak in between two resonant dips in amplitude spectrum [see Fig. 3.4(a)]. Therefore, in order to generate the CRIT spectrum, resonator systems with such phase discontinuity properties should be chosen. For better illustration, we compare RBRMZI with other two proposed structures in Fig. 3.4. In the two mutually coupled resonators system [40] [see Fig. 3.4(b)], for example, the phase discontinuity is obtained when one of the resonators is tuned to under-coupling situation, where the cavity loss dominates the coupling strength. On the other hand, in the cascade of two indirectly coupled resonators [45] [see Fig. 3.4(c)], the phase discontinuity naturally

occurs in the phase response of the through transmission (refer to Chapter 2 for detailed discussions of coupling conditions and phase responses). In the former case, the transparency is obtained by adjusting the inherent resonance splitting in between two resonators, whereas in the latter case, the transparent window is obtained by adjusting the resonance detuning between the two resonators. In previous section, we showed that the interference of two optical pathways within RBR can be used to generate a 4π linear phase swing as long as the detuning is small enough compared to the resonance linewidths. This phase response of RBR can be further engineered to match the CRIT phase requirement is the RBR is integrated with MZI, in which one of the MZI arms is side-coupled with the RBR [see Fig. 3.4(d)].

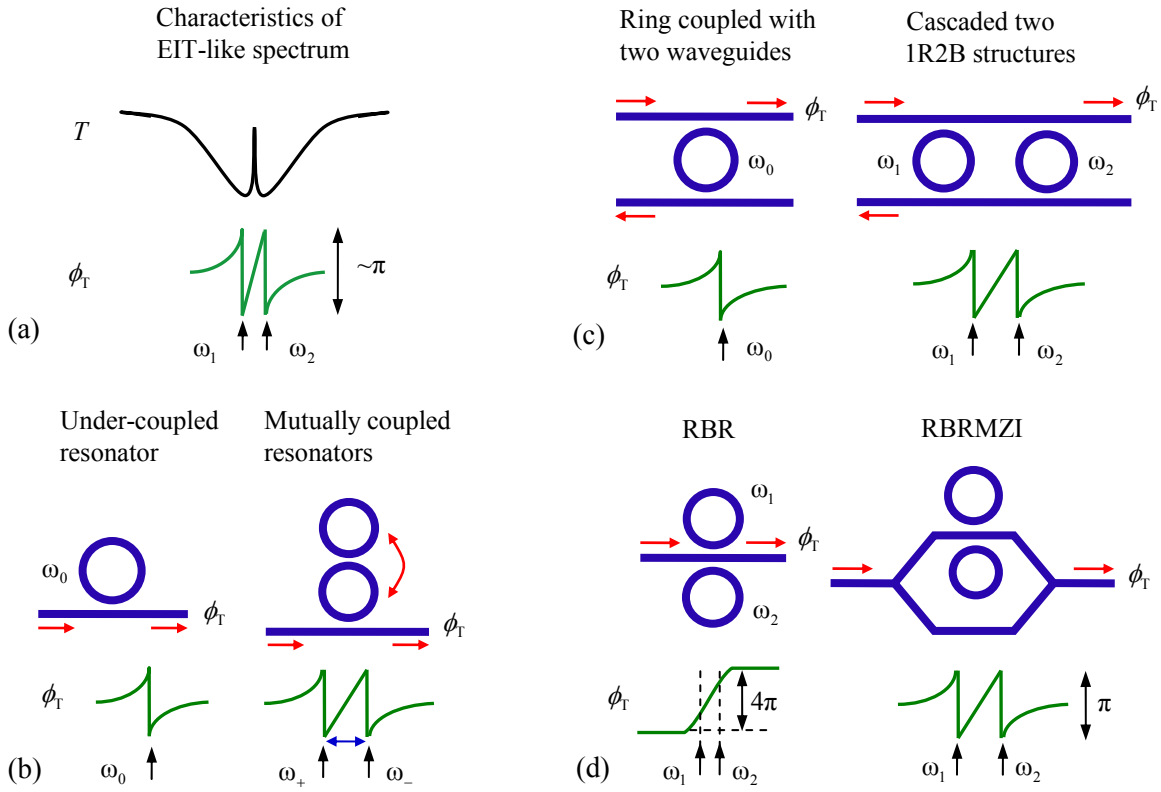

Fig. 3.4. (a) Characteristics of EIT-like amplitude and phase spectrum. Various realizations of EIT-like spectra in (b) two mutually coupled resonators [40], (c) cascade of two indirectly coupled resonators and (d) RBRMZI device.

The phase discontinuity is made possible because of additional non-resonant optical pathway (P3) in another MZI arm [see Fig. 1(b)], which results in a typical cosine-like MZI envelope. More generally, since the MZI itself may not be balanced due to fabrication variations and the presence of rings near one arm, this intrinsic asymmetry maybe represented by a phase bias (ϕ_B) in the other arm [36]. The transmission of RBRMZI (t_{MZI}) can be modeled with,

$$\begin{aligned} t_{MZI} &\equiv |t_{MZI}|\exp(i\phi_{MZI}) = \frac{i}{2}\left[t_{RBR} + \exp(i\phi_B)\right] \\ &= \frac{1}{2}\exp\left(i\frac{\phi_{RBR}+\phi_B+\pi}{2}\right)\left\{|t_{RBR}|\exp\left[i\left(\frac{\phi_{RBR}-\phi_B}{2}\right)\right] + \exp\left[-i\left(\frac{\phi_{RBR}-\phi_B}{2}\right)\right]\right\} \end{aligned} \tag{3.9}$$

In the situation of lossless RBR component ($a_{1,2}$=1, $|t_{RBR}|$=1) and balanced MZI (ϕ_B=0), the RBR transmission can be further simplified to a cosine term using the function of $e^{i\delta}+e^{-i\delta}=2\cos\delta$. Then the MZI transmission and phase response (ϕ_{MZI}) are simplified as,

$$t_{MZI}=\left|\cos\frac{\phi_{RBR}}{2}\right|\angle\phi_{MZI},\quad \phi_{MZI}=\frac{\pi}{2}+\frac{\phi_{RBR}}{2}+\cos^{-1}\left(\frac{\phi_{RBR}}{2}\right) \tag{3.10}$$

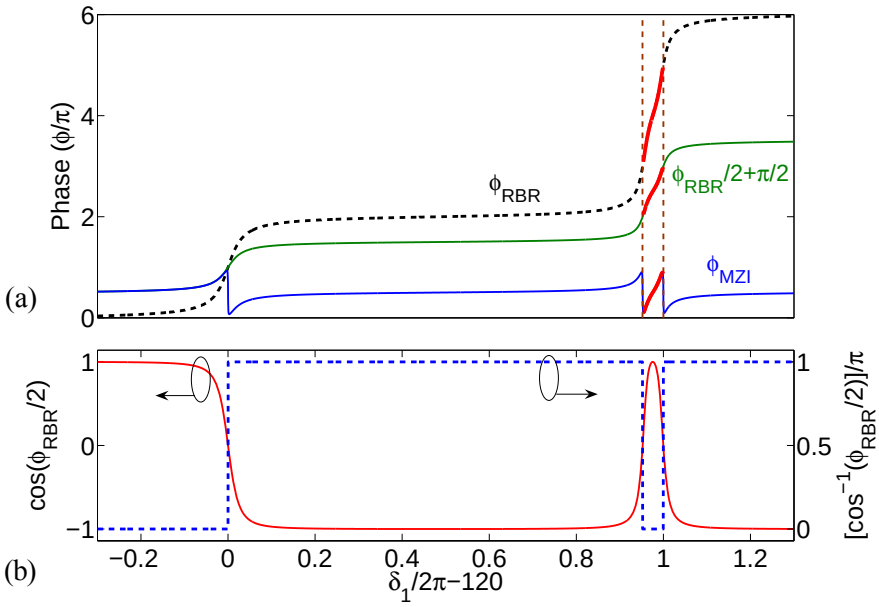

Fig. 3.5. (a) Profiles for three phase terms vs δ_1 (b) Phase and transmission of $\cos(\phi_{RBR}/2)$ vs δ_1.

The origin of the phase discontinuity in ϕ_{MZI} can be mathematically explained by the term $\cos(\phi_{RBR}/2)$ in Eq. (3.10). In order to illustrate the effects of phase on the emergence of transparent window, we plot the phase profile of RBR, MZI and the intermediate term, as shown in Fig. 3.5. Considering ϕ_{MZI} in Eq. (3.10), the summation of the first two terms is a continuous profile. The amplitude of $\cos(\phi_{RBR}/2)$ changes its sign at the positions of $\delta_1=m2\pi$ for R1 and δ_1=[round(γm/γ)] for R2 (m is an integer), hence giving corresponding phase jumps π at those positions. However, in the physical sense, the phenomenon can be explained by means of the two optical pathways (P1 and P2) in RBR interfere with the third non-resonant optical pathway in the other arm of MZI (P3) around the R1 and R2 resonances, respectively. In this situation, the output amplitude is zero and the phase information is lost, rendering the π phase jump of phase response. Therefore, the destructive interferences enhance the transparent peak in between the two closely spaced resonance locations, rendering a transparent window. The EIT-like resonance in RBRMZI has a similar feature with that in the cascaded 1R2B resonators, i.e., the two dips at both sides of the transparency window correspond to the two ring resonances. However, the difference between the two configurations lies in the fact that the phase discontinuities requirement in RBRMZI comes from the engineering of MZI, as illustrated in Fig. 3.4(d), instead of the light interaction in two rings alone. Note that this phase discontinuity is especially true for other resonator structures, such as the through transmission of 1R1B in critically coupled situation and 1R2B resonators at lossless case. Since the phase

discontinuity occurs in the cases of ϕ_{MZI} is an odd multiple of π i.e., $\phi_{MZI}=(2m+1)\pi$, it also follows the changes at the resonances of the two resonators ($\delta_1=2m\pi$) in RBR structure. Thus, the locations of the phase discontinuities can be controlled by changing the resonance frequency detuning between the two resonators, which in turn determines the linewidth of the CRIT transmission.

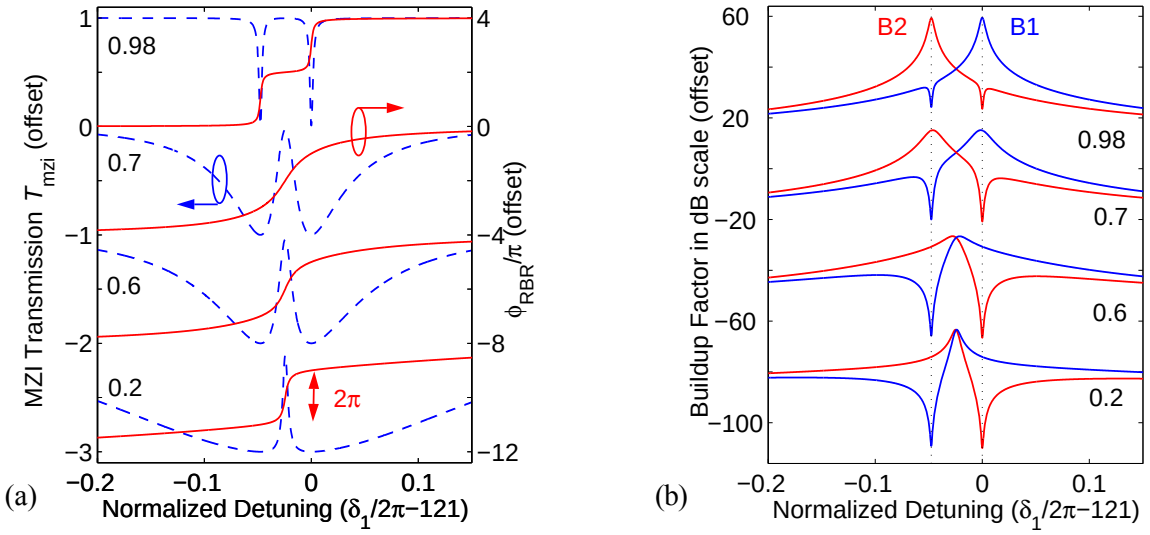

Fig. 3.6. (a) Transmission of lossless and balanced RBRMZI (T_{MZI}) for different r_0. (b) Plot of B_1 and B_2 buildup factors for corresponding r_0 values, where the dashed lines indicate the resonance locations.

Fig. 3.6(a) presents the CRIT transmissions and the phase responses of RBR section for different coupling strengths (r_0). Again, we choose γ=1.05 at the normalized frequency of $\delta_1/2\pi$ =121 for the purpose of illustration. It is important to note that the finesse of the transparent resonance increases along with increasing the coupling strength (or decreasing r_0) due to stronger interaction (more interaction) between the two rings via the tri-coupler. Furthermore, as illustrated in Fig. 3.6(a), the phase response of RBR structure (ϕ_{RBR}) becomes sharper in the enhancing the coupling strength. This is in contrast with other existing structure in Fig. 3.4(c), where low-finesse resonators do not provide sharp phase response. This difference can be explained by the way that the two resonators interact via the center waveguide in the RBR structure. When CRIT occurs, the light intensity is almost equally distributed in the two resonators [see panel (4) in Fig. 3.2(c)] and the light from the input waveguide cross-couples four times before exiting into the output waveguide. This means from the cross-coupling alone, the light acquires an abrupt phase change of 2π at the output port, and that the phase change is almost independent of the resonator finesse. In RBR device, since ϕ_{RBR} is a combination of resonant and non-resonant processes [see Eq. 3.4], the phase jump caused by cross-coupling is not so clearly seen in high finesse resonators, since the phase contribution resulting from resonant process is the predominant factor. It is only when the resonators have low finesse that the 2π phase jump due to cross-coupling can be observed, which is illustrated in the bottom panel in Fig. 3.6(a) where r_0=0.2.

Another perspective from the buildup factor profile is also presented in Fig. 3.6(b). When the two resonances are well separated relative to their broadening, we have the same situation as in Fig. 3.2(a),

where the peak of the intensity buildup in one ring translates into a dip on the other. Here, the dip serves as the resonant process, while the rest serves as the background spectrum. As the broadening of the two resonances increases, we can see that the resonant dips start to influence the background spectrum and induce spectrum asymmetricity. Note that this is a rather familiar situation found in ring-enhanced Mach-Zehnder interferometer (REMZI) [17], where asymmetric transmission spectrum is generated by inducing phase shift in one of MZI arms. Finally, when the two resonances are significantly broadened (e.g. at r_0=0.2), we can see that the peak of intensity buildup in both rings shifts to the center of the two resonances, which leads to CRIT in Fig. 3.6(a).

Note that manifesting phase discontinuity by a complete destructive interference is not exclusively RBRMZI. In fact, one should expect a similar phase response when a cascade of two resonators is side-coupled with one of the MZI arm, which is named as dual-resonator Mach-Zehnder interferometer (DRMZI) for convenience here. By side-coupling two identical resonators in one MZI arm, one can mimic the phase response of RBRMZI, but with one significant difference. In RBR, the two resonators interact indirectly through the center waveguide, which in turn gives a phase response consisting of contributions of the two resonators as well as the mixture resonant pathways [the term $\delta_1+\delta_2$ as shown in Eq. (3.4)]. In DRMZI, the phase contribution of one resonator does not affect the other, and thus the phase response simply consists of a summation of individual phase responses from each resonator. Since the phase slope of two side-coupled resonators would be about twice that of the individual ones, this means the finesse of CRIT generated by DRMZI is always limited to the finesse of the individual resonators. This is in qualitative difference with RBRMZI where the finesse of CRIT is progressively higher as the finesse of individual resonators decreases.

The comparison of RBRMZI and DRMZI is shown in Fig. 3.7(a), which plots the CRIT finesse (F), finesse enhancement (η), and the extinction ratio (ER) as a function of coupling coefficient (r_1). The finesse enhancement is defined as the ratio between the finesse of CRIT and the finesse of single side-coupled ring (1R1B) $\eta=F_{CRIT}/F_{1R1B}$, where $F_{CRIT}=2\pi/\delta_{FWHM}$ is the finesse of the CRIT transmission which has resonance linewidth of δ_{FWHM}, and $F_{1R1B}=\pi(a_1r_1)^{1/2}(1-a_1r_1)^{-1}$ is the finesse of a 1R1B taken from Eq. (2.15). The extinction ratio is defined as $ER=T_{MZI}(\delta_{CRIT})/T_{MZI}(\delta_{CRIT}\pm\Delta\delta)$, where δ_{CRIT} is the normalized frequency at which CRIT occurs, and $\Delta\delta$ is the detuning at which the background transmission spectrum is already present. In principle, one can choose any detuning value as long as it sufficiently represents the existence of background spectrum. Here, we choose the detuning to be $3/(2F_{CRIT})$, or $\Delta\omega=3\Delta\omega_{FWHM}/2$ in the absolute sense.

It can be clearly observed from Fig. 3.7(a) that, for DRMZI, the finesse increases with decreasing coupling strength, while the finesse enhancement is relatively constant. This is in contrast with RBRMZI, where the finesse and the finesse enhancement increase dramatically when the coupling strength is decreased. The relatively constant finesse enhancement in DRMZI shows that high finesse CRIT can only be generated out of high finesse background envelope, which means high background transmission, and results in low ER. This is confirmed in Fig. 3.7(a), where the ER of DRMZI is not more than ~20, while

that of RBRMZI can be as high as ~300. Such qualitative difference is illustrated in Fig. 3.7(b), where the CRIT transmissions of RBRMZI and DRMZI are plotted against the normalized detuning from the respective CRIT frequency. Here, the value of r_1 is chosen so that the finesse of both transmissions is the same (i.e., ~200). Clearly, it can be seen that the background spectrum of DRMZI is about 100 times higher compared to that of RBRMZI, which is consistent with ER in Fig. 3.7(a).

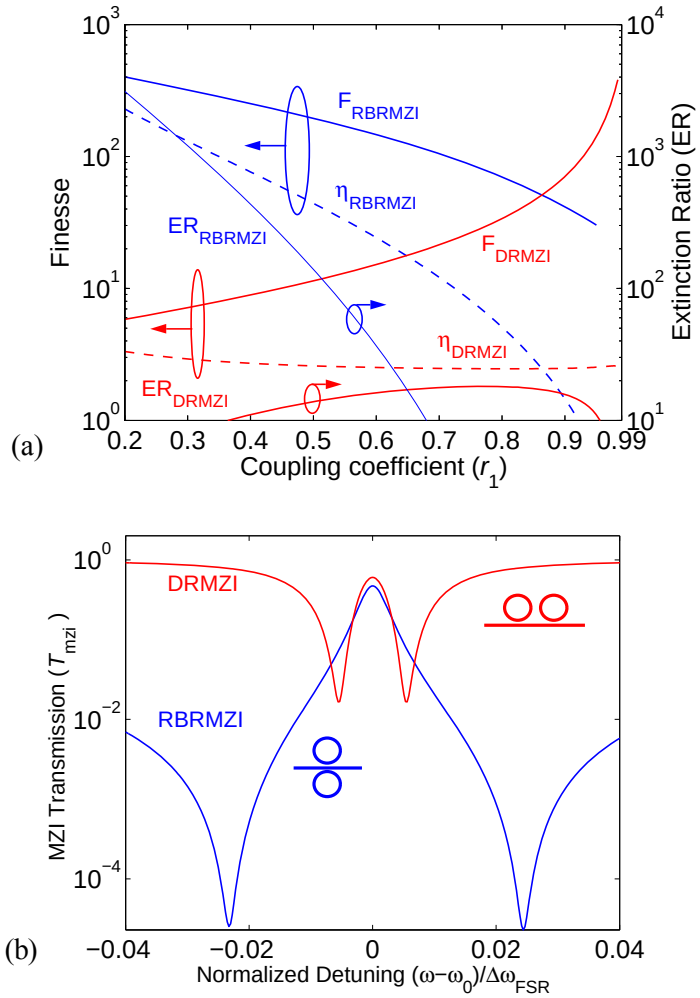

Fig. 3.7. (a) Calculated finesse, finesse enhancement, and extinction ratio of RBRMZI and DRMZI for a typical loss coefficient (a_1=0.995) as a function of coupling coefficient (r_1). (b) Comparison of transmission spectrum of RBRMZI and DRMZI for the same finesse (~200). It can be seen that the envelope effect in DRMZI is much more serious compared to that in RBRMZI.

3.5 Simulation results

In this section, we show that the analytical calculation agrees well with the FDTD numerical method. The simulation parameters are adopted based on the silicon-on-insulator (SOI) material platform (refer to Chapter 2). The 3D structure is reduced to a 2D structure by the effective index approximation, where the reduced index of the silicon core is n_{si}=2.841 for single quasi-TE mode. For design simplicity, the coupling strength for the two rings between the center waveguide are set to be identical (t_1=t_2) with a coupling length of L_C=6μm and a gap separation of g=200nm. The coupling length and the gap separation

can be further tuned to adjust the coupling conditions for fixed cavity lengths. The cavity circumference ratio of R1 and R2 is designed to be γ=1.05, using the quarter-round radius of 5μm. This radius is chosen to be 5μm so that the bending loss is negligible for SOI waveguides [32]. The RBRMZI consists of two 3dB multimode interferometer (MMI), which has a 3.5μm width and a 10.7μm length. The input/output MMI ports are tapered with a length of 5μm to minimize the insertion loss. A Gaussian input light pulse (λ_{center}=1550nm) is launched (based on the eigen-mode of the input waveguide) into the waveguide and the simulation grid size is made to be less than $\lambda/10n_{eff}$ for simulation accuracy.

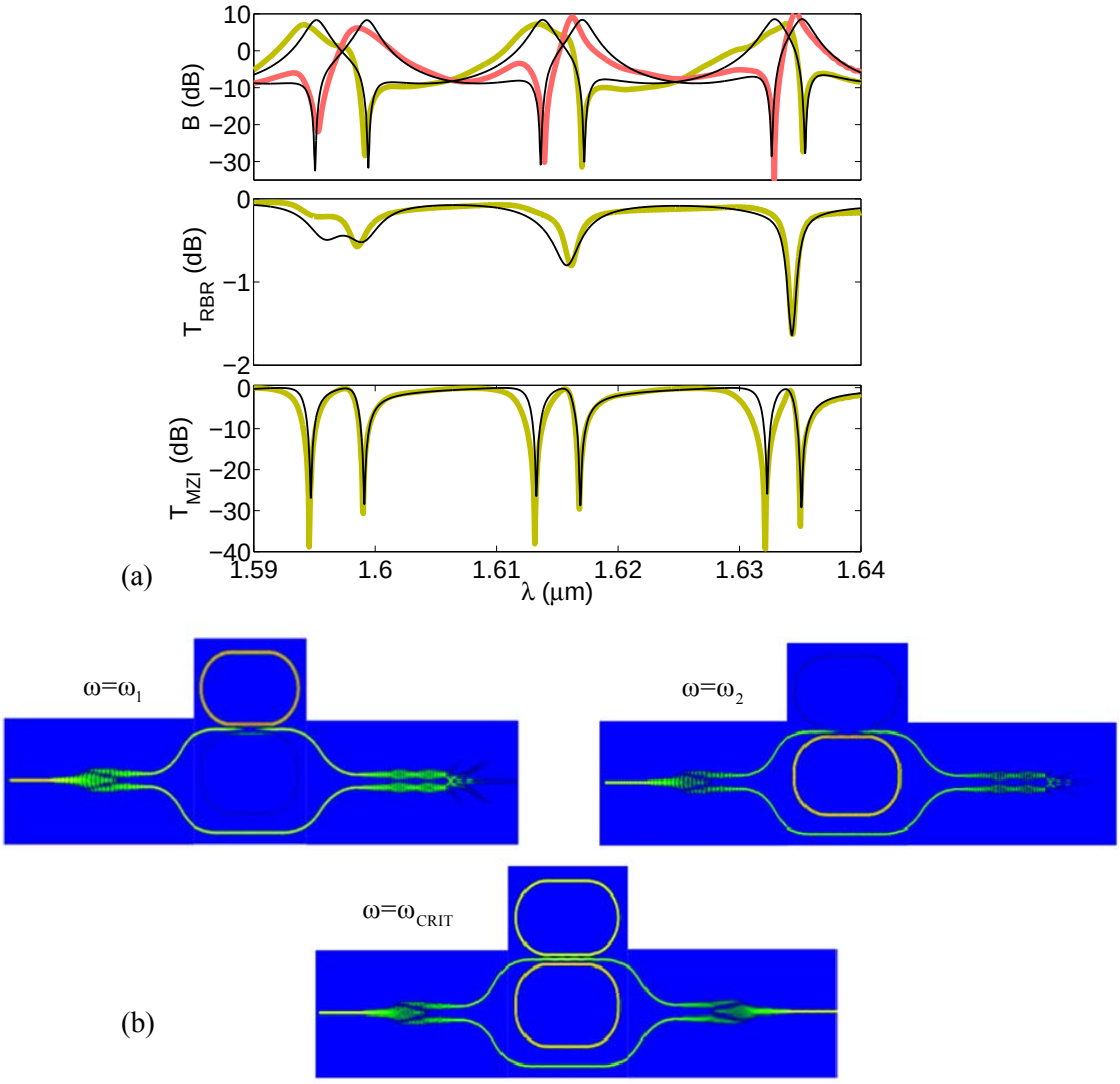

Fig. 3.8. (a) Comparison between the 2D-FDTD calculation results (thick faded) and the transfer matrix formalism (thin bold) for RBR and RBRMZI. (b) Intensity distributions (in dB scale) of RBRMZI for three different frequencies. Fitted loss and size detuning are a_1=0.99 and γ=1.0497,respectively.

Fig. 3.8(a) presents the simulation results of buildup factors and transmission for rather weakly coupling RBR and RBRMZI, which are theoretically fitted using the transfer matrix formalisms described earlier. To obtain a better fitting, the wavelength dependencies of effective index (n_{eff}) and coupling constant (r_0) are taken into account. From commercial mode solving, for the wavelength spectrum of

interest ($1.59<\lambda<1.64$), n_{eff} and r_0 can be numerically expressed as a function of λ as $n_{eff}(\lambda)=-1.247\lambda+4.258$ and $r_0(\lambda)=-4\lambda+6.693$ respectively, where λ is in microns. In general, the analytical formalism should agree well with the FDTD simulation results, except for some spectral non-idealities that have been overlooked in our model. For example, besides the nonzero transmission phases in coupling elements caused by the non-negligible overlap integrals and self-coupling coefficients in Eq. (A6), the coupling-induced phase shift (CIPS) from RBR perturbation in coupled MZI arm can also result in the transmission and buildup factor spectra to be asymmetric. This unexpected effect can be partly incorporated by introducing a phase bias (ϕ_B) between two MZI arms, whereϕ_B is around -0.25π for the fittings.

It can be seen from Fig. 3.8(a) that the transmission of RBR structure varies over different resonance orders. This is attributable to the fact that resonance detuning changes over the spectrum due to Vernier effect as described in Fig. 3.2(a). Around λ=1.595μm, one can see that the resonances are well detuned and RBR functions like two standalone 1R1B devices. This is manifested in two distinct resonant dips of different transmission contrast, since the two rings have different sizes and so have different effective cavity losses. Take the buildup factor for example, the B_1 spectrum is broader than B_2 due to the slight larger cavity size of R2 (γ>1). Consequently, the light resonates slightly longer in R2 and enhances the effective loss, giving a narrower resonant linewidth compared to that of R1. Similarly, the lower transmission dips in R2 resonance spectrum are due to the higher effective loss in R2. On the other hand, near λ=1.615μm and λ=1.635μm, the resonance detuning decreases and the RBR transmission begins to merge into a single resonant dip. The field intensity distributions of RBRMZI for three frequencies are shown in the panels of Fig. 3.8(b), which are similar to those in Fig. 3.2(c). The $\omega=\omega_1$ and $\omega=\omega_2$ correspond to the dominated light are in R1 and R2, respectively. The CRIT starts to occur near λ=1.635μm, albeit with high background spectrum. This is because the two resonators do not strongly interact, and thus result in a weak CRIT effect. The intensity distribution corresponding to CRIT is shown in the bottom panel.

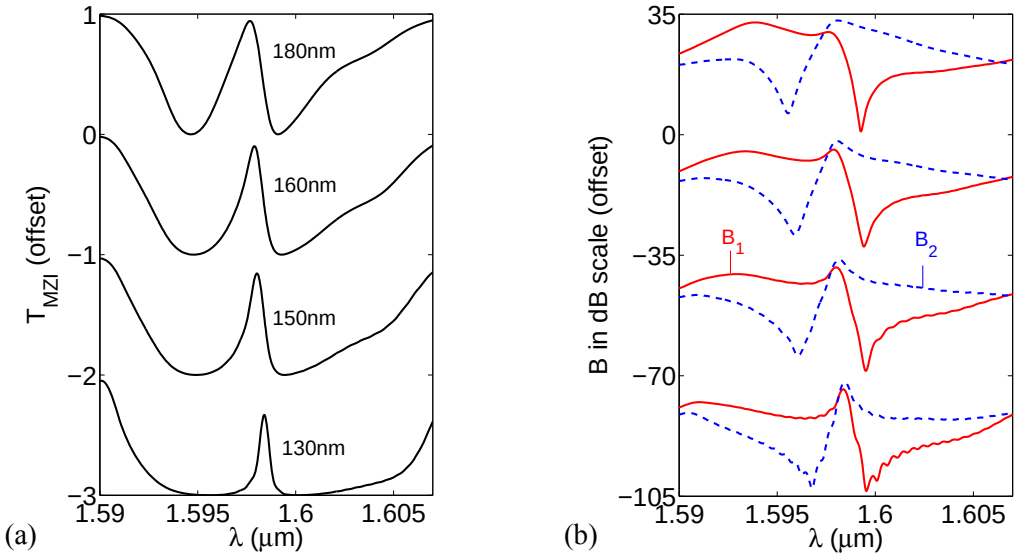

Fig. 3.9. (a) Simulated transmission of RBRMZI and, (b) buildup factors for different gaps (in μm).

As highlighted earlier in Fig. 3.6, the transparent window can be designed to be sharper and with narrower linewidth with stronger coupling strength. One method is to increase the coupling length within the range of beat length, and the other one is to decrease the coupling gap. In the later case, the resonance positions are fixed for better comparison using the same FSR. Fig. 3.9(a) shows the comparison of the CRIT for different gap separations, where the gap is varied gradually from 200nm down to 130nm. As expected, the FDTD calculation results show that the CRIT effect becomes stronger as indicated in decreasing resonance amplitude. Correspondingly, the simulated buildup factor for each gap separation is also shown in Fig. 3.9(b). It can also be seen that the buildup factor becomes significantly asymmetric when strong CRIT takes place (e.g., at the 130nm gap). It should be noted that the CRIT becomes increasingly asymmetric and the peak seems to shift to the longer wavelength as the coupling strength increases. As previously discussed, such a red shift of the CRIT is caused by the additional transmission phases in the RBR section and the imbalanced phase bias of two MZI arms. The increase in phase shift as the coupling strength increases inside the resonators modifies the resonance condition and consequently shifts the resonance wavelength. Such a shift can also be referred to the movement of the dips in buildup factor B_2 with different gap separations.

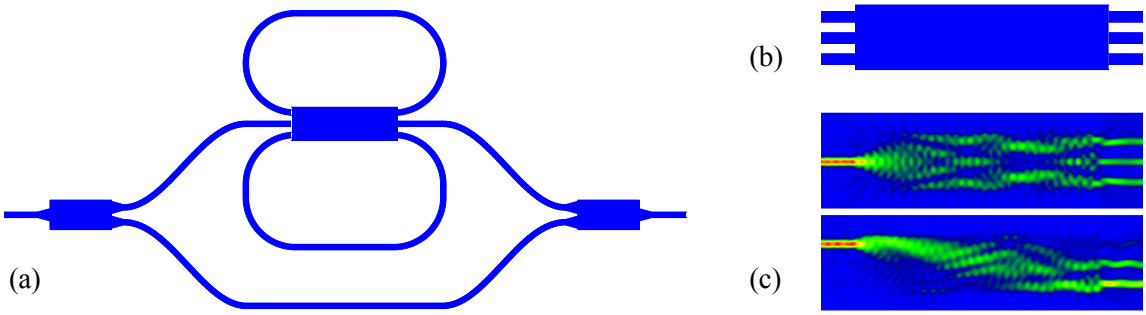

Fig. 3.10. (a) Schematic of RBRMZI integrated with a 3×3 MMI coupler. (b) A close-up of the MMI coupler. (c) Calculated intensity distributions of MMI with lunched input light from different channels.

In fabrication, even though many microring resonator-based devices have been realized upon various material platforms, the desired characteristics of resonators could be degraded due to the narrow gap separations in the directional coupler region. For instance, in the SOI material, it shows that the non-adiabatic mode transition at the coupler section will cause large excess mode conversion losses when a narrow gap is used, e.g., g<100nm [56]. Furthermore, the fabricated directional couplers may fuse together as a slab waveguide, which seriously destroys the expected properties of structures. MMI coupler, as one potential alternative type of couplers, has been theoretically and experimentally employed in SOI ring resonators [57-58]. The MMI coupler has the advantage of high fabrication tolerance due to its low sensitivity to the wavelength and polarization variations. As a general guideline, we can apply a 3×3 MMI coupler instead of the directional tri-coupler into the RBRMZI, as shown in Fig. 3.10(a). The MMI section has a width of 2.7μm and a length of 9μm with 450 nm gap separation between channels [see Fig. 3.10(b)]. For a better comparison with the RBRMZI using directional couplers in Fig 3.8(a), we adopt a

radius of 4.05μm to fix the FSR of R1. The field distributions of the MMI coupler lunched from different input channels are shown in Fig. 3.10(c). The light equally splits into the three output channels when the input light is injected from the middle channel [upper panel]. When the input light is launched from one side channel, large amount of intensity is guided into the opposite output channel and the center output channel, aiming to strengthen the interaction between the two rings [lower panel].

The simulated transmission of RBRMZI integrated with MMI coupler is presented in Fig 3.11. Even though the extinction ratio and modulation depth of the CRIT resonance are lower than that of RBRMZI with a directional coupler, the sharp CRIT resonances are still clearly observed since a strong coupling happens. The non-unity transparent peaks and non-zero transmission dips can be explained by two reasons. One reason is the insertion losses between the MMI channels and MMI multimode waveguide result in the light intensity at two MZI arms are not identical, giving rise to the non-complete destructive interferences between the optical pathways. The other reason is the ring-bus coupling in the RBR part is not under critical-coupled condition, thus, the resonant light can still leak into the output port. Compared to the CRIT in Fig. 3.8, there are several fake transparent peaks and the resonance positions have been slightly shifted in Fig. 3.11. We believe this is due to the combination effect as a result of the working mechanism of MMI coupler and the resonant properties of RBR resonator.

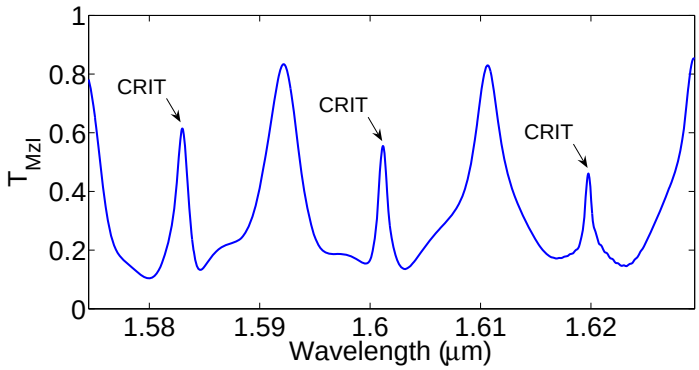

Fig. 3.11. Simulated transmission of RBRMZI integrated with a MMI coupler for three CRIT orders.

3.6 Summary

The RBRMZI structure has been theoretically explored for its capability of generating a narrow EIT-like transparency with high extinction ratio and finesse enhancement. Since the EIT-like spectrum in the RBRMZI is generated by inter-pathway interference between RBR and MZI arms, a low-finesse resonator is required for CRIT, instead of other existing schemes which requires high finesse resonator. Finally, the FDTD simulations are performed to verify the theoretical model and good agreements are obtained. For completeness, the RBRMZI integrated with MMI coupler is proposed for relaxing fabrication requirement. The proposed device can be useful for fast optical switching and sensor application, since they require both high finesse and high ER.

Chapter 4 Temporal Coupled Mode Theory in Ring-Bus-Ring Mach-Zehnder Interferometer

4.1 Introduction

Temporal coupled mode theory (TCMT) is a promising approach to revealing work mechanisms of resonators since it gives analysis to the time-dependent behavior between the incident/transmitted waves and resonant modes using time differential equations [59]. The dynamic equation has been tremendously successful in modeling a wide variety of passive and active optical resonant devices [41, 48, 60, 61]. In these structures, the resonators are typically loaded with one or several incoming/outgoing ports to allow frequency-selective power transfer between the ports. In the case when only a single mode is present in a lossless resonator, the mode coupling between bus and resonator can be described in terms of a unitary *S*-matrix that derived from the standard TCMT [62]. However, when more than one resonant mode is presented, there is a possibility that the optical modes inside the resonator can only be expressed using a non-orthogonal basis function, since the cavity by itself couples to the ports and thus is an open structure [63]. The presence of such non-orthogonality will strongly affect the response of the multimode system. For example, an induced transparency in the transmission spectrum resembling atomic EIT effect can be achieved in a structure with a middle waveguide sandwiched by two side-coupled photonic crystal (PhC) cavities [63]. This transparent feature is applicable for all-optical dynamical storage of light in solid state [41, 48] and high performance modulator [64]. However, in the above examples, most devices are based on the 2×2 coupler, but few on the 3×3 coupler (tri-coupler) [63]. In Chapter 3, the transfer matrix formalism (TMF) was developed to investigate the RBRMZI configuration, as shown in Fig. 4.1, where the resonant modes interact with each other at a tri-coupler, demonstrating the capability of generating EIT-like (CRIT) transparent spectrum in such a device.

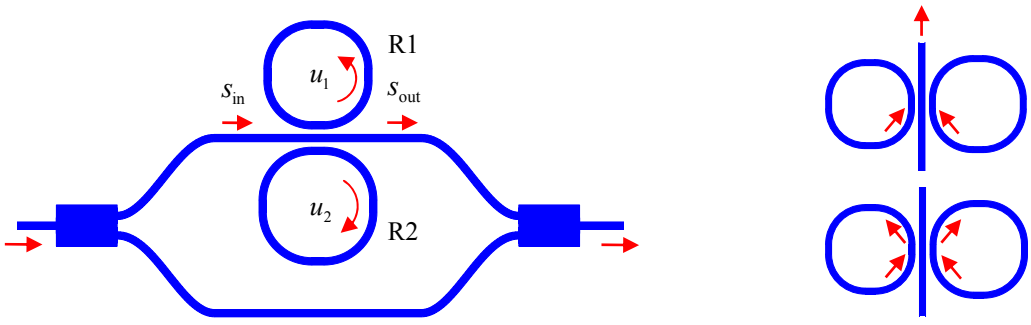

Fig. 4.1. Left: schematic of RBRMZI. Right: two characteristics of mode coupling inside RBR part.

In this chapter, we further our investigation by applying TCMT to illustrate the transparency property of the RBRMZI intuitively. The upper MZI arm in Fig. 4.1 depicts the schematic of the RBR structure, which consists of two rings, ring1 (R1) and ring2 (R2) with single mode u_1 and u_2 respectively, indirectly coupled through a middle bus waveguide between each other. Due to the presence of a tri-coupler at the

coupling region, the mode decay inside the RBR structure is qualitatively different compared to other existing resonators based on a 2×2 coupler. As illustrated in the right side of Fig. 4.1, the RBR has two main differences: two resonant modes (u_1 and u_2) decay to the middle bus simultaneously (upper figure) and the ring-bus coupling can induce an indirect coupling between the two outer rings through the bus (lower figure). This chapter is started by applying the coupling of mode analysis to the simplest single-ring case to highlight the essence of TCMT. We then exploit the fact that the energy of the system is conserved to find the coupling matrix of the tri-coupler. After that, the obtained matrix is used to explain the essential properties of the CRIT spectrum through integration of RBR with MZI. Unlike the TMF method which requires complex derivation, the TCMT is extraordinarily simple and illustrative since it demonstrates the transparency mimicking an EIT expression. Finally, a good agreement is obtained between the three methods, TCMT, TMF and FDTD simulation results.

4.1 One-ring-one-bus

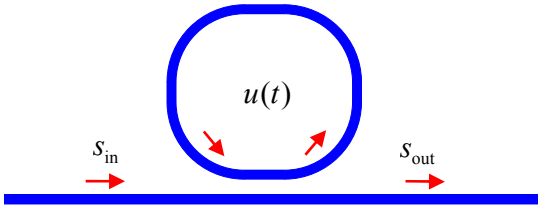

Fig. 4.2. Configuration of 1R1B with one single-mode transmitted inside it.

The single-ring resonator evanescently side-coupled to one input bus waveguide (1R1B in short) is shown in Fig. 4.2. It can be seen that the incident light going from the input port (s_{in}) couples into the ring resonator and excites the resonant mode $u(t)$, then transfers into the output port (s_{out}). The dynamic energy flow equations connecting s_{in}, s_{out} and $u(t)$ in 1R1B can be modeled as,

$$\begin{aligned} du/dt &= i\omega_i u - (1/\tau_i + 1/\tau)u + i\eta s_{in} \\ s_{out} &= s_{in} + i\eta u \end{aligned} \tag{4.1}$$

where the first equation describes the evolution of the ring resonator mode in time and ω_i is the resonance frequency, $1/\tau_i$ is the intrinsic decay rate due to ring absorption and $1/\tau$ is the external decay rate of the energy coupled into the bus. The second equation illustrates the connection of the incident and transmitted waves, where η is the coupling coefficient associated with the ring-bus interaction.

The ring-bus coupling coefficient (η) and the decay rate ($1/\tau$) are related by energy-conservation, i.e., the energy for the overall 1R1B, including both ring and bus, is conserved. To see this, we consider a situation where the external incident wave is absent at the initial time (t=0). Then at t>0, the ring supports a traveling wave $u(t)$ with a amplitude of $U(t)$ and the total power flowing through the ring is represented as $|U(t)|^2$ [60]. In the case that there is no absorption inside the ring area ($1/\tau_i$~0), the power of the ring exponentially decays into the bus determined by $|u|^2=|U(t)|^2\exp(-2t/\tau)$. When we consider the bus as a receiver, the traveling mode in the ring evanescently couples into the bus and engenders the transmitted

wave (s_{out}). Thus, we have $d|u|^2/dt=-2|u|^2/\tau=-\eta^2|u|^2$ and obtain the relation of $2/\tau=\eta^2$. Through solving Eq. (4.1) with this relation and $s_{in}\sim\exp(i\omega t)$, the normalized transmission of the 1R1B is given by,

$$t_{1R1B}=\frac{s_{out}}{s_{in}}=\frac{i(\omega-\omega_i)+\tau_i^{-1}-\tau^{-1}}{i(\omega-\omega_i)+\tau_i^{-1}+\tau^{-1}} \tag{4.2}$$

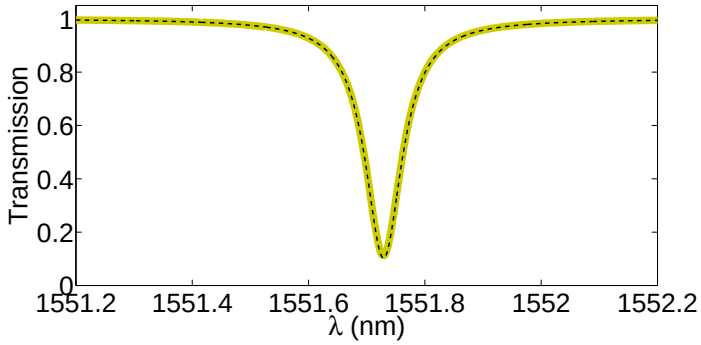

Fig. 4.3. Comparison of transmissions calculated from TMF (thick-faded) and TCMT (dashed). L_c=2μm, r_0=0.99, $v_g=c/4.25$ and a=0.995 are used.

We can see that Eq. (4.2) describes the transmission of the 1R1B device using the intrinsic loss and decay rate in temporal domain. Conceptually, it should be consistent with the transmission obtained from Eq. (2.13) using TMF method. In fact, the two methods are related by two considerations: the energy conservation and Q-factor. In order to find out this consistency, we first consider the energy conservation to get the relation between the coupling coefficients. The total stored energy $|u(t)|^2$ and the entire power flowing through any cross section of the ring waveguide $|U(t)|^2$ can be related by $|u(t)|^2=|U(t)|^2t_R$, where t_R is the cavity round-trip time given by $t_R=L/v_g$. L and v_g are the ring circumference and group velocity of the traveling wave in the resonator, respectively. Therefore, the reduction of the total stored energy in per round-trip time should be equal to the increase of the transmitted wave s_{out} originated from the decaying of the traveling wave with amplitude $U(t)$. Then, mathematically, we can obtain the relationship of the coupling coefficients in time and in space as follows,

$$\left|s_{out}\right|^2=\eta^2\left|U(t)\right|^2=t_0^{\,2}\frac{v_g}{L}\left|u(t)\right|^2\rightarrow\eta^2=t_0^{\,2}\frac{v_g}{L}=(1-r_0^{\,2})\frac{v_g}{L} \tag{4.3}$$

where t_0 and r_0 are the cross coupling coefficient and reflection coefficient in TMF, respectively. On the other hand, using the definition of Q-factor in Eq. (2.19), the total Q-factor (Q_t) is obtained by solving the full-width at half-maximum (FWHM) linewidth of resonance frequency ($\omega_{FWHM}=2/\tau_i+t_0^2$) from Eq. (4.2) as $Q_t^{-1}=\omega_{FWHM}/\omega_i=Q_i^{-1}+Q_e^{-1}=\lambda_{FWHM}/\lambda_i$. $Q_i=(\tau_{i1,2}\omega_{1,2})/2$ is the intrinsic quality factor accounting for the ring absorption and $Q_e=(L_{1,2}\omega_{1,2})/(t_0^2v_g)$ is the external quality factor that is responsible for the ring-bus coupling. The notation λ_{FWHM} is the FWHM and λ_i is the resonance wavelength. Then by applying in the result in Eq. (4.3) and $Q_t=Q_i^{-1}+Q_e^{-1}$, all the parameters in Eq. (4.2) can be rewritten via the parameters of TMF (e.g. r_0, a and δ). Fig. 4.3 presents the comparison of the transmissions obtained from Eq. (4.2) and TMF from Eq. (2.13). It shows that the two approaches agree very well each other.

4.2 Ring-bus-ring

In this section, we develop the mode analysis of RBR configuration loaded on the upper MZI arm in Fig. 4.1. Due to the presence of the tri-coupler at the coupling region, the incident light couples into the two rings simultaneously, Eq. (4.1) without modification cannot be adopted to model the mode coupling in the RBR case. In addition, the indirect coupling between the two outer rings that induced by the ring-bus coupling must be taken into account. To do this, we recall the general TCMT for a resonant system with the existence of more than one resonant modes [62],

$$\begin{aligned} du/dt &= (i\Omega - \Gamma_i - \Gamma)u + i\mathrm{H}^{\mathrm{T}} s_{\mathrm{in}} \\ s_{\mathrm{out}} &= s_{\mathrm{in}} + i\mathrm{H}u \end{aligned} \tag{4.4}$$

where Ω and Γ_i are 2×2 Hermitian matrices in which the diagonal elements represent the resonance frequencies and intrinsic losses respectively. Γ is a Hermitian matrix describing the decay rates of two resonant modes of the two rings with respect to the middle bus. H is a matrix whose elements are the ring-bus coupling coefficients. The expressions of u, Ω, Γ_i, H and Γ are given by,

$$u = \begin{bmatrix} u_1 \\ u_2 \end{bmatrix}, \Omega = \begin{bmatrix} \omega_1 & 0 \\ 0 & \omega_2 \end{bmatrix}, \Gamma_i = \begin{bmatrix} {\tau_{i1}}^{-1} & 0 \\ 0 & {\tau_{i2}}^{-1} \end{bmatrix}, \mathrm{H} = \begin{bmatrix} \eta_1 \\ \eta_2 \end{bmatrix}^{\mathrm{T}}, \Gamma = \frac{1}{2}\begin{bmatrix} {\eta_1}^2 & \eta_1\eta_2 \\ \eta_1\eta_2 & {\eta_2}^2 \end{bmatrix} \tag{4.5}$$

where the parameters with subscripts 1 and 2 correspond to the rings R1 and R2, respectively. The formula of decay rate matrix Γ is obtained in the following way: the overall RBR system is energy conserving. Following the similar procedure in 1R1B that the power in the transmitted wave comes from the traveling mode, we have $d(u^*u)/dt = u^*(-i\Omega^* - \Gamma^*)u + u^*(i\Omega - \Gamma)u = -2u^*\Gamma u = -s_{\mathrm{out}}{}^* s_{\mathrm{out}} = -u^*\mathrm{H}^*\mathrm{H}u$. Thus, Γ can be expressed in terms of H as $\Gamma = \mathrm{H}^*\mathrm{H}/2$. In the expression of Γ, the diagonal elements ${\eta_{1,2}}^2/2$ are the decay rates of the corresponding resonant mode $u_{1,2}$ to the middle bus. The non-zero elements $\eta_1\eta_2/2$ are the indirect coupling between the two outer rings induced by the direct ring-bus coupling. Therefore, the two resonant modes form a non-orthognal basis, since $\Gamma\Omega \neq \Omega\Gamma$ [63].

We arrive at the following set of equations by substituting Eq. (4.5) into Eq. (4.4),

$$\begin{aligned} du_1/dt &= (i\omega_1 - {\tau_{i1}}^{-1} - {\eta_1}^2/2)u_1 - \eta_1\eta_2 u_2/2 + i\eta_1 s_{\mathrm{in}} \\ du_2/dt &= (i\omega_2 - {\tau_{i2}}^{-1} - {\eta_2}^2/2)u_2 - \eta_1\eta_2 u_1/2 + i\eta_2 s_{\mathrm{in}} \\ s_{\mathrm{out}} &= s_{\mathrm{in}} + i\eta_1 u_1 + i\eta_2 u_2 \end{aligned} \tag{4.6}$$

Similar to the TMF, the differential equations look like that of 1R1B in Eq. (4.1), but they are now modified due to the contribution of the resonant process of u_1 (${\eta_1}^2/2$), u_2 (${\eta_2}^2/2$) and the mixture of the two resonant modes ($\eta_1\eta_2/2$). This is also different from the two mutually coupled resonators system [refer to Eq. (B1) in Appendix B], where the ring-bus direct coupling is only accessible for one of the rings (ring1). Whereas the interaction between excited mode u_2 in ring2 and the propagating waves (s_{in} and s_{out}) in the bus waveguide is relied on the loading factor term ($\eta_c u_2$) imposed by mode u_2 on mode u_1. However, in the RBR, the light interaction works in the tri-coupler section formed by a ring-bus-ring interface. Within

conventional 2×2 couplers, it is impossible to obtain mixture interaction between the two cavities without mutual coupling between them, e.g. in the two cascaded 1R2B configuration [refer to Eq. (B5)]. Solving the differential equations in Eq. (4.6) with the time dependency of s_{in}~exp($i\omega t$), we can get the relative buildup B_{21} which is defined as the ratio of the light circulation in R2 relative to that of R1,

$$B_{21}=\left|\frac{-\eta_2\Delta\omega_1+i\eta_2\tau_{i1}^{-1}}{-\eta_1\Delta\omega_2+i\eta_1\tau_{i2}^{-1}}\right|^2 \xrightarrow{\tau_{i1}^{-1},\tau_{i2}^{-1}\sim 0}\left(\frac{\eta_2}{\eta_1}\right)^2\left|\frac{\Delta\omega_1}{\Delta\omega_2}\right|^2 \tag{4.7}$$

which represents the light intensity distribution in the two rings. It is quite clear that the light relative buildup is proportional to coupling strengths $\eta_{1,2}$ and inversely proportional to the cavity size detuning (or frequency detuning $\Delta\omega_{1,2}=\omega-\omega_{1,2}$). The normalized transmission ($t=s_{out}/s_{in}$) of RBR system is obtained by solving Eq. (4.6) with Eq. (4.7),

$$t_{RBR}=\frac{s_{out}}{s_{in}}=\frac{(i\Delta\omega_1+\tau_{i1}^{-1}-\eta_1^2/2)(i\Delta\omega_2+\tau_{i2}^{-1}-\eta_2^2/2)-\eta_1^2\eta_2^2/4}{(i\Delta\omega_1+\tau_{i1}^{-1}+\eta_1^2/2)(i\Delta\omega_2+\tau_{i2}^{-1}+\eta_2^2/2)-\eta_1^2\eta_2^2/4} \tag{4.8}$$

When the resonance frequencies of the two rings coincide $\Delta\omega_1=\Delta\omega_2$ (one special case is the two rings are identical) and the losses are the same $1/\tau_{i1}=1/\tau_{i2}=1/\tau_i$, the transmission can be simplified to,

$$t_{RBR}=\frac{i\Delta\omega_1+\tau_i^{-1}-(\eta_1^2+\eta_2^2)/2}{i\Delta\omega_1+\tau_i^{-1}+(\eta_1^2+\eta_2^2)/2} \tag{4.9}$$

which again looks very similar to the transmission of 1R1B in Eq. (4.2), except the different coupling strength terms $(\eta_1^2+\eta_2^2)/2$ and τ^{-1}. In fact, the two equations are equivalent with each other, as verified by the transmission response of RBR later. Following the similar procedure in single-ring resonator, R1,2 are assumed to support traveling wave $u_{1,2}(t)$ with a amplitude of $U_{1,2}(t)$. Considering the energy conservation in the overall RBR system, we arrive at $|s_{out}|^2=t_1^2|U_1(t)|^2+t_2^2|U_2(t)|^2=\eta_1^2|u_1(t)|^2+\eta_2^2|u_2(t)|^2$, where $t_{1,2}$ are the cross-coupling coefficients of the two rings and the middle bus waveguide in TMF. Between $t_{1,2}$ and r_0 (the reflection coefficient of the middle bus), there exists a relation of $r_0^2+t_1^2+t_2^2=1$ [refer to Eq. (A8)]. Recombining the above relation with Eq. (4.3), we can yield the relationship between the temporal and spatial coupling coefficients,

$$\begin{aligned}&\eta_{eff}^2=\eta_1^2+\eta_2^2=t_1^2v_gL_1^{-1}+t_2^2v_gL_2^{-1}\\&\xrightarrow{L_1=L_2}=(t_1^2+t_2^2)v_gL_1^{-1}=(1-r_0^2)v_gL_1^{-1}\end{aligned} \tag{4.10}$$

where η_{eff} is the effective coupling coefficient for the tri-coupler, which represents the total power coupled to the bus from the resonant modes. The second row in Eq. (4.10) implies that, when the two rings have the same resonances with an identical cavity circumference, the bus in RBR and 1R1B will receive a same fraction of power from the resonant ring(s), making the two equations, Eq. (4.3) and Eq. (4.10), be equivalent. This explains why the RBR behaves like a 1R1B when the two rings are identical.

To verify the theoretical analyses, Fig. 4.4 presents the comparison of transmissions calculated from the FDTD simulation, TMF and TCMT for one resonance order. Excellent agreement is obtained between

the three approaches. We can see only one resonance dip when $\omega_1=\omega_2$ and two distinguished resonances when $\omega_1\neq\omega_2$. Note that there is no resonance splitting at $\omega_1=\omega_2$, which is unlike other two-cavity systems. The existence of resonance splitting completely depends on the additional phase shift that introduced into resonant mode u_1 by the presence of the second ring (R2). As mentioned in Chapter 3, there is no difference whether the resonant light passes through two rings in RBR or one ring in 1R1B, owning to the 2π phase shift from four-time cross-couplings. Whereas, for the two mutually coupled rings structure [40], it naturally has the resonance splitting, since R2 introduces a π phase shift due to twice cross-couplings between two rings. This π phase difference gives rise to a destructive interference between the two ring resonant modes in the output port [refer to Eq. (B3)]. In the two-cascaded 1R2B configuration, the power exchange between the cavities are facilitated by double parallel buses, thus, the existence of resonance splitting is dependent on the ring-to-ring separation [see Eq. (B6)]. The resonance splitting only occurs when the coupling phase (ϕ) between the two rings is not an integral number of π ($\phi\neq m\pi$). In other situations, when $\phi=m\pi$, the additional phase (4π) caused by R2 is a combination of three parts, π from twice cross-couplings between R1 and R2, π from half circumference of R2, and 2π from coupled buses. Such a 4π phase results in a constructive interference and thus the resonance splitting disappears.

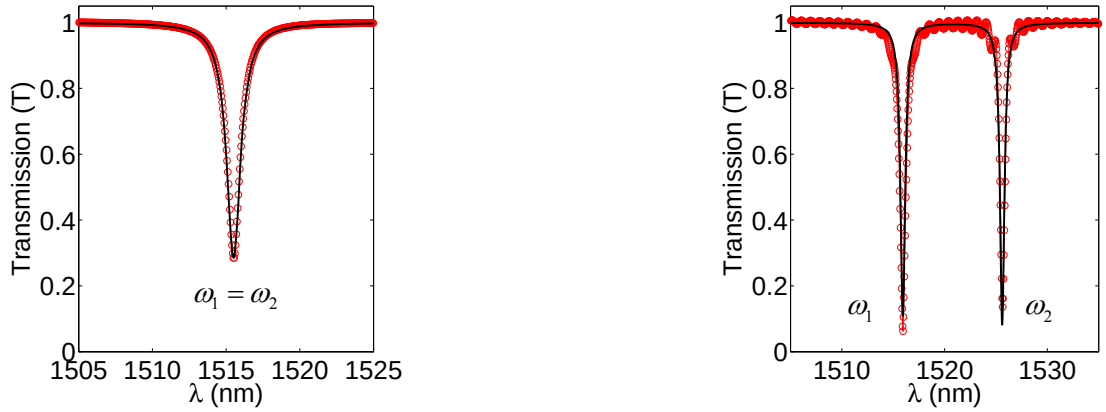

Fig. 4.4. Comparison of RBR transmissions obtained from TCMT and TMF (solid lines) and FDTD simulations (open circles). Note that the profiles of two analytic theories are not distinguishable due to excellent fitting between the two.

The proposed RBR device provides new possibilities for designing various microring resonator-based devices. For instance, it is possible to add drop ports at each ring to redirect the input light through the resonant rings, as shown in Fig. 4.5(a). The power in each output port can be calculated from the modified equations of Eq. (4.6), where the decay rates caused by drop channels should be included. Panel (1)-(3) in Fig. 4.5(b) show how the incident light is transferred at three different wavelengths. The RBR filter is flexible and relatively more compact compared to other cascaded ring filters since it can drop light to left and right simultaneously using one coupler. As highlighted earlier in Eq. (4.7), how much light located in the rings relies on the ring-bus coupling strengths and frequency detuning. This property suggests another potential application of the RBR device as a selective power splitter. At the position of coincident

resonance, RBR can behave like a 1×3 power splitter with arbitrary fraction of input intensity through varying the coupling strengths of the tri-coupler. One special case is under the critical-coupled condition, the transmission is zero and thus the RBR functions as a 1×2 splitter. When the coupling in the tri-coupler is symmetric, it gives 50% to 50% splitting, as shown in panel (4).

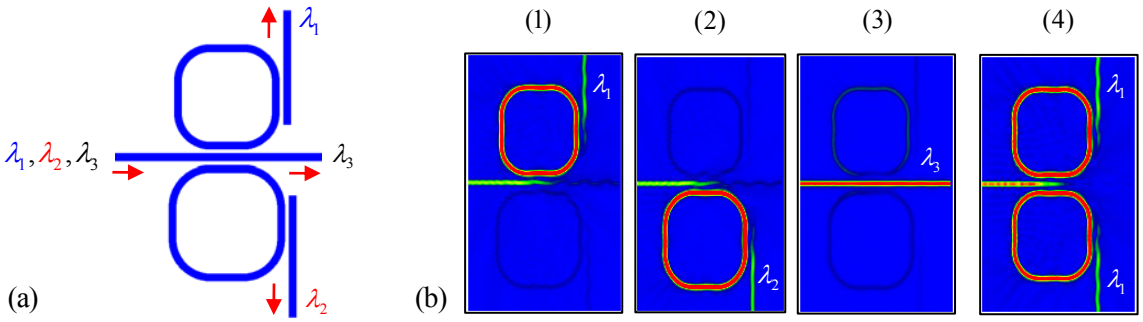

Fig. 4.5. (a) Schematic of proposed RBR channel dropping filter. (b) Panel (1)-(3) show the dominated light at three wavelengths. Panel (4) shows the intensity distribution of a 1×2 RBR power splitter.

4.4 Ring-bus-ring Mach-Zehnder interferometer

For simplicity, we consider a balanced MZI with two perfect 3dB splitter/combiner at the input/output end, the transmission of the MZI enhanced with RBR is modeled by $t_{MZI}=i(t_{RBR}+1)/2$,

$$t_{MZI}=\frac{i(i\Delta\omega_1+\tau_{i1}^{-1})(i\Delta\omega_2+\tau_{i2}^{-1})}{(i\Delta\omega_1+\tau_{i1}^{-1}+\eta_1^2/2)(i\Delta\omega_2+\tau_{i2}^{-1}+\eta_2^2/2)-\eta_1^2\eta_2^2/4} \tag{4.11}$$

The general shapes of Eq. (4.11) are plotted in Fig. 4.6 for two different situations. The RBRMZI transmission exhibits an atomic EIT-like (or CRIT) feature that a narrow transparent peak occurs in the center of a broader transmission background. The occurrence of the CRIT resonance can be analyzed in the following procedures. For better analysis, we assume that the tri-coupler has a symmetric coupling ($\eta_1=\eta_2$) and the intrinsic losses in the two rings are identical ($1/\tau_{i1}=1/\tau_{i2}=1/\tau_i$). When a strong coupling occurs, i.e., $\eta_1^2/2 \gg |\omega_1-\omega_2| \gg 1/\tau_i$, there are two minima and a maximum at the positions of $\omega=\omega_{1,2}$ and $\omega=(\omega_1+\omega_2)/2$ in the transmission spectrum respectively,

$$T_{min}\equiv|t_{MZI}|^2\approx\frac{4\tau_i^{-2}}{\eta_1^4},\qquad T_{max}\approx\frac{[(\omega_2-\omega_1)/2]^4}{[\eta_1^2\tau_i^{-1}-(\omega_2-\omega_1)^2/4]^2}. \tag{4.12}$$

When the resonance detuning $\Delta\omega_{1,2}$ are much less than the resonator's free spectral range (FSR), i.e., $\Delta\omega_{1,2}\ll 2\pi v_g/L_{1,2}$, the transmission power of Eq. (4.11) in a lossless case ($1/\tau_{i1,2}\sim 0$) can be deduced as,

$$T_{MZI}=1-\frac{(2\eta_1^2)(2\eta_1^2)(\Delta\bar{\omega})^2}{(2\eta_1^2)^2(\Delta\bar{\omega})^2+4\left[(\Delta\bar{\omega})^2-(\omega_2-\omega_1)^2/4\right]^2} \tag{4.13}$$

where $\Delta\bar{\omega}=\omega-(\omega_1+\omega_2)/2$. We recall the EIT absorption expression (T_{abs}) in atomic system from reference [65] as $T_{abs}=\Omega_1^2\Gamma\Delta^2/[\Delta^2\Gamma^2+4(\Delta^2-\Omega_2^2/4)^2]$, where Ω_1 and Ω_2 are respective Rabi frequencies of the probe

field and pump field, respectively. Γ is decay rate and Δ is detuning of the probe field from the atomic resonance. It can be seen that the fraction in Eq. (4.13) mimics the behavior of EIT equation if we regard ω_2-ω_1~Ω_2, $\Delta\bar{\omega}$ ~Δ and $2\eta_1^2$~Ω_1. From this analogy, we can see that no drive power is needed to generate transparency in ring resonator system. The function of powerful drive laser (Ω_1) used to create EIT in atomic vapor is realized by the interaction between the two rings ($2\eta_1^2$). It is worth noting that the bandwidth of the transparent resonance (Π) is arbitrarily narrow in low loss case,

$$\Pi \approx \frac{(\omega_2-\omega_1)^2+4\tau_i^{-2}}{2\eta_1^2+(\omega_2-\omega_1)} \tag{4.14}$$

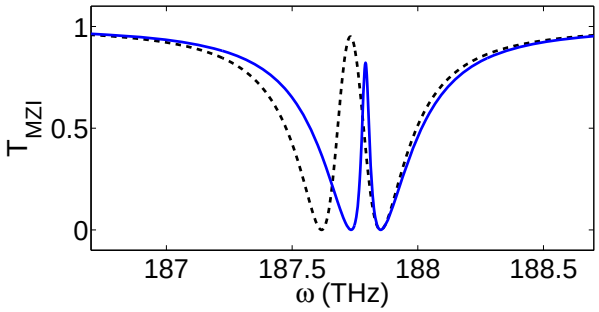

Fig. 4.6. Transmissions of RBRMZI system under two conditions. Solid curve is for ω_2-ω_1=1.2GHz and dashed curve is for ω_2-ω_1=2.4GHz, where Q_i/Q_e≈50 is used.

Eq. (4.14) clearly tells us that the transparency becomes sharper with increasing coupling strength η_1. This can be explained by the presence of non-orthogonal modes in RBR device, which renders a strong interaction between two cavities. The arbitrary position of the transparent resonance ω=(ω_1+ω_2)/2 with a tunable bandwidth Π has several important applications. For instance, the RBRMZI device can serve as tunable source of slow light since the group delay (T_g) that originated from the transparency is approximately $T_g \approx \Pi^{-1}$ [41]. This resonator's compound delay line has certain advantages over the slow light technique in classical systems. For example, the resonator's delay time is strongly dependent on the detuning of frequency separation |ω_2-ω_1|. The detuning have been examined experimentally using pump-probe scheme [46] and electro-optic effect [64] on silicon platform. Furthermore, the transparent position of the CRIT in ring resonators could be arbitrarily controlled to satisfy different resonance frequencies, whereas the atomic EIT signal is limited only to a small number of accessible transition frequencies. This advantage especially highlights the application of microring resonators for all-optical communication and signal processing. In addition, the resonator systems have much lower loss compared to that in real atomic systems. In the atomic systems, since the spontaneous emission is not fully suppressed, a significant amount of input light is absorbed [41]. Another application of CRIT is for low-power switching realized in all-pass ring resonator, as presented in Fig 4.6, where the transparency is shifted from the dashed curve to the solid curve. The perturbation theory calculation [61] shows that a slightly variation in the group index of the larger ring (Δn_g~0.001) can obtain 100% switching of the transparent frequency due to the Vernier effect of the two ring resonances.

Finally, we present that the theoretical prediction is in good agreement with simulation results from 2D-FDTD method. The MMI with a width of 2.4μm and a length of 5μm is adopted to connect MZI arms. We use a circumference ratio of the two rings as γ=1.05, a radius of 5μm and a coupling length of 4μm. Fig. 4.7 shows the FDTD calculation results of the RBRMZI, which is fitted using the TMCT described earlier and the TMF in Eq. (3.3). In the curve fitting, γ=1.0498, r_0=0.575 and the loss factor a=0.995 are used. Generally, the analytical formulas agree well with the simulation results, except some non-idealities that are not taken into account in our TMCT model. For example, the small shift of transparent peak (~5GHz) caused by the asymmetricity in the simulation result originates from phase bias (ϕ_B) between two MZI arms [refer to Eq. (3.9)] and wavelength dispersion [36]. We also note that the different contrasts in the fitted curves are attributed to the occurrence of a rather strong coupling (r_0=0.575). Such difference can be reduced with weak coupling through optimizing RBR parameters.

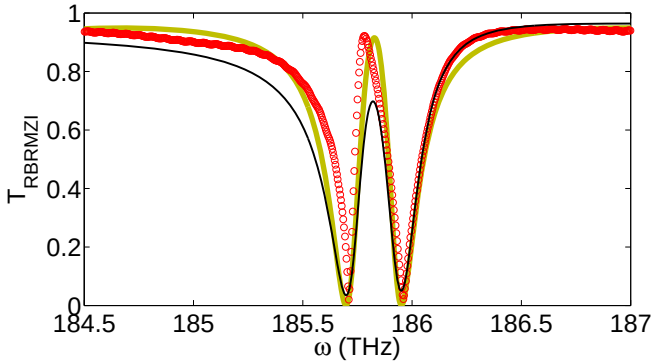

Fig. 4.7. Comparison of transmissions obtained from FDTD simulation (open circles), TCMT (solid) and TMF (thick-faded) for balanced arm length RBRMZI.

We have mentioned the CRIT property can also be created in the relatively similar configurations with two PhC cavities in PhC system or two detuned aperture-side-coupled FP cavities in plasmonic system instead of rings [63], as shown in Fig. 4.8(a) and Fig. 4.8(b), respectively. We believe that the mode analysis of the tri-coupler in RBRMZI is also helpful for analyzing the induced transparency in the two similar devices. Take the PhC system for example, this structure consists of a center PhC waveguide sandwiched by two side-coupled PhC cavities with different dielectric constants. The difference in dielectric constants gives the two cavities different resonance frequencies, which are corresponding to the two resonance dips in EIT-like spectrum. However, in general, the RBR structure exhibits two individual resonances when the two resonances do not coincidence with each other. It is thus interesting to see the transmission response of such a PhC system. Considering the standing wave in PhC resonator with modified Eq. (4.6), the forward transmission (s_+/s_{in}) can be obtained as,

$$\frac{s_+}{s_{in}} = \frac{(i\Delta\omega_1 + \tau_{i1}^{-1})(i\Delta\omega_2 + \tau_{i2}^{-1})}{(i\Delta\omega_1 + \tau_{i1}^{-1} + \eta_1^2)(i\Delta\omega_2 + \tau_{i2}^{-1} + \eta_2^2) - \eta_1^2\eta_2^2} \tag{4.15}$$

where all parameters have the same physics as those in Eq. (4.11). Compared to Eq. (4.11), Eq. (4.15) has the remarkable similar expression except the modified decay rate terms ($\eta_{1,2}^2/2$). This difference comes

from the different work mechanisms of the two kinds of resonators, i.e. standing wave in PhC cavity and traveling wave in ring resonator. Therefore, in PhC cavity, the resonant modes decay in both forward and backward directions, rendering in the decay rate for the transmitted wave is divided by a factor of two. The EIT-like spectrum described by Eq. (4.15) can also be explained by the bi-directional transmissions in PhC cavities. When the two resonance modes in the PhC cavities decay equally to the two output ports, such a PhC system will possess only a single independent decay port, which gives rise to the all-optical induced transparency analog of atomic EIT [63].

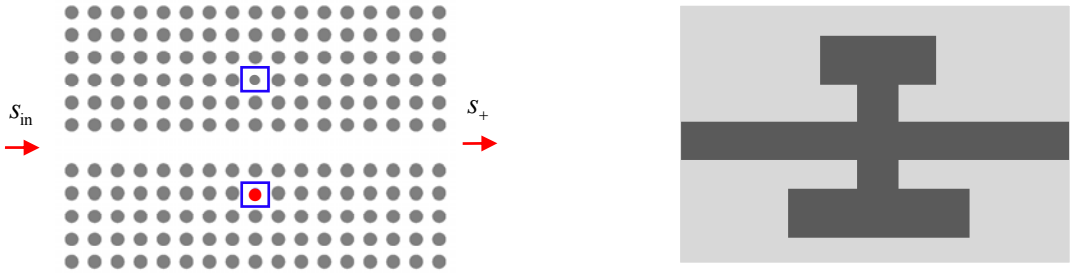

Fig. 4.8. Schematics of two similar configurations. (a) PhC system with two side-coupled cavities. The boxes indicate the positions of the two cavities with different dielectric constants. (b) Plasmonic structure with two aperture-side-coupled FP resonators.

4.5 Summary

The TCMT is originally developed for the RBR structure and used to analyze the CRIT in RBRMZI configuration. Due to the presence of a tri-coupler at the coupler region, the mode decay in the RBR is different compared with other traditional resonators based on a 2×2 coupler. The TCMT shows that an arbitrary narrow transparent resonance can be tuned by coupling coefficients and frequencies spacing, which is applicable for low-power switching and tunable delay line. The two theories, TCMT and the TMF, are related via energy-conservation and Q-factor. A good agreement is achieved between TCMT, TMF and the 2D-FDTD numerical calculations.

Chapter 5 Experimental Realization of Coupled Resonator Induced Transparency

5.1 Introduction

Silicon-on-insulator (SOI) technology offers tremendous potential benefits for realizing ultra-compact integrated optics, owning to its compatibility with CMOS fabrication procedure for building large-scale on-chip optical devices. The high-index contrast SOI waveguide shows a strong confinement of guided modes, which allows building high-density photonic circuits with small radius and low bending loss on silicon substrates [32]. The CRIT based on resonant cavities has been experimentally demonstrated in SOI technology [45], however, in practice, it is still difficult to detune the resonant interaction between the internal pathways in optical systems. The transparent spectrum with narrow linewidth in current existing configurations can only be obtained under very stringent fabrication conditions. In the cascaded 1R2B system [45], for example, the required resonator circumference difference between two rings is only ~8nm, which is clearly difficult to control in fabrication. In other configurations based on mutually coupled microspheres [44, 50] and microrings [40, 47, 50], the two almost identical resonators are required to have infinitesimally different intrinsic cavity losses and coupling strengths. This stringent requirement means that it needs to actively tune the cavity loss or gain, which clearly will impose additional complexity in device designs and fabrication. In Chapters 3 and 4, it has been theoretically proposed that the RBRMZI is capable of generating narrow CRIT resonance by means of synergistic integration of ring-bus-ring geometry with the Mach-Zehnder interferometer.

In this chapter, we present the experimental realization of the CRIT in RBRMZI fabricated on SOI under ePIXfab silicon photonics platform [67]. Different from other systems, a high-Q transparency is achieved by the RBRMZI with two rings having the same intrinsic loss and a relatively large perimeter difference of 2.2μm. This chapter begins by extracting the basic parameters from the measurements of 1R2B and MMI. Then we move on to the characterization of the RBR and RBRMZI, and show a good agreement between the measured results and the theory.

5.2 Experimental setup

Fig. 5.1 illustrates the fiber-to-grating mechanism (a) and the schematic of the measurement setup (b). The coupling between the standard single-mode optical fibers and strip waveguides is facilitated by a focusing grating coupler fabricated on the input/output ports within a footprint of 18.5μm×28μm. The fiber is near vertically butt-coupled to the grating (~10^{o} off the vertical axis) with a coupling efficiency of ~30% [68]. The fiber-to-waveguide coupling efficiency has a Gaussian spectral profile with a bandwidth of ~30nm. As we will see later, this bandwidth is broad enough to characterize microring resonator since the free spectral rang (FSR) is normally less than 30nm for the resonator with a radius of 5μm. The device under test (DUT) is excited with an ASE broadband source with wavelengths ranging from 1520nm to

1610nm. The output power passes through a 90:10 power splitter, where 10% fractional power is guided to a fiber power meter for alignment purpose while all the rest is forwarded to an optical spectrum analyzer for normalization with the input spectrum.

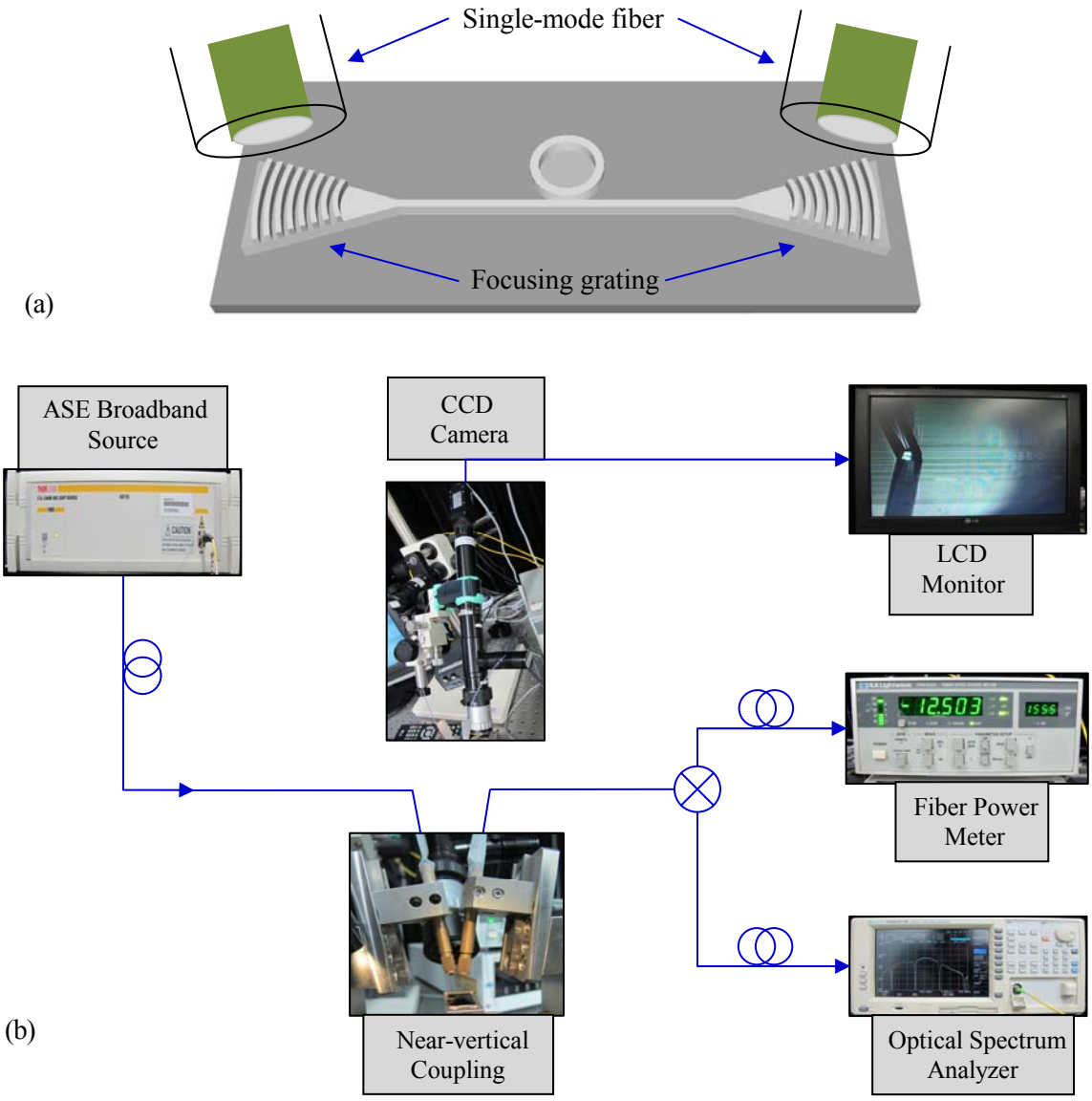

Fig. 5.1 (a) Illustration of the near-vertical coupling with focusing gratings in the measurement. (b) Schematic of the measurement setup for ring resonator devices.

5.3 Characterization of basic parameters

5.3.1 One-ring-two-bus

One of the fabricated 1R2B devices using the directional racetrack coupler is shown in Fig. 5.2. All 1R2B DUTs have a fixed radius of R=5μm and a coupling gap separation (g) varied orderly as 200nm, 300nm and 400nm. For each group of devices with the same coupler gap, the coupling length (L_c) is changed progressively by 2μm increment from 6μm to 14μm. Therefore, in this way, we could estimate and plot the coupling coefficient (r) value as a function of L_c.

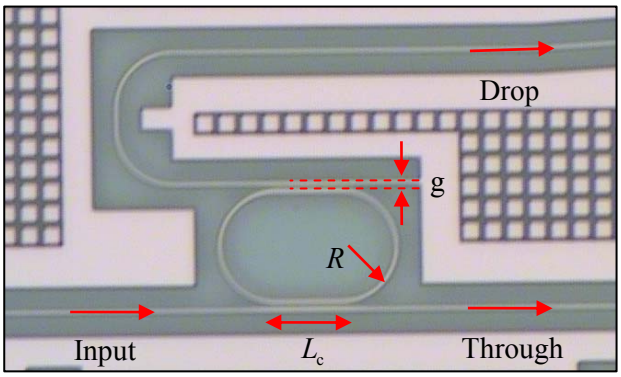

Fig. 5.2. Fabricated 1R2B device with R=5μm and g=300nm.

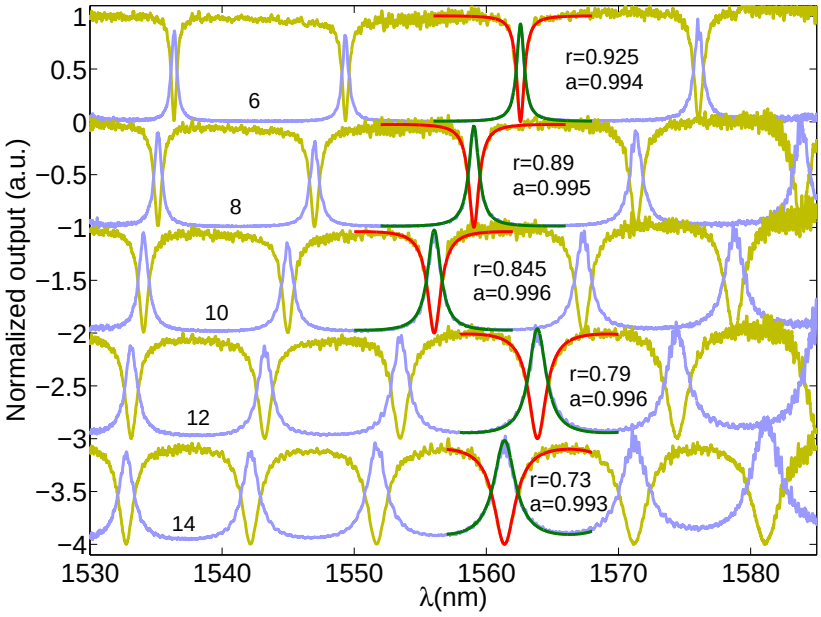

Fig. 5.3. Measured through and drop output of resist coated 1R2B devices with g=300nm, where the coupling length varies from 6μm to 14μm. The fitting focuses on one resonance.

Fig. 5.3 shows the fitted through and drop transmissions for various 1R2B with a gap separation of 300nm and a coupling length ranging from 6μm to 14μm. The theoretical model agrees well with the measurement results within one resonance order. The curve-fitting guideline is described as follows: (1) the ring circumference $L=2(\pi R+L_c)$ is used to convert the normalized detuning $\delta=2\pi n_g L/\lambda$ and relate the coupling length L_c to wavelength domain. The initial estimation of group index n_g is taken from FSR as $n_g=\lambda^2/\Delta\lambda_{FSR}L$ that calculated from the differentiation of resonance situation $n_gL=m\lambda$. The obtained group index is n_g~4.21 (~4.64) for resist coated DUTs (bare silicon DUTs). (2) For 1R2B, the resonance peaks in the drop spectrum is much more sensitive to the effect of loss than the resonance dips in the through spectrum. We can assume an empirical value for loss factor (a) based on reference [36], e.g., a=0.995 (a=1 in lossless case), and obtain the initial estimation of coupling coefficient r by fitting the through transmission near the resonances ($\delta\sim m2\pi$). (3) The obtained r is then applied into the resonance peaks of the drop transmission to extract the real loss factor. Through repeating the above steps, we finally obtain

the fitted parameters as labeled in Fig. 5.3. It shows that the extracted loss factors remain almost constant as a~0.995 in different 1R2B devices, and this value will be used to characterize the RBR and RBRMZI structures that fabricated on the same chips. As expected, the coupling coefficient r decreases (or coupling strength increases) with the increasing of coupling length. In order to understand the trend of this variation, we recall the expression of r=cos(κz) in Eq. (2.12), and get a linear function of,

$$\cos^{-1}(r) = \kappa z = \left(\frac{\pi}{2L_\pi}\right) L_c + \frac{\pi L_0}{2L_\pi} \tag{5.1}$$

where L_π=π/2κ is the beat length and z=(L_c+L_0) is the total coupling length. L_0 is regarded as an offset that takes into account the coupling occurs at the curve region before/after the directional coupler.

Therefore, we can calculate the coupling strength r for any coupling length L_c using the above linear relation. Fig. 5.4(a) presents two fitted linear regressions of wavelengths around 1540 nm and 1580nm. In general, the linear trend agrees well with the theoretical model in Eq. (5.1). As we can see, due to the wavelength dispersion, the value of r becomes more sensitive to λ as L_c increases from 6μm to 14μm. This dispersion also partly explains why the resonance linewidths of the transmissions in Fig. (5.3) gradually broaden with the increase of wavelength. In the longer wavelength regime, i.e., λ=1580nm, the coupling length relative to λ is smaller and thus the beat length should be shorter. This understanding is supported by the experimental results that the sets of [L_0, L_π] for 1540nm and 1580nm are founded to be [2.45μm, 39.27μm] and [2.24μm, 32.06μm], respectively.

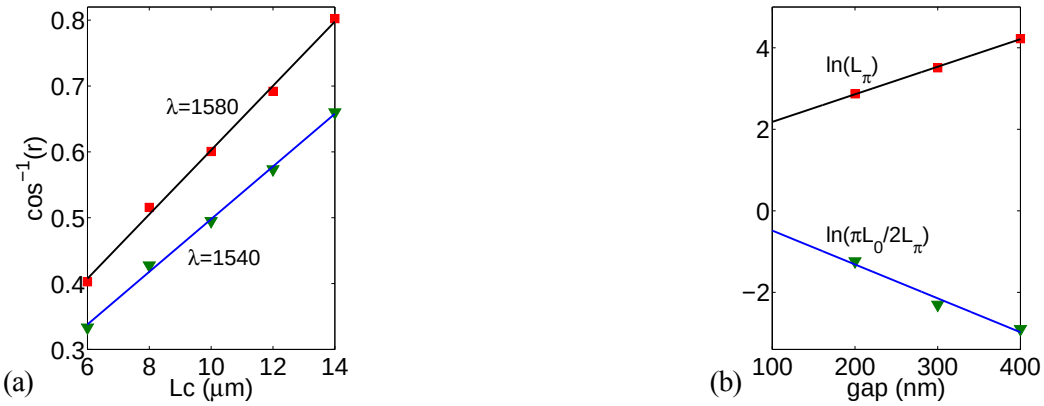

Fig. 5.4. (a) Plot of coupling coefficient r with the variation of coupling length L_c for two wavelengths. (b) Set of [L_0, L_π] as a function of gap at wavelength around λ=1550nm.

Following the above fitting procedure, we can similarly deduce the values of [L_0, L_π] for devices with a gap separation of 200nm and 400nm. Then, it is possible to further extract the initial guess of [L_0, L_π] for devices with any gap separation, as reflected by the linear relation in Fig. 5.4(b). Here we take one special gap separation g=150nm for example. We obtain the set of [L_0, L_π]=[3.22μm, 12.43μm], and deduce r=0.4 in the case of L_c=6μm. The obtained r ($r_{1,2}$ in tri-coupler) will be used later to figure out the coupling coefficient for the center waveguide (r_0=2r-1) of the tri-coupler in RBR and RBRMZI.

We should point out that the curve-fitting can only focus on one resonance order (or one FSR) due to the effect of wavelength dispersion. To cover the entire spectrum, the dispersion effect on the coupling coefficient r and group index n_g need to be considered. We investigate the exact values of n_g and r for each resonance position, and obtain r=-2.51λ(μm)+4.62 and n_g=-0.051λ(μm)+4.222, respectively. As shown in Fig. 5.5(a), the r and n_g decrease gradually in the longer wavelength region. Fig. 5.5(b) shows a good fitting is obtained through the whole spectrum for four FSRs from 1530nm to 1585nm.

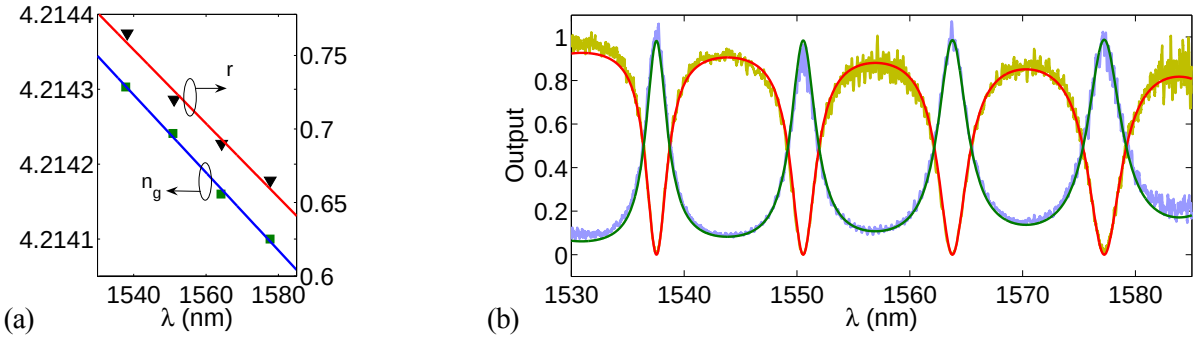

Fig. 5.5. (a) Linear variations of n_g and r as functions of λ. (b) Fitting covers the entire spectra.

5.3.2 Multimode interferometer

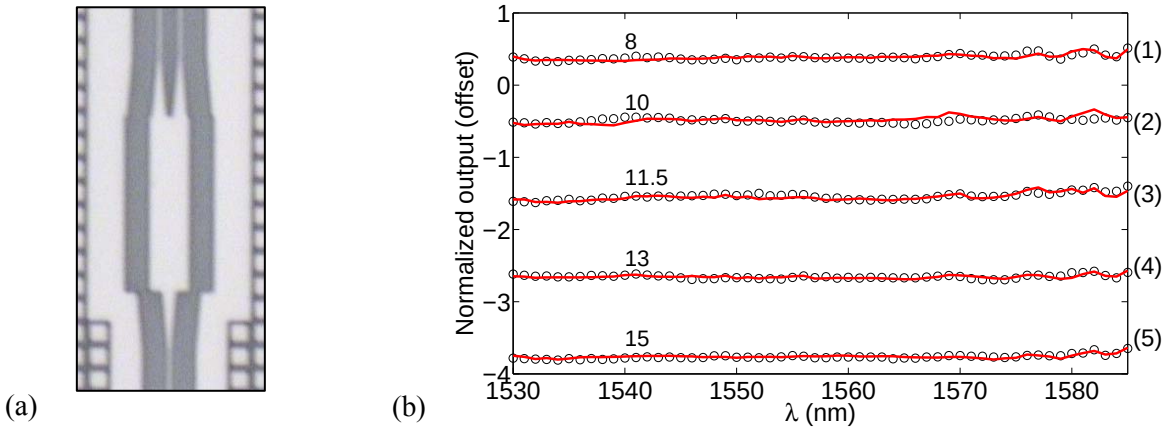

Fig. 5.6. (a) Fabricated 3dB MMI. (b) Measured MMI outputs of various MMI lengths (in μm).

We are going to characterize the 1×2 multimode interferometer (MMI) coupler that will be integrated in RBRMZI. Fig. 5.6(a) shows a single fabricated 3dB MMI coupler with a MMI width (W_{MMI}) of 3.5μm and a MMI length (L_{MMI}) of 11.5μm. The 5μm length waveguides are tapered at the input/output ports to reduce the insertion loss. The measured spectra of five MMIs with different L_{MMI} are shown in Fig. 5.6(b). As we can see, each MMI coupler works very well with the balanced two outputs covering the entire flat spectrum. The ideal MMI device should be DUT2 with a length of L_{MMI}=10μm since both the bar (open circle) and cross (solid line) outputs are around 3dB, which suggests the splitting imbalance and the insertion loss are minimum. However, we have chosen DUT3 into RBRMZI design before the fabrication. In fact, the adoption of DUT3 is acceptable even though the insertion loss seems to be larger than that in

DUT2. Moreover, it has been examined that the waveguide bending loss and propagation loss are much smaller compared to the MMI insertion loss [23]. Thus, in DUT3, only the insertion loss needs to take into account and thus the estimated transmission factor is ~0.88 for one MMI output amplitude.

5.4 Ring-bus-ring Mach-Zehnder interferometer

We first measure the independent RBR device. In the RBR, the first ring (R1) has a radius of R=5μm with a coupling length L_c=6μm. The radius of the second ring (R2) is adjusted by the cavity size detuning γ, which is defined as the ratio between the circumference of R2 and that of R1. This means that the RBR structure is symmetric when γ=1, that is the two rings have the same radius and thus give rise to the identical coupling coefficient (r_1=r_2) with the middle waveguide. For other values of γ, the RBR is asymmetric due to the slight difference in radii and coupling coefficients (r_1≠r_2). Fig. 5.7(a) shows the fabricated RBR device with two identical rings (γ=1). Fig. 5.7(b) presents the measured transmissions of RBR (T_{RBR}) with i-line resist cladding (upper panel) and with air cladding (lower panel), respectively. In the ideal case of γ=1, the RBR should behave like 1R1B and exhibit only one resonance dip during per FSR [refer to Eq. (3.8)]. However, in realistic case, due to the presence of inevitable fabrication non-uniformity, the fitted γ is slightly different from unity as γ=1+Δγ, where Δγ=±0.00033 is the deviation of the designed value γ, as labeled in Fig. 5.7(b). When a strong coupling (r_0=2$r_{1,2}$-1=0.4) occurs at the resist coated RBR, the two separated resonances merge to one indistinguishable resonance due to a strong interaction between the two resonant modes (upper panel). On the other hand, as expected from the theory, we have two resonances when the coupling strength is rather weak (r_0=0.98) (lower panel).

Next, the measurement extends to the RBRMZI device presented in Fig. 5.8. Two 3dB MMI couplers with W_{MMI}=3.5μm and L_{MMI}=11.5μm are integrated to optimize the MZI splitting and combing loss. The 5μm-length tapers are applied to connect input/output ports with the MZI arms to reduce the insertion loss. The RBR component in the upper MZI arm is identical with the independent RBR device, e.g., a fixed L_c=6μm, R1 has R=5μm and the cavity size of R2 is detuned by γ.

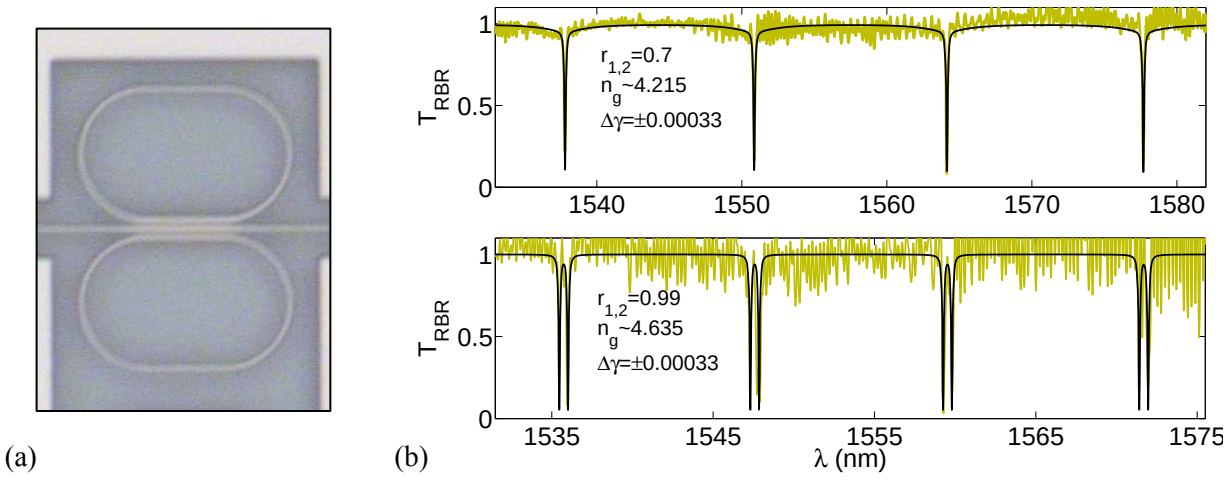

Fig. 5.7. (a) Fabricated RBR with γ=1 and g=250nm in bare silicon. (b) Measured (thick-faded) and fitted spectrum (solid line) of RBR devices.

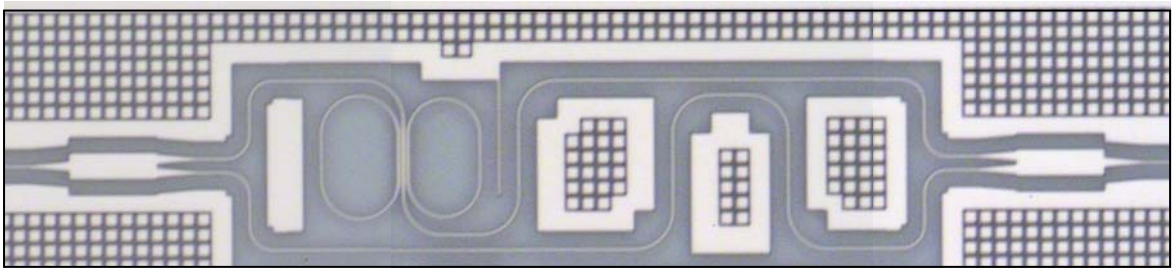

Fig. 5.8. Fabricated RBRMZI with γ=1.05 and g=150nm (Note that this figure is combined by three parts due to the limited visibility of the microscope).

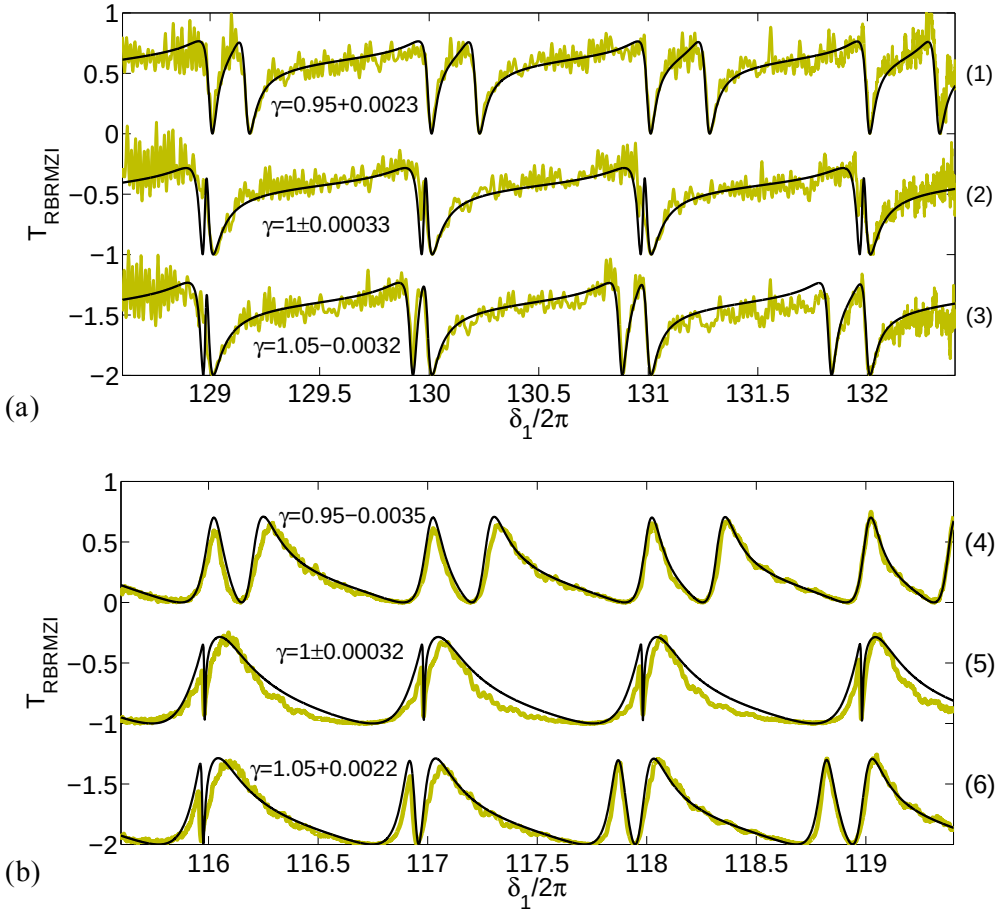

Fig. 5.9. Measured (thick-faded) and fitted (solid) transmissions of RBRMZI devices (T_{RBRMZI}). (a) g=150nm in bare silicon and (b) g=200nm with resist coating.

Fig. 5.9 shows the fitted transmissions of RBRMZI (T_{RBRMZI}) for six DUTs. DUT1 to 3 (DUT4 to 6) have a gap separation of 150nm (200nm) with bare silicon (resist coating). Please note that the resist coatings were initially processed for passivation purpose and then removed in some devices in order to compare the transparent resonances in DUTs under two different conditions, with resist coating and bare silicon. The procedure of curve fitting is explained in the following: (1) The round-trip loss a=0.995 is obtained for 1R2B fitting and the MMI transmission factor of 0.88 is obtained from MMI fittings. (2) The group index is adopted from RBR fitting as n_g~4.21/4.64 for resist coated/bare silicon devices. In order to

fit the whole spectrum, the variation of group index as functions of wavelength λ are taken into account as n_g=0.00564λ(μm)+4.2017 and n_g=0.017λ(μm)+4.6126, respectively. (3) The cavity size detuning γ that determines the locations of two individual resonances is obtained through adjusting the relative separation between the two resonances over the entire spectrum. (4) The coupling coefficient $r_{1,2}$ that determines the linewidth of the two resonances is deduced from 1R2B fitting. Here, we still assume r_1=r_2 for the asymmetric/symmetric RBR element since the radius difference (ΔR) between R1 and R2 is so small that the variation of r_1 and r_2 can be ignored, e.g. ΔR=91nm at γ=1.05. (5) The initial guess of the MZI imbalance phase (ϕ_B) that determines the asymmetricity of the Fano-lineshape is derived from fitting the spectra of RBRMZI with symmetric RBR component. It is much easier to get ϕ_B in the case of γ~1 since the resonance is characterized only by a single-cavity. Through repeating step (2) to (5) for fine-adjustments until the fitting converges, it is possible to find a combination of the imbalance phase and the coupling coefficient that fit well the experimental results. In this way, we obtain ϕ_B~0.31π and $r_{1,2}$~0.88 for DUT1 to 3, while ϕ_B~-0.7π and $r_{1,2}$~0.74 for DUT4 to 6. It is worth pointing out that the high imbalance phase ϕ_B~-0.7π makes the transparent resonance be inverted in DUT4 to 6, which is known as coupling-induced absorption [44]. Moreover, the coupling strength in the first three DUTs is weaker (larger $r_{1,2}$) than the coupling of the rest three DUTs even though the gap separation of the directional tri-coupler seems to indicate the contrary. This is explained by the mode-field size of the guided mode gets larger with more extended tail due to leaky evanescent field in the resist-coated devices.

Even though the best-fitted values of γ are shown in Fig. 5.9, it is interesting to highlight that there exists two possible fittings for symmetric RBR cases (DUT2 and DUT5) at γ~1 using slightly different group indices and cavity size detunings. This is because γ is too near unity to figure out which resonance comes from R1 or R2. There is also no discerning pattern deduced from the relative resonance separation which changes over different resonance orders. Thus, it is quite possible to fit the two special situations with ±Δγ considering that in symmetric limit, that is R1and R2 are interchangeable. Here, we take the resonance order of 130 in DUT2 for example, it can be fitted with two sets of (γ, n_g) as (1+0.00033, 4.6375) and (1-0.00033, 4.639). In fact, since the RBR structure is symmetric and γ is so near to one that it is likely to obtain reasonable fit with γ=1 while fixing all other fitting parameters, e.g. $r_{1,2}$, n_g and ϕ_B. We believe that this is owing to the value of γ should not deviate in the presence of coupling-induced phase shift (CIPS) due to the symmetry of RBR, i.e., the amount of CIPS in R1 and R2 are identical and the CIPS is almost cancelled-off with each other. This idea is strongly supported by the experimental findings indicated in Fig. 5.9. The calculated cavity size derivation Δγ/γ in DUT2 (DUT5) is only ~0.03% which is around 10 times smaller than that of Δγ/γ~0.3% in the asymmetric RBR shown by DUT1 and 3 (DUT4 and 6). Moreover, it is also evident that the measurement of devices in the bare silicon with high-contrast index exhibits more noise than the resist-coated devices. This is due to the fact that the bare silicon devices experience stronger reflection from the waveguide surface roughness and the input/output gratings, which contributes to the additional noise in the measurement results.

The advantage of the RBRMZI can be seen from DUT2 where the CRIT resonance has a bandwidth of 0.25nm, a free spectral rage of 12nm and Q~6300. For this device, the circumference difference of the two rings is around 2.2μm, which is much larger compared to the reported result of ~8nm in another CRIT system based on cascaded 1R2B resonators [45]. The finesse value of this transparency ~70 is obtained using relatively lower finesse rings ~23. For other cases like DUT 01, 03, 04 and 06, the ring resonances are detuned further away from each other, rendering in weaker inter-cavity interaction between the two outer rings. We further extract the Q-factors of CRIT resonance in more device measurements shown in Fig. 5.10. It is interesting to see that, for γ~1, the Q-factor is almost constant over the entire resonance positions, while it increases gradually with the increase of wavelength for γ~1.05 and γ~0.95 (see the solid line plots as an example). This trend is consistent with the fitting that it is hard to see the Veriner effect of the two ring resonances and thus partly explains why there are two existing fittings at γ is almost unity. Fig. 5.10 clearly tells us that the highest Q-factor is also achieved in this special situation γ~1. This result is in agreement with our earlier understanding that the CIPS is nearly cancelled in the symmetric RBR part. Thus, a very slight deviation of cavity size detuning will give rise to very sharp CRIT feature. Based on the collected results in Fig. 5.10, we estimate that Δγ/γ ~0.035% cavity size deviation with r_1~0.8 power coupling strength and ~0.5% cavity loss (or a=0.995) are sufficient to generate transparent resonance with Q-factors more than 18000.

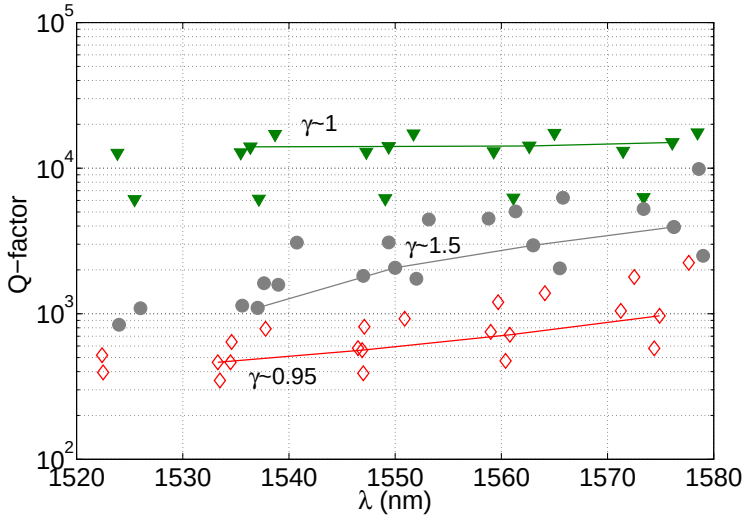

Fig. 5.10. Measured Q-factors of the RBRMZI devices for different cavity size detuning γ.

5.5 Summary

In this chapter, we experimentally realize the CRIT through RBR geometry synergistically integrated with MZI based on SOI technology. The transparency can be created without the requirement of different losses in the two rings and a very small difference of ring circumferences. The measurement result agrees well with the theoretical prediction, where the sharpest transparent resonance generates from slight cavity size detuning and low ring finesse at strong coupling condition.

Chapter 6 Conclusions and Future Work

6.1 Conclusions

In this thesis, I have theoretically analyzed and experimentally demonstrated the induced transparency in RBRMZI on SOI technology. Starting from the introduction of the waveguide mode theory, the effective index method used to solve the mode field of rectangular waveguides is discussed. The matrix formalism of two coupled waveguides is developed to analyze two basic one-ring configurations, 1R1B and 1R2B. The fundamental parameters and their relations are derived and discussed in details.

The main work began by investigating the RBR structure based on a tri-coupler. In this coupler, the self-coupling coefficients and overlap integrals should be neglected at weak coupling situations. At strong coupling conditions (e.g. r<0.99), the non-zero self-coupling coefficients and overlap integrals will introduce the asymmetry to the resonances. The 4π phase response of the RBR geometry can exhibit an EIT-like characteristic when the RBR is integrated with MZI. The destructive interferences between the three optical pathways in RBRMZI lead to the generation of CRIT in low-finesse resonators at strong coupling conditions. In addition, compared to another dual-ring MZI, the RBRMZI exhibits higher extinction ratio, finesse enhancement and lower background spectrum. The theoretical work extends to illustrate the CRIT using the mode analysis from TCMT. It shows an arbitrary narrow transparency can be flexibly obtained by modifying the resonance frequency and coupling strengths. The TCMT and the TMF are related via energy-conservation and Q-factors.

Finally, we demonstrate the CRIT in RBRMZI on SOI material platform. The transparency does not require different losses in the two rings ($a_1 \neq a_2$) and a very small difference of ring circumferences (e.g., in the range of nm). The measurement result agrees well with the theoretical prediction, where the sharpest transparent resonance generates from slight cavity size detuning and low ring finesse at strong coupling condition. Applying a slight cavity size detuning of $\gamma \sim 1.05$ and a coupling coefficient of $r_1 \sim 0.88$, the best transparency is obtained with a bandwidth of 0.25nm, a FSR of 12nm and a $Q \sim 6300$. Based on the further measurement results, it shows that the transparency with $Q \sim 18000$ can be created using a power coupling of $r_1 \sim 0.8$, a roundtrip loss of $a \sim 0.995$, a circumference of the one ring 43.4μm and a relative circumference deviation of the other ring $\Delta\gamma/\gamma \sim 0.035\%$. The transparency in RBR-MZI is applicable for low-power switching and tunable delay lines in signal processing based on chip-sized devices.

6.2 Future work

The future work should be focused on the improvement of current devices and the exploration of some possible applications using the RBRMZI.

In current devices, the fittings of the asymmetric transparent resonances are based on the assumption of the symmetric tri-couplers ($r_1=r_2$) in the RBR structures. However, it is not clear whether the fabricated gap separations in the tri-coupler region were open or identical (most likely not) as they were designed, as

well as the possible effects of different coupling coefficients ($r_1 \neq r_2$) have not been discussed. In addition, further investigations found that much better fittings were obtained using different coupling strengths. Therefore, it is necessary to show the scanning-electron micrographs of the RBR structures to see whether the tri-couplers have the uniform gap separations and waveguide widths. Another problem is the current transparency resonance is not pronounced. The sharpness of the transparency can be increased at strong coupling condition. However, the stronger coupling will aggravate the CIPS and the asymmetricity. There are several approaches that can be used to overcome this problem. Firstly, we can apply the symmetric tri-coupler in RBR to cancel the CIFS in the two rings. R1 and R2 should have the same radius in order to guarantee their identical ring-bus coupling strengths, which are different in current devices. Secondly, it is possible to eliminate the MZI imbalance caused by the loaded RBR through varying the wire width of the other bare MZI arm [36]. Thirdly, the variations of waveguide widths came from optical proximity, i.e., waveguide width in coupler region is narrower than that of isolated ones, can be compensated by optical proximity correction through adding certain geometries on the re-sized mask.

The active tuning (like switching) is a promising application for the narrow CRIT resonance. Fast switching speed and low-power consuming (or high extinction ratio) are the two important requirements in active optical devices. The CRIT used for switching with high extinction ratio has been proposed in reference [64], but the switching speed of this CRIT has not been investigated yet. In fact, a tradeoff exists where these two requirements. Let us take the resonance of 1R1B for example. In order to get low-power consuming modulation, a high-Q resonance is desirable. However, the higher Q leads to longer effective cavity lifetime and lower optical losses, suggesting that more time must be taken by the resonator to maintain the same modulation depth [7]. This tradeoff between the switching speed and the power consuming can be broken by the high-Q transparency in RBRMZI with low ring finesse (or low cavity lifetime). The advantage of CRIT in RBRMZI is that both requirements can be satisfied at strong coupling condition, in contrast to a push-pull relation of the two requirements in conventional CRIT schemes or single-cavity resonators. Therefore, an active device with fast switching speed and low-power consuming can be realized using the CRIT in RBRMZI.

Appendix A. Derivation of 3×3 Coupling Matrix

Fig. A1 shows the geometric outline of three parallel coupled waveguides with the power guidance in z direction. In order to make the notations consistent with that in RBR structure in main content, the three waveguides shall be orderly notated with 1, 0, 2.

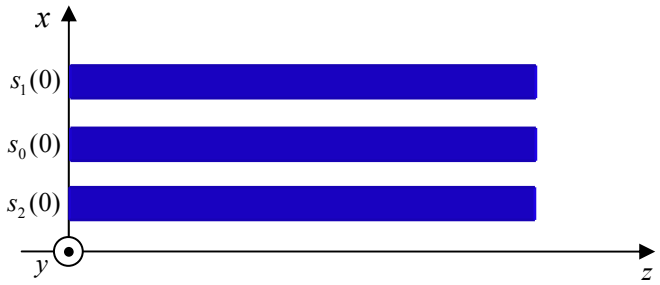

Fig. A1. Configuration of three parallel coupled waveguides oriented along z-axis, where $s_{1,0,2}(0)$ is the value of s at the position of z=0.

In order to simplify the calculation and analysis, we make the following assumptions for practical waveguide configurations: (1) The three waveguides should be identical with the same parameters, e.g. waveguide dimension and refractive index. (2) The waveguide-waveguide coupling is only noticeable for two adjacent elements. Conceptually, the coupling of light can occur between any two of the three waveguides. However, in the more realistic case, due to the fact that the coupling between two outer waveguides is only assisted by the presence of the center one, the direct coupling between them so weak that can be negligible (κ_{12}=0). (3) The overlap integrals are much smaller that can be negligible ($\hat{C}_{pq}$=0, q,p=1,2,3) compared with the self-coupling coefficients under both weak and strong coupling conditions, since the several orders of difference between the amplitudes of electric field and magnetic field [refer to Eq. (2.8)]. (4) The self-coupling coefficients should be taken into account at strong coupling conditions and be neglected at weak coupling conditions. Since at the weak coupling cases, the electric field overlap could be very small due to weak field perturbations between two neighboring waveguides. (5) In general, the self-coupling terms for the middle waveguide and two outer waveguides are not identical due to the different mode perturbations. Based on the above assumptions, the M-matrix in Eq. (2.7) can be rewritten as the following form for a general tri-coupler,

$$M = \begin{bmatrix} \beta + \kappa_{11} & \kappa_1 & 0 \\ \kappa_1 & \beta + \kappa_{00} & \kappa_2 \\ 0 & \kappa_2 & \beta + \kappa_{22} \end{bmatrix} \tag{A1}$$

where β is the propagation constant of a standalone waveguide without the presence of the other waveguides, $\kappa_{11,00,22}$ are the self-coupling coefficients and $\kappa_{1,2}$ are the cross-coupling coefficients between the side waveguide 1,2 with the center waveguide 0.

In Eq. (A1), we can see that the propagation constants in the diagonal elements are modified with the self-coupling coefficients, which will cause coupling-induced phase shift in the resonances. Generally,

where $\kappa_1 \neq \kappa_2$ and $\kappa_{11} \neq \kappa_{22} \neq \kappa_{00}$, one has the characteristic equation in the form of cubic equation, suggesting that it is too complicated to be solved analytically. However, we can assume $\kappa_{11}=\kappa_{22}$ since the fields integral of the cross-coupling counterparts are much larger compared to those in self-coupling coefficient. Refer to Eq. (2.8), mathematically, the self-coupling coefficient is calculated from a square of the fields with the perturbation of other waveguides. Since the "squared" field term can make the field tail shorter, which means that the fields overlap with $\Delta\varepsilon(x)$ becomes to quadratically smaller. In this regard, the field overlap of cross-coupling coefficients is much more sensitive to the variation of gap separations than that in the self-coupling coefficients. Therefore, when the gap separations are not so different (e.g. <50nm), it is still reasonable to assume that $\kappa_{11}=\kappa_{22}\neq\kappa_{00}$ in the case of $\kappa_1 \neq \kappa_2$.

Based on the above discussions, we follow closely the procedure from Eq. (2.9) to Eq. (2.11). Solving the equation $|M-I\sigma|=0$ for Eq. (A1), the three eigenvalues (σ) and corresponding eigenvectors (υ) can be expressed as the following equations,

$$\begin{aligned} &\sigma_{1,3} = \bar{\beta} \pm \psi,\ \upsilon_{1,3} = \begin{bmatrix} 1 & (-\Delta\beta \pm \psi)/\kappa_1 & \kappa_2/\kappa_1 \end{bmatrix}^{\mathrm{T}}, \\ &\sigma_2 = \beta + \kappa_{11},\ \upsilon_2 = \begin{bmatrix} 1 & 0 & -\kappa_1/\kappa_2 \end{bmatrix}^{\mathrm{T}}. \end{aligned} \tag{A2}$$

where $\bar{\beta}=\beta+(\kappa_{11}+\kappa_{00})/2$, $\psi=(\Delta\beta^2+\kappa^2)^{1/2}$, $\Delta\beta=(\kappa_{11}-\kappa_{00})/2$ and $\kappa^2=\kappa_1{}^2+\kappa_2{}^2$ is the effective coupling constant for the tri-coupler. Then substituting the three eigenvectors to $s=\Sigma_m c_m v_m \exp(i\sigma_m z)$, where c_m is the coefficients to be determined later. The output s can be expressed as,

$$\begin{bmatrix} s_1 \\ s_0 \\ s_2 \end{bmatrix} = \begin{bmatrix} \exp(i\sigma_1 z) & \exp(i\sigma_2 z) & \exp(i\sigma_3 z) \\ \dfrac{-\Delta\beta+\psi}{\kappa_1}\exp(i\sigma_1 z) & 0 & \dfrac{-\Delta\beta-\psi}{\kappa_1}\exp(i\sigma_3 z) \\ (\kappa_2/\kappa_1)\exp(i\sigma_1 z) & -(\kappa_1/\kappa_2)\exp(i\sigma_2 z) & (\kappa_2/\kappa_1)\exp(i\sigma_3 z) \end{bmatrix} \begin{bmatrix} c_1 \\ c_0 \\ c_2 \end{bmatrix} \tag{A3}$$

Substituting the eigenvalues in Eq. (A2) to Eq. (A3) and considering the initial conditions for power at $z=0$, we can find c_m in terms of $s_m(0)$ from Eq. (A3) as the following matrix,

$$\begin{bmatrix} c_1 \\ c_0 \\ c_2 \end{bmatrix} = \frac{\kappa_1}{2\kappa^2\delta} \begin{bmatrix} (\psi+\Delta\beta)\kappa_1 & \kappa^2 & (\psi+\Delta\beta)\kappa_2 \\ 2\kappa_2{}^2\psi/\kappa_1 & 0 & -2\kappa_2\psi \\ (\psi-\Delta\beta)\kappa_1 & -\kappa^2 & (\psi-\Delta\beta)\kappa_2 \end{bmatrix} \begin{bmatrix} s_1(0) \\ s_0(0) \\ s_2(0) \end{bmatrix} \tag{A4}$$

Then Eq. (A3) is substituted with Eq. (A4) to eliminate c_m, where the relations of $2\cos\delta=(e^{i\delta}+e^{-i\delta})$, $2i\sin\delta=(e^{i\delta}-e^{-i\delta})$ and $\psi^2-\Delta\beta^2=\kappa^2$ are used. Finally, we obtain a general 3×3 coupling matrix to connect the incident light and output response,

$$\begin{bmatrix} s_1 \\ s_0 \\ s_2 \end{bmatrix} = \exp(i\bar{\beta}z) \begin{bmatrix} r_1\exp(i\varphi_1) & it_1 & t_{12}\exp(i\varphi_{12}) \\ it_1 & r_0\exp(i\varphi_0) & it_2 \\ t_{21}\exp(i\varphi_{21}) & it_2 & r_2\exp(i\varphi_2) \end{bmatrix} \begin{bmatrix} s_1(0) \\ s_0(0) \\ s_2(0) \end{bmatrix} \tag{A5}$$

where r_q and t_q are real values, and φ are the additional transmission phases at strong coupling condition. The matrix elements in Eq. (A5) are expressed as the following set of equations,

$$
\begin{aligned}
&t_1 = \frac{\kappa_1}{\psi}\sin(\psi z),\ t_2 = \frac{\kappa_2}{\psi}\sin(\psi z),\ r_0\exp(i\varphi_0) = \cos(\psi z) - i\frac{\Delta\beta}{\psi}\sin(\psi z),\\
&r_1\exp(i\varphi_1) = \frac{\kappa_1^{\,2}}{\kappa^2}\left[\cos(\psi z) + i\frac{\Delta\beta}{\psi}\sin(\psi z)\right] + \frac{\kappa_2^{\,2}}{\kappa^2}\exp(i\Delta\beta z),\\
&r_2\exp(i\varphi_2) = \frac{\kappa_2^{\,2}}{\kappa^2}\left[\cos(\psi z) + i\frac{\Delta\beta}{\psi}\sin(\psi z)\right] + \frac{\kappa_1^{\,2}}{\kappa^2}\exp(i\Delta\beta z),\\
&t_{12}\exp(i\varphi_{12}) = t_{21}\exp(i\varphi_{21}) = \frac{\kappa_1\kappa_2}{\kappa^2}\left[\cos(\psi z) + i\frac{\Delta\beta}{\psi}\sin(\psi z) - \exp(i\Delta\beta z)\right].
\end{aligned}
\tag{A6}
$$

We can observe that all the phases are caused by $\Delta\beta$ from the self-coupling terms when a strong coupling occurs. In the case that the two outer waveguides are symmetrically located from the center one, the cross-coupling coefficients have $\kappa_1=\kappa_2$. Then Eq. (A6) can be simplified to,

$$
\begin{aligned}
&t_1 = t_2 = \frac{\kappa_1}{\psi}\sin(\psi z),\ r_0\exp(i\varphi_0) = \cos(\psi z) - i\frac{\Delta\beta}{\psi}\sin(\psi z),\\
&r_1\exp(i\varphi_1) = r_2\exp(i\varphi_2) = \frac{1}{2}\left[\cos(\psi z) + i\frac{\Delta\beta}{\psi}\sin(\psi z) + \exp(i\Delta\beta z)\right],\\
&t_{12}\exp(i\varphi_{12}) = t_{21}\exp(i\varphi_{21}) = \frac{1}{2}\left[\cos(\psi z) + i\frac{\Delta\beta}{\psi}\sin(\psi z) - \exp(i\Delta\beta z)\right].
\end{aligned}
\tag{A7}
$$

If we consider the asymmetric coupling case ($\kappa_1\neq\kappa_2$) in weak coupling situations, then all the self-coupling coefficients $\kappa_{11,00,22}$ can be neglected and thus the three waveguides have the same propagation constant β. In mathematical form, the common phase term $\exp(i\bar{\beta}z)$ becomes to $\exp(i\beta z)$, $\kappa_{11}=\kappa_{22}=\kappa_{00}=0$, $\Delta\beta=0$ and $\psi=\kappa$, then all the additional transmission phases disappear. Therefore, the following equations can be deduced from Eq. (A7),

$$
\begin{aligned}
&r_0 = \cos(\kappa z),\ r_1 = \frac{\kappa_1^2\cos(\kappa z) + \kappa_2^2}{\kappa^2},\ r_2 = \frac{\kappa_2^2\cos(\kappa z) + \kappa_1^2}{\kappa^2},\\
&t_1 = \frac{\kappa_1\sin(\kappa z)}{\kappa},\ t_2 = \frac{\kappa_2\sin(\kappa z)}{\kappa},\ t_{12} = t_{21} = \frac{\kappa_1\kappa_2}{\kappa^2}\left[\cos(\kappa z) - 1\right].
\end{aligned}
\tag{A8}
$$

Further the assumption under weak coupling conditions, when the coupling is symmetrical ($\kappa_1=\kappa_2$), the coupling constants in Eq. (A8) can be simplified to the following set of equations [Note that these equations can also be obtained from Eq. (A7), when all the self-coupling terms are neglected.],

$$
r_0 = \cos(\kappa z),\ t_1 = t_2 = \frac{\sin(\kappa z)}{\sqrt{2}},\ r_1 = r_2 = \frac{\cos(\kappa z) + 1}{2},\ t_{12} = t_{21} = \frac{\cos(\kappa z) - 1}{2}. \tag{A9}
$$

Note that the relationships among the coupling coefficients in Eq. (A8) can be obtained upon substituting coupling constants, which will be helpful for deducing the through transmission and buildup factors in Chapter 2. For example,

$$
r_2 + r_1 = \frac{\kappa_1^2\cos(\kappa z) + \kappa_2^2}{\kappa^2} + \frac{\kappa_2^2\cos(\kappa z) + \kappa_1^2}{\kappa^2} = \frac{(\kappa_2^2 + \kappa_1^2)\cos(\kappa z) + (\kappa_1^2 + \kappa_2^2)}{\kappa^2} = r_0 + 1 \tag{A10}
$$

where Eq. (A10) is substituted with $\kappa^2=\kappa_1^2+\kappa_2^2$ and $r_0=\cos(\kappa z)$ to cancel the numerator. Following the same method for other coupling coefficients in Eq. (A8), it shows that the following other relationships can be derived,

$$t_1 r_2 - t_2 t_{21} = t_1,\ t_2 r_1 - t_1 t_{12} = t_2,\ r_1 r_2 - t_{12} t_{21} = r_0,$$
$$r_1 r_0 + t_1^2 = r_2,\ r_0 r_2 + t_2^2 = r_1,\ r_0^2 + t_1^2 + t_2^2 = 1. \tag{A11}$$

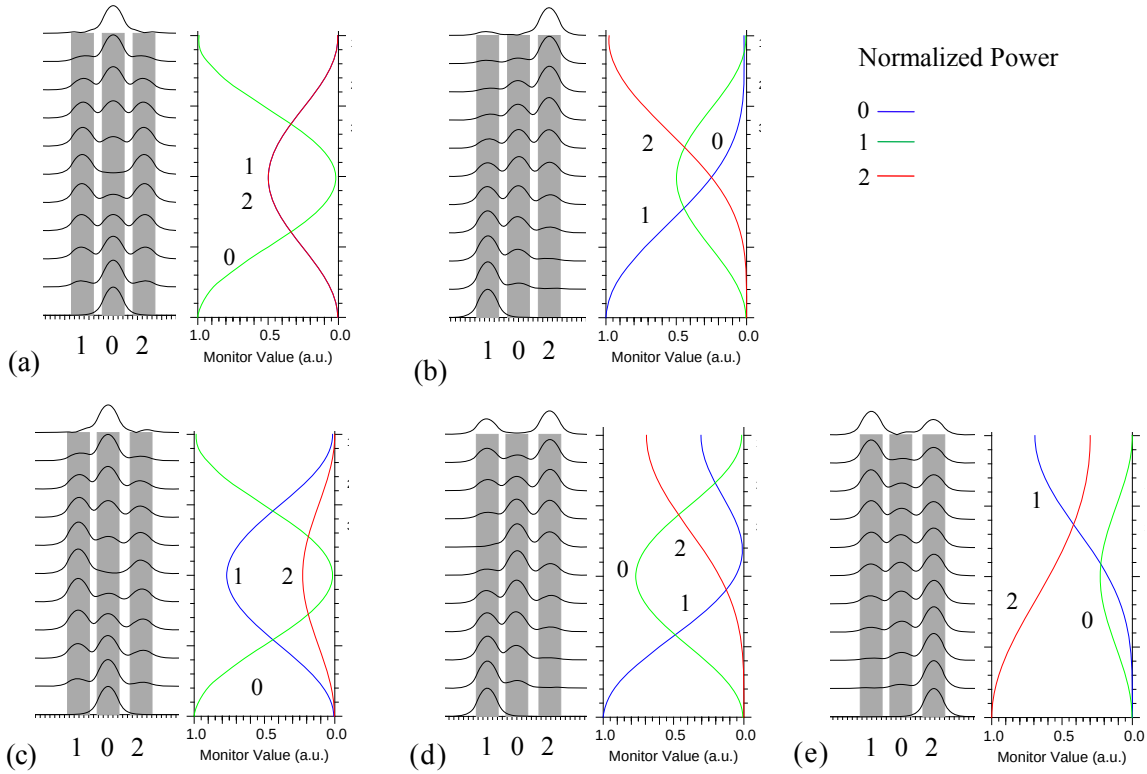

Fig. A2. BPM simulation results of three coupled waveguides. In each panel, the left part is the schematic representation of the evanescent coupling of modes and the right part is the monitor power normalized to the input power. The couplings are symmetric at (a)-(b) and asymmetric at (c)-(e).

The coupling constants in Eq. (A8) and Eq. (A9) can be verified with beam propagation method (BPM) numerical simulations. As shown in Fig. A2, when the two outer waveguides are located with the same separation from the center one (the symmetric case), the input light from the center waveguide splits equally to both outer elements. See panel (a), at the position where the center waveguide has a minimum value of zero, both the two outer waveguides have a maximum normalized power of 0.5, which is in agreement with the maximum square value of the cross-coupling constant $t_1 = \sin(\kappa z)/\sqrt{2}$ for two adjacent waveguides in Eq. (A9). This also explains why the maximum normalized power that can be achieved for the center guide is 0.5, when the light is lunched from one side waveguide [see panel (b)]. However, the situation becomes different when the two outer waveguides are located with different spaces from the center one (asymmetric case), the power still can be completely transferred to the other two waveguides if the light is launched from the center waveguide [see panel (c)]. The difference from the symmetric case

[see panel (a)] lies in the fact that the amount of the light split to two outer waveguides depends largely on the cross-coupling coefficients (t_1 and t_2) in Eq. (A8) of two neighboring waveguides. When the input power is started from the side waveguide, it cannot be completely guided to the opposite waveguide due to the maximum absolute value of the transmission coefficient between two outer waveguides t_{12} is no longer unity [see panel (d) and (e)]. Therefore, the simulation results agree with the theoretical predictions using Eq. (A8) and Eq. (A9), and suggest they can be used for analyzing the proposed RBR configuration. Note that, similar to the two coupled waveguides case, the common phase propagation term $\exp(i\bar{\beta}z)$ in Eq. (A5) is not considered in analytical formulations since it only shifts the resonance positions without changing the spectrum characteristics.

Appendix B. CRIT in Other Two-Ring Systems

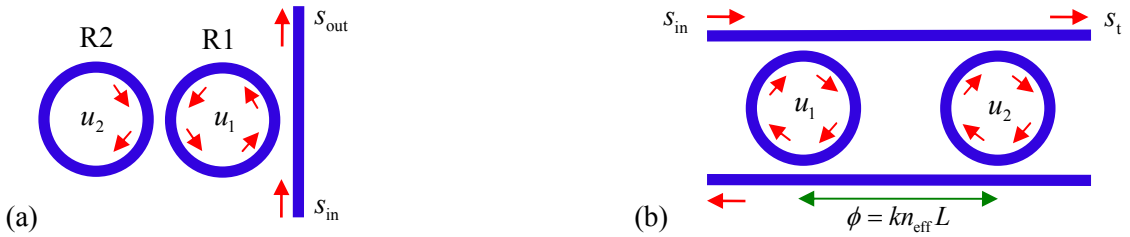

Fig. B1. Schematics of (a) two mutually coupled rings and, (b) two cascaded 1R2B resonator.

The CRIT can be obtained from two existing configurations shown in Fig. B1, two mutually coupled resonators system and two cascaded 1R2B system. For the mutual coupled resonators in Fig. B1(a), the equations for the evolution of resonator modes in time are given by,

$$\begin{aligned} du_1/dt &= (i\omega_1 - 1/\tau_{i1} - 1/\tau_e)u_1 + i\eta_c u_2 + i\eta_e s_{in} \\ du_2/dt &= (i\omega_2 - 1/\tau_{i2})u_2 + i\eta_c u_1 \\ s_{out} &= s_{in} + i\eta_e u_1 \end{aligned} \tag{B1}$$

where η_c represents the mutual coupling coefficient between modes u_1 and u_2. η_e is the coupling between R1 and the bus that can be expressed with $1/\tau_e=\eta_e^2/2$. The coupling coefficients in Eq. (B1) are related to that of the transfer matrix formalism in spatial domain. It can be seen from R1 that the traveling wave u_2 in R2 of amplitude $U_2(t)$ plays a similar role to the incident wave s_{in}. Thus one can consider the mutual coupling term to have a form of $i\eta_c' U_2(t)$, where η_c' serves as the coupling between a power normalized wave $U_2(t)$ and an energy normalized mode $u_1(t)$. Similar to the 1R1B case in Eq. (4.3), we can obtain $\eta_c'=t_c(v_{g1}/L_1)^{1/2}$, where t_c is the mutual coupling coefficient of R1 and R2 in space formulation. Converting to energy normalization for R2 by $i\eta_c' U_2=i\eta_c u_2(t)$ and $|U_2(t)|^2=v_{g2}/L_2|u_2(t)|^2$, we then obtain $\eta_c=\eta_c'(v_{g2}/L_2)^{1/2}$ and get the expression of η_c with foregoing relations as $\eta_c=t_c(v_{g1}/L_1)^{1/2}(v_{g2}/L_2)^{1/2}$ [60].

The normalized transmission is obtained by solving Eq. (B1) as,

$$\frac{s_{out}}{s_{in}} = \frac{(i\Delta\omega_1 + 1/\tau_{i1} - \eta_e^2/2)(i\Delta\omega_2 + 1/\tau_{i2}) + \eta_c^2}{(i\Delta\omega_1 + 1/\tau_{i1} + \eta_e^2/2)(i\Delta\omega_2 + 1/\tau_{i2}) + \eta_c^2} \tag{B2}$$

where $\Delta\omega_{1,2}=\omega-\omega_{1,2}$. For simplicity, we assume that the resonances of the both rings coincide $\Delta\omega_{1,2}=\Delta\omega$ and the intrinsic loss in the two rings are identical $1/\tau_{i1,i2}=1/\tau_i$. Eq. (B2) can be rewritten as,

$$\frac{s_{out}}{s_{in}} = \frac{\left[i(\Delta\omega - \left|\eta_c^2 - \eta_e^2/16\right|^{1/2}) + 1/\tau_i - \eta_e^2/4\right]\left[i(\Delta\omega + \left|\eta_c^2 - \eta_e^2/16\right|^{1/2}) + 1/\tau_i - \eta_e^2/4\right]}{\left[i(\Delta\omega - \left|\eta_c^2 - \eta_e^2/16\right|^{1/2}) + 1/\tau_i + \eta_e^2/4\right]\left[i(\Delta\omega + \left|\eta_c^2 - \eta_e^2/16\right|^{1/2}) + 1/\tau_i + \eta_e^2/4\right]} \tag{B3}$$

Eq. (B3) clearly tells us that the coincident resonance splits to two individual resonances with the positions of $\omega\pm|\eta_c^2-\eta_e^2/16|^{1/2}$. When there is no coupled bus where the resonance splitting is solely due to mutual coupling between the two rings, the detuned resonances can be expressed simply by $\omega\pm\eta_c$.

Furthermore, when the intrinsic loss in R2 is negligible ($1/\tau_{i2}\sim0$) and $\Delta\omega_1=\Delta\omega_2$, the power response in Eq. (B3) can be rewritten as the EIT-like expression in the following form,

$$T \equiv \left|\frac{s_{\text{out}}}{s_{\text{in}}}\right|^2 = 1 - \frac{8(2\eta_1^{-2}+\tau_{\text{i}})^{-1}(2/\tau_{\text{i}}+\eta_1^{\,2})(\Delta\omega)^2}{(\Delta\omega)^2(2/\tau_{\text{i}}+\eta_1^{\,2})^2 + 4\left[(\Delta\omega)^2-(2\eta_{\text{c}})^2/4\right]^2} \tag{B4}$$

From Eq. (B4) and the assumption of $1/\tau_{i2}\sim0$, we can conclude that the transparent spectrum can only be obtained when the two rings have different intrinsic losses, i.e. the loss in R2 is very low ($1/\tau_{i2}\sim0$) and much smaller than that of R1 ($1/\tau_{i2} \ll 1/\tau_{i1}$), where an under-coupling is required.

For the two cascaded 1R2B system shown in Fig. B1(b), we assume the coupling strengths at all directional couplers are identical, then the coupled-mode equations connecting the incident light, resonant modes and the through transmission are given by,

$$\begin{aligned} du_1/dt &= (i\omega_1 - 1/\tau_{\text{i1}} - 2/\tau_{\text{e}})u_1 + i\eta_{\text{e}}s_{\text{in}} + i\eta_{\text{e}}u_2 e^{i\phi} \\ du_2/dt &= (i\omega_2 - 1/\tau_{\text{i2}} - 2/\tau_{\text{e}})u_2 + i\eta_{\text{e}}(s_{\text{in}} + i\eta_{\text{e}}u_1)e^{i\phi} \\ s_{\text{t}} &= (s_{\text{in}} + i\eta_{\text{e}}u_1)e^{i\phi} + i\eta_{\text{e}}u_2 \end{aligned} \tag{B5}$$

where $\phi=kn_{\text{eff}}L$ stands for the coupling phase between the two resonant modes and L is the ring-to-ring separation. The through transmission is obtained by solving Eq. (B5) as,

$$\begin{aligned} \frac{s_{\text{t}}}{s_{\text{in}}} &= \frac{e^{i\phi}(i\Delta\omega_1 + 1/\tau_{\text{i1}})(i\Delta\omega_2 + 1/\tau_{\text{i2}})}{(i\Delta\omega_1 + 1/\tau_{\text{i1}} + \eta_{\text{e}}^{\,2}/2)(i\Delta\omega_2 + 1/\tau_{\text{i2}} + \eta_{\text{e}}^{\,2}/2) - e^{i2\phi}\eta_{\text{e}}^{\,4}/4} \xrightarrow{1/\tau_{\text{i1,i2}}=1/\tau_{\text{i}},\Delta\omega_{1,2}=\Delta\omega} \\ &= e^{-i\phi} + \frac{(\eta_{\text{e}}^{\,4}/4)(1-e^{-i\phi})^2}{i\Delta\omega + 1/\tau_{\text{i}} + (\eta_{\text{e}}^{\,2}/2)(1-e^{-i\phi})} - \frac{(\eta_{\text{e}}^{\,4}/4)(1+e^{-i\phi})^2}{i\Delta\omega + 1/\tau_{\text{i}} + (\eta_{\text{e}}^{\,2}/2)(1+e^{-i\phi})} \end{aligned} \tag{B6}$$

Expressing $e^{-i\delta}=\cos\delta-i\sin\delta$, we obtain the resonance positions as $\omega\pm(\eta_{\text{e}}^{\,2}/2)\sin\phi$ when $\Delta\omega_{1,2}=\Delta\omega$. Thus, the occurrence of resonance splitting relies on the transmission phase ϕ caused by ring-to-ring separation. When the phase ϕ is an integral multiple of π ($\phi=m\pi$), there is no resonance splitting, and the transmission can be simplified to that of 1R2B, while the resonance splitting always exists in other situations. When the two resonances don't coincide $\Delta\omega_1\neq\Delta\omega_2$, the ring-to-ring separation satisfies $\exp(i2\phi)=1$ and the intrinsic losses are negligible $1/\tau_{i1,i2}\sim0$, the power in Eq. (B6) can be rewritten as the EIT-like expression,

$$T \equiv \left|\frac{s_{\text{t}}}{s_{\text{in}}}\right|^2 = 1 - \frac{2\eta_{\text{e}}^{\,2}(2\eta_{\text{e}}^{\,2})(\Delta\bar{\omega})^2}{(2\eta_{\text{e}}^{\,2})^2(\Delta\bar{\omega})^2 + 4\left[(\Delta\bar{\omega})^2-(\omega_2-\omega_1)^2/4\right]^2} \tag{B7}$$

where $\Delta\bar{\omega}=\omega-(\omega_1+\omega_2)/2$. A comparison between Eq. (B4) and Eq. (B7) reveals two main differences between the two systems. The first difference is the bandwidth of the transparency is determined by the mutual coupling η_{c} in the mutual coupled resonators, while it is determined by the detuning of resonance frequencies (or the separation of two resonances) in the two cascaded 1R2B system $|\omega_2-\omega_1|$. The second difference is the CRIT only happens when the two resonant frequencies are coincident with each other in the former system, whereas the later system requires the two rings to resonate in different frequencies.

Author's Publications

1. **Y. B. Zhang**, D. H. Zhang, and T. Mei "*Temporal coupled mode theory in ring-bus-ring Mach-Zehnder interferometer*," Applied Opt., vol. 51 (2012).
2. **Y. Zhang**, S. Darmawan, L.Y. M. Tobing, T. Mei, and D. H. Zhang, "*Coupled resonator induced transparency in ring-bus-ring Mach-Zehnder interferometer*," J. Opt. Soc. Am. B, vol. 28 (2011).
3. **Y. Zhang**, S. Darmawan, L.Y. M. Tobing, T. Mei, and D. H. Zhang, "*Electromagnetically induced transparency-like resonance in ring-bus-ring Mach-Zehnder interferometer*," Photonics Global Conference, Singapore, 2010 (oral presentation and Best Paper Award).
4. **Y. B. Zhang**, S. Darmawan, T. Mei, and D. H. Zhang, "*Temporal coupled mode theory in ring-bus-ring configuration*," Topical Meeting on Advances in Optoelectronics and Micro/nano-optics, Guangzhou, China, 2010 (oral presentation).
5. S. Darmawan, Landobasa Y. M. Tobing, L. Tjahjana, **Y. Zhang**, and D. H. Zhang, "*Realization of coupled-resonator-induced transparency in silicon-on-insulator based on ring-bus-ring geometry*," International Quantum Electronics Conference/Conference on Lasers and Electro-Optics Pacific Rim, Sydney, Australia, 2011(poster).

References

[1] M. S. Dahlem, C. W. Holzwarth, A. Khilo, F. X. Kärtner, H. I. Smith, and E. P. Ippen, "Reconfigurable multi-channel second-order silicon microring-resonator filterbanks for on-chip WDM systems," Opt. Express **19**, 306-316 (2011).

[2] Kuldeep Amarnath, *Active microring and microdisk optical resonators on Indium Phosphide*, PH.D. Thesis, University of Maryland, College Park (2006).

[3] John Heebner, Rohit Grover, and Tarek Ibrahim, *Optical microresonators*: *theory*, *fabrication*, *and applications*, (Springer Series in Optical Sciences 138, Springer, New York, 2008).

[4] K. DeVos, I. Bartolozzi, E. Schacht, P. Bienstman, and R. Baets, "Silicon-on-insulator microring resonator for sensitive and label-free biosensing," Opt. Express **15**, 7610-7615 (2007).

[5] J. S. Levy, A. Gondarenko, M. A. Foster, A. C. Turner-Foster, A. L. Gaeta, and M. Lipson, "CMOS-compatible multiple-wavelength oscillator for on-chip optical interconnects," Nature Photon. **4**, 37-39 (2010).

[6] G. S. Wiederhecker, L. Chen, A. Gondarenko, and M. Lipson, "Controlling photonic structures using optical forces," Nature **462**, 633-636 (2009).

[7] K. Preston, P. Dong, B. Schmidt, and M. Lipson, "High-speed all-optical modulation using polycrystalline silicon microring resonators," Appl. Phys. Lett. **92**, 151104 (2008).

[8] Q. Xu, B. Schmidt, S. Pradhan, and M. Lipson, "Micrometer-scale silicon electro-optic modulator," Nature **435**, 325-327 (2005).

[9] Y. M. Landobasa, S. Darmawan, and M. K. Chin, "Asymmetric Fano resonance and bistability for high extinction ratio, large modulation depth, and low power switching," Opt. Express **14**, 12770-12781 (2006).

[10] S. Darmawan, Y. M. Landobasa, P. Dumon, R. Baets, and M. K. Chin, "Resonance enhancement in silicon-on-insulator-based two-ring Mach-Zehnder interferometer," IEEE Photon. Technol. Lett. **20**, 1560-1562 (2008).

[11] I. Chremmos and N. Uzunoglu, "Reflective properties of double-ring resonator system coupled to a waveguide," IEEE Photon. Technol. Lett. **17**, 2110-2112 (2005).

[12] P. Chamorro-Posada and F. J. Fraile-Pelaez, "Fast and slow light in zigzag microring resonator chains," Opt. Lett. **34**, 626-628 (2009).

[13] J. E. Heeber, R. W. Boyd, and Q. H. Park, "SCISSOR solitons and other novel propagation effects in microresonator-modified waveguides," J. Opt. Soc. Am. B **19**, 722–731 (2002).

[14] F. Xia, L. Sekaric, and Y. Vlasov, "Ultracompact optical buffers on a silicon chip," Nature Photon. **1**, 65-71 (2007).

[15] L. Y. M. Tobing, P. Dumon, R. Baets, and M. K. Chin, "Boxlike filter response based on complementary photonic bandgap in two-dimensional microresonator arrays," Opt. Lett. **33**, 2512 (2008).

[16] L. Zhang, M. Song, T. Wu, L. Zou, R. G. Beausoleil, and A. E. Willner, "Embedded ring resonators for microphotonic applications," Opt. Lett. **33**, 1978-1980 (2008).

[17] V. Van, T. N. Ding, W. N. Herman, and P. T. Ho, "Group delay enhancement in circular arrays of microring resonators," IEEE Photon. Technol. Lett. **20**, 997-999 (2008).

[18] J. Yang, F. Wang, X. Jiang, H. Qu, M. Wang, and Y. Wang, "Influence of loss on linearity of microring-assisted Mach-Zehnder modulator," Opt. Express **12**, 4178-4188 (2004).

[19] S. Fan, "Sharp asymmetric line shapes in side-coupled waveguide-cavity systems," Appl. Phys. Lett. **80**, 908-910 (2002).

[20] M. Terrel, M. J. F. Digonnet, and S. Fan, "Ring-coupled Mach-Zehnder interferometer optimized for sensing," Appl. Opt. **48**, 4874-4879 (2009).

[21] J. E. Heebner and R. W. Boyd, "Enhanced all-optical switching by use of a nonlinear fiber ring resonator," Opt. Lett. **24**, 847-849 (1999).

[22] W. Green, R. Lee, G. DeRose, A. Scherer, and A. Yariv, "Hybrid InGaAsP-InP Mach-Zehnder racetrack resonator for thermooptic switching and coupling control," Opt. Express **13**, 1651-1659 (2005).

[23] S. Darmawan, Y. M. Landobasa, P. Dumon, R. Baets, and M. K. Chin, "Nested-ring Mach-Zehnder interferometer on silicon-on-insulator," IEEE Photon. Technol. Lett. **20**, 9-11 (2008).

[24] G. T. Paloczi, Y. Huang, A. Yariv, and S. Mookherjea, "Polymeric Mach-Zehnder interferometer using serially coupled microring resonators," Opt. Express **11**, 2666-2671 (2003).

[25] S. Darmawan, Y. M. Landobasa, and M. K. Chin, "Phase engineering for ring enhanced Mach-Zehnder interferometers," Opt. Express **13**, 4580-4588 (2005).

[26] Y. Lu, L. Xu, M. Shu, P. Wang, and J. Yao, "Proposal to produce coupled resonator-induced transparency and bistability using microresonator enhanced Mach-Zehnder interferometer," IEEE Photon. Technol. Lett. **20**, 529-531 (2008).

[27] S. Y. Cho and R. Soref, "Interferometric microring-resonant 2×2 optical switches," Opt. Express **16**, 13304-13314 (2008).

[28] J. K. S. Poon, L. Zhu, G. A. DeRose, and A. Yariv, "Transmission and group delay of microring coupled-resonator optical waveguides," Opt. lett. **31**, 456-458 (2006).

[29] J. E. Heebner and R. W. Boyd, "Slow light and fast light in resonator-coupled waveguides," J. Mod. Opt. **49**, 2629-2636 (2002).

[30] Z. Zhang, M. Dainese, L. Wosinski, and M. Qiu, "Resonance-splitting and enhanced notch depth in SOI ring resonators with mutual mode coupling," Opt. Express **16**, 4621-4630 (2008).

[31] Y. Dumeige, "Stopping and manipulating light using a short array of active microresonators," Europhys. Lett. **86,** 14003 (2009).

[32] P. Dumon, W. Bogaerts, V. Wiaux, J. Wouters, S. Beckx, J. V. Campenhout, D. Taillaert, B. Luyssaert, P. Bienstman, D. V. Thourhout, and R. Baets, "Low-loss SOI photonic wires and ring resonators fabricated with deep UV lithography," IEEE Photon. Technol. Lett. **16**, 1328-1330 (2004).

[33] L.-W. Luo, G. S. Wiederhecker, J. Cardenas, C. Poitras, and M. Lipson, "High quality factor etchless silicon photonic ring resonators," Opt. Express **19**, 6284-6289 (2011).

[34] V. Van, T. A. Ibrahim, K. Ritter, P. P. Absil, F. G. Johnson, R. Grover, and P.-T. Ho, "All-optical nonlinear switching in GaAs-AlGaAs microring resonators," IEEE Photon. Technol. Lett. **14**, 74-76 (2002).

[35] M. A. Popović, C. Manolatou, and M. R. Watts, "Coupling-induced resonance frequency shifts in coupled dielectric multi-cavity filters," Opt. Express **14**, 1208-1222 (2006).

[36] S. Darmawan, Landobasa Y. M. Tobing, and T. Mei, "Coupling induced phase shift in a microring-coupled Mach-Zehnder interferometer," Opt. Lett. **35**, 238 (2010).

[37] Q. Li, M. Soltani, S. Yegnanarayanan, and A. Adibi, "Design and demonstration of compact, wide bandwidth coupled-resonator filters on a silicon-on-insulator platform," Opt. Express **17**, 2247-2254 (2009).

[38] A. M. Prabhu, V. Van, W. N. Herman, and P. T. Ho, "Compact silicon microring-assisted directional couplers for optical signal processing applications," Opt. Lett. **34**, 1249 (2009).

[39] V. Van and P. T. Ho, "Microring-assisted coupling between dissimilar waveguides," Tsinghua Sci. Technol. **15**, 145-150 (2010).

[40] D. D. Smith, H. Chang, K. A. Fuller, A. T. Rosenberger, and R. W. Boyd, "Coupled-resonator-induced transparency," Phys. Rev. A **69**, 063804 (2004).

[41] L. Maleki, A. B. Matsko, A. A. Savchenkov, and V. S. IIchenko, "Tunable delay line with interacting whispering-gallery-mode resonators," Opt. Lett. **29**, 626-628 (2004).

[42] M. F. Yanik, W. Suh, Z. Wang, and S. Fan, "Stopping light in a waveguide with an all-optical analog of electromagnetically induced transparency," Phys. Rev. Lett. **93**, 233903 (2004).

[43] M. D. Lukin and A. Imamoglu, "Controlling photons using electromagnetically induced transparency," Nature **413**, 273-276 (2001).

[44] A. Naweed, G. Farca, S. I. Shopova, and A. T. Rosenberger, "Induced transparency and absorption in coupled whispering-gallery microresonators," Phys. Rev. A **71**, 043804 (2005).

[45] Q. Xu, S. Sandhu, M. L. Povinelli, J. Shakya, S. Fan, and M. Lipson, "Experimental realization of an on-chip all-optical analogue to electromagnetically induced transparency," Phys. Rev. Lett. **96**, 123901 (2006).

[46] X. Yang, M. Yu, D.-L. Kwong, and C.W. Wong, "Coupled resonances in multiple silicon photonic crystal cavities in all-optical solid-state analogy to electromagnetically induced transparency," IEEE J. Sel. Top. Quantum Electron. **16**, 288-294 (2010).

[47] Y. Dumeige, T. K. N. Nguyên, L. Ghisa, S. Trebaol, and P. Féron, "Measurement of the dispersion induced by a slow-light system based on coupled active-resonator-induced transparency," Phys. Rev. A **78**, 013818 (2008).

[48] S. Kocaman, X. Yang, J. F. McMillan, M. B. Yu, D. L. Kwong, and C. W. Wong, "Observations of temporal group delays in slow-light multiple coupled photonic crystal cavities," Appl. Phys. Lett. **96**, 221111 (2010).

[49] Q. Xu, P. Dong, and M. Lipson, "Breaking the delay-bandwidth limit in a photonic structure," Nature Phys. **3**, 406-410 (2007).

[50] K. Totsuka, N. Kobayashi, and M. Tomita, "Slow light in coupled-resonator-induced transparency," Phys. Rev. Lett. **98**, 213904 (2007).

[51] Q. Xu, J. Shakya, and M. Lipson, "Direct measurement of tunable optical delays on chip analogue to electromagnetically induced transparency," Opt. Express **14**, 6463-6468 (2006).

[52] Shun Lien Chuang, *Physics of Photonic Devices*, 2nd Ed. (Wiley, New York, 2009).

[53] http://www.optiwave.com/products/fdtd_overview.html.

[54] S. L. Chuang, "Application of the strongly coupled-mode theory to integrated optical device," IEEE J. Quantum Electron. **23**, 499-509 (1987).

[55] H. Yi, D. S. Citrin, Y. Chen, and Z. Zhou, "Dual-microring-resonator interference sensor," Appl. Phys. Lett. **95**, 191112 (2009).

[56] F. Xia, L. Sekaric, and Y. Vlasov, "Mode conversion losses in silicon-on-insulator photonic wire based racetrack resonators," Opt. Express **14**, 3872-3886 (2006).

[57] D.-X. Xu, A. Densmore, P. Waldron, J. Lapointe, E. Post, A. Delâge, S. Janz, P. Cheben, J. H. Schmid, and B. Lamontagne, "High bandwidth SOI photonic wire ring resonators using MMI couplers," Opt. Express **15**, 3149-3155 (2007).

[58] D. X. Xu, P. Cheben, A. Delâge, S. Janz, B. Lamontagne, E. Post, and W. N. Ye, "Polarization-insensitive MMI-coupled ring resonators in silicon-on-insulator using cladding stress engineering," Photon. West SPIE Proc. **6477**, 64770D (2007).

[59] Hermann Anton Haus, *Waves and Fields in Optoelectronics*. (Englewood Cliffs, NJ: Prentice-Hall, 1984).

[60] B. E. Little, S. T. Chu, H. A. Haus, J. Foresi, and J. P. Laine, "Microring resonator channel dropping filters," IEEE J. Lightwave Technol. **15**, 998-1005 (1997).

[61] C. Manolatou and M. Lipson, "All-optical silicon modulators based on carrier injection by two-photon absorption," J. Lightwave Technol. **24**, 1433-1439 (2006).

[62] S. Fan, W. Suh, and J. D. Joannopoulos, "Temporal coupled-mode theory for the Fano resonance in optical resonators," J. Opt. Soc. Am. A **20**, 569-572 (2003).

[63] W. Suh, Z. Wang, and S. Fan, "Temporal coupled-mode theory and the presence of non-orthogonal modes in lossless multimode cavities," IEEE J. Quantum Electron. **40**, 1511-1518 (2004).

[64] Q. Xu, "Silicon dual-ring modulator," Opt. Express **17**, 20783-20793 (2009).

[65] Y. Li and M. Xiao, "Observation of quantum interference between dressed states in an electromagnetically induced transparency," Phys. Rev. A **51**, 4959-4962 (1995).

[66] Z. Han and S. I. Bozhevolnyi, "Plasmon-induced transparency with detuned ultracompact Fabry-Perot resonators in integrated plasmonic devices," Opt. Express **19**, 3251-3257 (2011).

[67] http://www.epixfab.eu/.

[68] F. V. Laere, T. Claes, J. Schrauwen, S. Scheerlinck, W. Bogaerts, D. Taillaert, L. O'Faolain, D.V. Thourhout, and R. Baets, "Compact focusing grating couplers for silicon-on-insulator integrated circuits," IEEE Photon. Technol. Lett. **19,** 1919-1921 (2007).